UNIVERSITY OF OKLAHOMA

GRADUATE COLLEGE

ENSEMBLE KALMAN FILTER DATA ASSIMILATION OF VORTEX-SE P3 TAIL DOPPLER RADAR AND COMPACT RAMAN LIDAR DATA FOR A 13 APRIL 2018 TORNADIC SUPERCELL

A THESIS

SUBMITTED TO THE GRADUATE FACULTY

in partial fulfillment of the requirements for the

Degree of

MASTER OF SCIENCE

By

JONATHAN TYLER DEGRAW
Norman, Oklahoma
2025

ENSEMBLE KALMAN FILTER DATA ASSIMILATION OF VORTEX-SE
P3 TAIL DOPPLER RADAR AND COMPACT RAMAN
LIDAR DATA FOR A 13 APRIL 2018 TORNADIC SUPERCELL

A THESIS APPROVED FOR THE
SCHOOL OF METEOROLOGY

BY THE COMMITTEE CONSISTING OF

Dr. Ming Xue, Chair

Dr. Xiao-Ming Hu

Dr. James Ruppert

Acknowledgements

The work required to complete this thesis would have been impossible without the influence of several individuals in my professional and personal life. I am grateful for the assistance of my advisor, Dr. Ming Xue, who met with me weekly and guided me throughout the research process. Dr. Xue was very patient with me, especially when several important life events pushed back my graduation timeline. I am grateful for the work of Dr. Ningzhu Du, who conducted initial data assimilation (DA) and forecast experiments on the 2500 m grid before I joined the project. I am grateful for the support of Dr. Xiao-Ming Hu, who helped me learn proper implementation of DA and forecasting code. I am grateful for the contributions made by Dr. Rong Kong, who helped develop new codes in the ARPS EnKF DA system. I am grateful to those who participated in the VORTEX-SE field campaign, for providing me with the unique data sets I used in my experiments. The NOAA Office of Marine and Aviation Operations (OMAO), the NOAA Aircraft Operations Center (AOC), and the National Severe Storms Laboratory (NSSL) are gratefully acknowledged for providing NOAA P3 flight hours, skillful operation of the NOAA P3 aircraft N42RF, and travel support respectively for the collection of P3 scientific data during VORTEX-SE (2018). I thank Dr. Conrad Ziegler, who provided access to his objectively analyzed NOAA P3 airborne dual tail Doppler radar and KULM ground-based radar radial velocity and reflectivity fields generated for the 13-14 April 2018 Monroe, LA storm. I am grateful for the assistance of Dr. Dan Stechman, who helped with the application of the radar editing script and radar analysis codes. Dr. Todd Murphy is thanked for providing access to the KULM radar data. I am also grateful for Drs. Guo Lin and Zhien Wang, who provided the retrieved compact Raman lidar moisture profile data.

Finally, I would like to thank my family. I thank my beautiful wife Jasey, for her love, support, and encouragement. I thank my parents, Tyler and Sarah, for their love and support. I also thank my son, Calvin, whose life motivates me daily to work diligently.

I was supported in my research by National Science Foundation (NSF) grant AGS-1917701. The experiments were conducted using NSF-funded supercomputing systems. DA experiments were conducted on the Expanse supercomputing system operated by the San Diego Supercomputer Center at UC San Diego. Forecasts were conducted on the Stampede3 supercomputing system operated by the Texas Advanced Computing Center at the University of Texas at Austin.

Table of Contents

List of Figures

List of Tables

Abstract

An integral part of any numerical weather prediction (NWP) system is data assimilation (DA): the process of optimally combining observations and model state backgrounds to minimize the overall error in the resulting analysis. Over the past two decades, data from several different observing systems have been assimilated for real convective scale cases. The assimilation of reflectivity (Z) and radial velocity (V_r) data collected by Weather Surveillance Radar-1988 Doppler (WSR-88D) radars has been well studied and their positive impact in NWP is well known. Unfortunately, due to their stationary nature, the distance between WSR-88D radars and storms of interest can result in low-resolution data or incomplete data coverage. Consequently, DA of specialized weather radar observations has also been studied, including observations collected by truck-based mobile radars. Results in these studies have shown that analyses produced using both WSR-88D DA and specialized radar DA are improved versus analyses generated from WSR-88D DA alone. The assimilation of thermodynamic profiles, retrieved from thermodynamic remote sensors, has also been conducted with the goal of improving analyzed storm environmental conditions, particularly in the boundary layer.

Building upon experiments conducted in existing literature, this study performs ensemble Kalman filter (EnKF) DA of observations obtained during the 2018 Verification of the Origins of Rotation in Tornadoes Experiment Southeast (VSE18) field campaign for a cyclic, multi-tornado producing supercell that occurred during the late evening of 13 April 2018 near Monroe, Louisiana. In addition to surface observations and WSR-88D Z and V_r data, other unique specialized VSE18 data are also assimilated. These data include dual tail Doppler radar (TDR) V_r data, downward facing compact Raman lidar (CRL) retrieved water vapor mixing ratio (q_v) profiles, V_r data collected by an S-band WSR-88D equivalent radar operated by University of

Louisiana Monroe (KULM), and special radiosondes launched from Minden and Monroe Lousiana. The DA was performed in a series of experiments on nested 2500 m and 500 m grids using the Weather Research and Forecasting (WRF) model and the Advanced Regional Prediction System (ARPS) EnKF DA system. Deterministic forecasts were then performed using ensemble mean analyses for each DA experiment, on two-way nested 2500 m, 500 m, and 100 m WRF model grids.

The impact of the data on the analyses was evaluated through a series of data denial experiments. CRL DA results in much larger values of q_v in the inflow region of the Monroe supercell than the other analyses. TDR and KULM DA results in higher values of low-level vertical vorticity, and thereby a stronger tornadic like vortex (TLV), in the analysis. The TLV is absent in other analyses. TDR and KULM DA also increases the strength of low-level and mid-level updrafts in the analysis. The impact of assimilating special soundings in earlier DA cycles on the analyses of later DA cycles is relatively small, and the sign of the impact on analyzed updraft intensity and low-level rotation is not always consistent. This limited impact is likely attributable to the advection of the sounding-modified environment away from the supercell. Ultimately, experiments assimilating both CRL, TDR, and KULM data produced superior analyses, since they feature strong TLVs, deep intense updrafts, and improved boundary layer conditions in the inflow region of the supercell.

The impact of the DA on storm forecasts was also examined. In CRL DA experiments, the forecasted Monroe supercell retains supercellular characteristics, including strong mid-level updrafts and associated mesocyclone, longer than the forecasts from other experiments. Generally, CRL DA experiments better forecast reflectivity than other experiments. CRL DA experiments have longer, more intense UH tracks than most other experiments. TDR and KULM

V_r DA experiments better predict the intensity, track, and overall structure of the TLV. In TDR and KULM V_r DA experiments, the predicted TLV intensifies significantly within the first 5 to 10 minutes of the forecast. Unfortunately, the TDR and KULM V_r DA seems to degrade reflectivity forecasts, as indicated by poor statistical skill scores, and the qualitatively observed disorganization of the forecasted supercell 15 to 20 minutes after forecast initialization. Special sounding DA does not consistently improve forecasts.

Additional work is required to determine why TDR and KULM DA degraded predicted reflectivity forecasts. If possible, CRL, TDR, and KULM DA should be conducted for additional VSE18 cases. Ensemble forecasts should also be conducted using ensemble analyses, as better predictions of the TLV may be obtained in the forecasts for individual ensemble members.

Chapter 1: Introduction

1.1 Background and Motivation

Numerical weather prediction (NWP) model simulations assist meteorologists in identifying and understanding key physical processes involved in tornado formation and intensification. The first paper to assert NWP of convective scale storms, at horizontal resolutions on the order of 1 km, was published by Lilly (1990). Since then, innovations made in high-performance computing, atmospheric model and observation systems, and data assimilation (DA) have allowed the accuracy of NWP to steadily improve (Simmons and Hollingsworth 2002; Stensrud et al. 2009; Stensrud et al. 2013). Since NWP is an initial value problem (Bjerknes 1904), an integral part of any NWP system is DA: the process of optimally combining observations and model background state, thus lowering the overall error in the resulting analysis (Lorenc 1986). Several DA algorithms have been developed to accomplish this goal, including the three-dimensional variational approach (3DVar), the four-dimensional variation approach (4DVar), ensemble Kalman filtering (EnKF), and various hybrid ensemble-variational techniques (Gustafsson et al. 2018). Since NWP forecasts play a vital role in the preservation of life and property, it is important that new DA capabilities continue to be developed and investigated.

The 3DVar finds optimal analyses by minimizing an associated cost function using iterative procedures (Lorenc 1986). The cost function can be minimized by setting the gradient of the cost function to zero. In comparison to other methods, 3DVar has a lower computational cost and is generally easier to implement. Complex observation operators, assuming they are linear or weakly non-linear, can easily be incorporated into 3DVar. Equation constraints can be applied to the cost function, increasing accuracy. However, defining sufficiently accurate background error covariances for all model variable pairs is difficult. Typically, the background error covariance used in 3DVar is derived from historical data and is therefore not flow-dependent. This DA method has been successfully implemented in plethora of both mesoscale and convective scale NWP experiments (Hu et al. 2006a; Hu et al. 2006b; Schenkman et al. 2011; Natenberg et al. 2013), and continues to be used for a variety of applications. Gao et al. (2002) developed a 3DVar system for the Center for Analysis and Prediction of Storms (CAPS) Advanced Regional Prediction System (ARPS) model DA system.

Like 3DVar, 4DVar generates analyses by iteratively minimizing a cost function. Additional and modified terms in the cost function allow for the assimilation of observations across a given time interval (Lewis and Derber 1985; Courtier 1997; Kalnay 2003). Unlike 3DVar, calculating the gradient of the observation term in the cost function requires the use of a tangent linear version of the forward prediction, i.e., the NWP model, and its adjoint. In this way, the 4DVar leverages the NWP model as a strong constraint within the DA framework, establishing physical connections among observed and unobserved model state variables. The main advantage of 4DVar is that if (1) the model is assumed perfect and (2) the initial background error covariance is assumed correct, the analyses generated at the conclusion of the DA period are equivalent to those of the extended Kalman filter (EKF; Kalnay 2003). Thus, unlike 3DVar, the background error covariance implicitly evolves within 4DVar from initial time to final time and is therefore considered flow-dependent. Unlike EKF, the final background error and analysis error covariances are not products of the 4DVar DA and consequently are not available after DA is complete (the calculation of error covariance in EKF is prohibitively expensive in EKF for realistic NWP models, however). Generally, 4DVar is computationally more expensive than 3DVar and is computationally slightly less expensive than EnKF (assuming ensemble size $\leq$ 100). The accuracy of 4DVar analyses is generally higher than those of 3DVar and is similar to those of EnKF. 4DVar is less popular for convective scale DA experiments, in part due to the difficulty of developing and maintaining a tangent linear model and its adjoint in the presence of complex nonlinear physics processes that are important at such scales (Qin 1996). Thus far, 4DVar has enjoyed limited success at the convective scale.

In EnKF DA algorithms, flow-dependent background error covariances are derived statistically from an ensemble of forecasts and are used to update state variables (Evensen 1994). The solution approximates that of the EKF. In EKF, the linear model matrix involved in updating error covariances has a size equal to the degrees of freedom of the NWP model, which can be very large. This makes solving EKF very computationally expensive. In EnKF, the background error covariance is estimated using an ensemble of forecasts, usually using an ensemble size between 10 and 100 (Kalnay 2003). Due to the small size of the ensemble compared to the degrees of freedom of the NWP system, the resulting covariance matrix is rank deficient but is much easier to compute. The computational cost of EnKF, depending on the ensemble size, can be 10 to 100 times greater than 3DVar and is comparable with 4DVar. Unlike 4DVar, the development of a tangent linear model and its adjoint, whose code can be difficult to develop and maintain, is not required. Also, the assumption of a perfect model, which is required by 4DVar, is unnecessary, though EnKF does assume errors from different sources are unbiased. The convenience and flexibility of EnKF, and its ability to handle complex physics processes, such as multi-moment ice microphysics, has made it a popular DA algorithm for convective scale DA in recent years. Tong and Xue (2005) developed and integrated EnKF DA capabilities into the ARPS DA system. These capabilities have been improved and expanded over time. The ARPS EnKF DA system has been used for numerous convective scale DA experiments often involving radar data (Xue et al. 2006; Snook et al. 2011; Tanamachi et al. 2013; Supinie et al. 2016;

Supinie et al. 2017; Labriola et al. 2020). Therefore, it is chosen as the base DA system in this study.

Hybrid ensemble-variational techniques such as the hybrid ensemble-3DVar (En3DVar) promise improvements in analysis accuracy by combining dynamic flow-dependent background error statistics (from EnKF) with static flow-independent statistics (used by 3DVar or 4DVar) via a weighted average. These techniques were first developed by Hamill and Snyder (2000) and have been successfully implemented in subsequent convective scale real case studies (Li et al. 2012; Zhang et al. 2013; Pan et al. 2014; Shen et al. 2017; Kong et al. 2018; Kong et al. 2021). The hybrid EnVar involves a variational analysis step in addition to the EnKF DA, and is therefore more complex to implement and run, especially when new capabilities to assimilate additional data are needed. In this study, new capabilities to assimilate airborne Doppler radar and retrieved Raman lidar moisture profiles need to be developed. Therefore, we choose to use the more flexible EnKF DA system.

Weather radar is a key instrument whose data play a vital role in convective-scale DA and forecasting. Radars are capable of remotely observing storm structure and in-storm dynamical processes. The spatiotemporal resolution of radar data is often higher than data from other observing platforms. Of the variables observed by weather radar, those most commonly assimilated are radial velocity (V_r) and reflectivity (Z). Snyder and Zhang (2003; Zhang et al. 2004) were the first to assimilate simulated V_r of a supercell thunderstorm using EnKF. Tong and Xue (2005) were the first to assimilate simulated Z using a multi-class ice microphysics scheme. For real cases, EnKF DA of Weather Surveillance Radar-1988 Doppler (WSR-88D) data was first realized by Dowell et al. (2004) and has since become common in EnKF DA experiments. Unfortunately, due to their stationary nature, the distance between WSR-88D radars and storms of interest can result in low-resolution data or missing data coverage. Consequently, assimilation of data from specialized weather radars, including those from mobile radar observations or special dense radar networks, has been performed in addition to WSR-88D DA, to further improve analyses. Snook et al. (2011) conducted EnKF DA of stationary X-band Collaborative Adaptive Sensing of the Atmosphere (CASA) radar V_r and Z data and concluded that the assimilation of CASA radar data improved low-level circulations verses WSR-88D DA only. Tanamachi et al. (2013) performed EnKF DA of high-resolution mobile, X-band, polarimetric radar V_r data and determined that the tornadic like vortex was stronger and more intense in the associated analyses verses WSR-88D DA only. Supinie et al. (2016) completed EnKF DA of Mobile Weather Radar, 2005, X-band, Phased array (MWR-05XP) V_r data, collected during the second Verification of the Origins of Rotation in Tornadoes Experiment (VORTEX2), and reported improved mid-level rotation (mesocyclone) in the ensemble forecasts generated from experiment analyses. Supinie et al. (2017) carried out EnKF DA of S-band rapid-scan phased-array radar (PAR) data from the National Weather Radar Testbed via an EnKF system, and identified improvements in both the analyses and ensemble forecasts in the PAR experiment verses the WSR-88D only experiment. Additional EnKF DA has been conducted using data collected by airborne tail-Doppler radars (TDR). While TDR DA has been performed for several tropical cyclone related cases, using 3DVar (Xiao et al. 2009; Du et al. 2012; Li et al. 2022), EnKF (Weng and Zhang 2012; Davis et al. 2021; Hartman et al. 2021), and hybrid (Lu et al. 2017; Green et al. 2022) DA systems, to the author's knowledge, no TDR DA experiments have been performed for tornadic, convective scale storms.

Model state variables unobserved by radar, such as in-storm and near-storm temperature or moisture fields, can also be updated in radar EnKF DA via background error covariances.

However, while radar DA can provide valuable information about storm structure and internal storm dynamics, it is difficult for radar DA to update the environmental conditions of storms because their measurements are limited to the precipitating regions. The skill of forecasts initialized using analyses produced primarily from radar DA often decreases very quickly after initialization, since storm dynamics and thermodynamics in the analyses are often incompatible with the storm's environment (Fabry and Meunier 2020). For example, forecasts may degrade if planetary boundary layer (BL) conditions in the inflow region of the storm are not conducive for intense thunderstorms. Since observations are only available in precipitating regions, if an impact on the environment is desired, radar DA must project information tens to hundreds of kilometers away from the precipitating area. This requires the use of large ensemble background error covariance localization radii and the assumption that the correlation between errors at observed locations and unobserved locations is strong. If the correlation between these errors is weak, the impact of DA on unobserved locations will also be weak. Also, the error covariance between in-storm observations and locations in the storm environment estimated from the ensemble must be reliable, in order for the in-storm observations to correctly update the environmental conditions. This is usually difficult with a limited ensemble size. Furthermore, the influence of in-storm observations on the storm environment is often limited by the relatively small covariance localization radii used when assimilating in-storm radar observations. Small localization radii ensure that the analyzed fields are more reliable and contain more spatial structures.

Conventional observations, such as surface observations recorded by Automated Surface Observing System (ASOS) stations, Automated Weather Observing System (AWOS) stations, and radiosondes launched regularly by National Weather Service (NWS) Weather Forecast Offices (WFOs), sample environmental conditions and are assimilated in most NWP systems.

For example, Snook et al. (2015) found that the assimilation of surface, wind profiler, and upper-air observations in addition to WSR-88D and CASA radar data improved forecasts considerably. Unfortunately, surface observations are single point observations and thus do not provide information on the BL. Additionally, radiosondes are only launched twice daily (at 0000 UTC and 1200 UTC) and the WFOs from which they are launched are often located hundreds of miles apart, leading to low spatiotemporal resolutions in the data. Other surface-based observing systems sampling storm environments and BL conditions have been deployed in attempt to solve this problem, and their resulting data have been applied to DA experiments (Chipilski et al. 2022). One of these thermodynamic remote sensors is the microwave radiometer (MWR) (Vandenberghe and Ware 2002; Caumont et al. 2016). However, the low vertical resolution of MWR data precludes its use in convective DA. Another thermodynamic remote sensor is the Atmospheric Emitted Radiance Interferometer (AERI). Several studies have applied AERI data in convective DA with positive results (Coniglio et al. 2019; Hu et al. 2019; Chipilski et al. 2020; Degelia et al. 2020; Lewis et al. 2020). A third instrument developed more recently is the Raman lidar (RL). DA of retrieved temperature (Adam et al. 2016) and moisture (Grzeschik et al. 2008; Yoshida et al. 2022) fields from RL data has been shown to improve BL structure and forecasted precipitation. Data from related mobile remote sensors, including airborne compact RL (CRL), have been collected in a few field studies (Lin et al. 2023; Lin et al. 2024), but have not yet been utilized in DA experiments. Since data from these mobile instruments is denser in spatial resolution (along the flight tracks), being comprised of a series of profiles rather than a single profile, they have even greater potential to improve environment and BL conditions in DA analyses.

The collection of the special datasets used in DA often requires novel field campaigns. One such campaign is the Verification of the Origins of Rotation in Tornadoes Experiment Southeast (VORTEX-SE). VORTEX-SE was a program investigating the formation, intensity, structure, and path of tornadic storms in the southeastern United States (US). Research in this region is of particular importance since, due to several physical and social vulnerabilities, most tornado related US fatalities occur in southeastern states (Ashley 2007; Strader and Ashley 2018; Agee and Taylor 2019). During VORTEX-SE (2018) (VSE18), unique data were collected by a National Oceanic and Atmospheric Administration (NOAA) WP-3D (P3) Orion “Hurricane Hunter” aircraft, which recorded supercell storm structure and spatiotemporal heterogeneities in the BL via TDR and CRL instruments respectively (Hosek et al. 2023; Lin et al. 2023). In addition to data collected by the P3 aircraft, the University of Louisiana Monroe also had in operation an S-band radar (KULM) that collected near storm data at low levels ($\leq$ 3km). Special radiosondes were also launched from Minden, LA, and Monroe, LA, at strategic times during the campaign.

Building upon experiments conducted in the literature, the current study assimilates data collected during VSE18 to the Weather Forecasting and Research (WRF) model using the EnKF DA system available in the ARPS DA system. The VSE18 data used in this experiment was collected on the 13 April 2018 in northern Louisiana, during which time a cyclic, multi-tornado producing supercell passed near the city of Monroe. In addition to conventional and WSR-88D data, dual TDR V_r data, KULM V_r data, CRL-derived water vapor mixing ratio (q_v) profiles, and special soundings are assimilated in a series of experiments. Among these, data denial experiments are completed to determine the impact of each data type on the analyses.

Deterministic forecasts are conducted on ensemble mean analyses from each DA experiment to assess the impact of the DA on storm forecasts.

This study acts under the following hypothesis: *Experiments assimilating TDR V_r, KULM V_r, CRL q_v, and special sounding data will result in better analyses and forecasts than experiments assimilating conventional and WSR-88D data only.*

1.2 Uniqueness

Key aspects of this study that are unique:

- Previous studies have assimilated TDR data for real tropical cyclone cases, but none have assimilated TDR data for a real convective scale case. *In this study, for the first time, TDR V_r data are directly assimilated for a real tornadic supercell case.*
- While data from stationary, ground-based RL have been assimilated in several previous studies, none have assimilated airborne CRL data. *In this study, for the first time, airborne CRL q_v profiles are assimilated.*

1.3 Thesis Overview

The remainder of the thesis is organized as follows. Chapter 2: provides an overview of the 13 April 2018 severe weather and reviews the methodology utilized in the study. This includes descriptions of the WRF and ARPS EnKF systems and their parameter settings, the types of observations assimilated in DA, quality-control and formatting techniques used in data preprocessing, and DA experimental design. Chapter 3: discusses results, including the impact of assimilating VSE18 data on the analyses and prediction of the Monroe supercell storm. Chapter 4: details the conclusions of the study and outlines important issues that should be addressed in future work.

Chapter 2: Case Overview and Methodology

2.1 Overview of 13 April 2018 VORTEX-SE Case

Between the late afternoon of Friday, 13 April 2018, and early morning of Saturday, 14 April 2018, several severe thunderstorms impacted portions of southeast Oklahoma, northeast Texas, southern Arkansas, and northern Louisiana. Figure 2.1 depicts the first round of severe weather, which consisted of supercells, several of which were tornadic, that developed in northern Louisiana and southern Arkansas. These formed ahead of a quai-linear convective system (QLCS) which stretched from Magnolia, AR, to Natchitoches, LA. The second round of severe weather occurred over southeastern Oklahoma, Southwest Arkansas, and Northeast Texas and was also comprised of several tornado-producing supercells. The third round featured the QLCS, which produced some straight-line wind damage, and several tornadoes associated with a supercell embedded in the line. Over the two days, 18 tornadoes occurred, including two EF-0 tornadoes, twelve EF-1 tornadoes, and three EF-2 tornadoes. This study focusses on the cyclic, multi-tornado producing supercell which initiated southwest of Winnfield, LA in the evening of 13 April 2018, during the first round of severe weather. The cell followed a southwesterly trajectory, eventually becoming tornadic near the town of Monroe, LA (hereafter referred to as the Monroe supercell). The supercell produced three EF-1 tornadoes over the course of its lifetime, all of which were visually confirmed by the P3 aircraft in operation: (1) a tornado which occurred between 2334 – 2338 UTC (6:34pm – 6:38pm CDT) north of Calhoun, LA (hereafter referred to as the Calhoun tornado), (2) a tornado which occurred between 2343 – 2349 UTC (6:43pm – 6:49pm CDT) east of Downsville, LA (hereafter referred to as the Downsville tornado), and (3) a brief tornado which occurred between 0004 – 0006 UTC (7:04pm – 7:06pm CDT) West of Sterlington, LA (hereafter referred to as the Sterlington tornado).

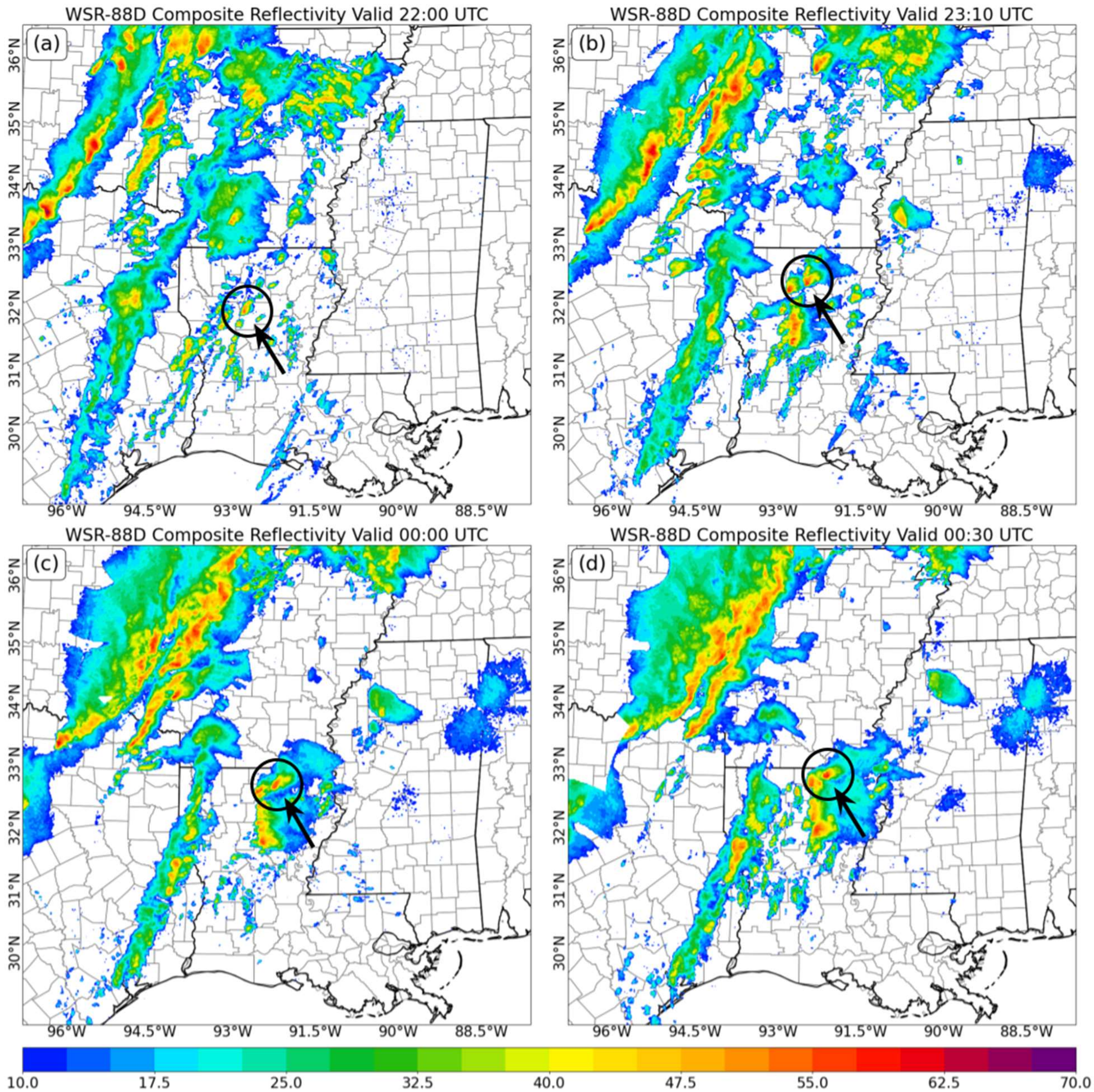

Figure 2.1: Composite reflectivity constructed from WSR-88D data within the 2500 m grid domain for (a) 2200 UTC on 13 April 2018, (b) 2300 UTC on 13 April 2018, (c) 0000 UTC on 14 April 2018, and (d) 0030 UTC on 14 April 2018. Circle and arrow mark the location of the Monroe supercell.

2.2 Forecast Model and DA System Overview

The ARPS EnKF DA system is chosen as the data assimilation system for the DA portions of the experiments. EnKF DA consists of two steps, (1) the ensemble forecast step and

(2) the EnKF analysis step. In the forecast step, each ensemble forecast member at a given time t_j is given by forecast equation

$$\mathbf{x}_i^b(t_j) = M_{j-1}\left(\mathbf{x}_i^a(t_{j-1})\right), i = 1, \ldots N \tag{2.1}$$

where $\mathbf{x}$ represents model state variables, superscripts a and b denote the analysis and background (forecast) fields respectively, subscripts i and j denote the ith ensemble member and jth time respectively, t is time, M is a dynamical model, and N is the number of ensemble members. The forecast error covariance, $\mathbf{P}^b$, is estimated from an ensemble of nonlinear model forecasts:

$$\mathbf{P}^b = \frac{1}{N-1}\sum_i^N \left(\mathbf{x}_i^b - \bar{\mathbf{x}}^b\right)^2. \tag{2.2}$$

The evaluation of $\mathbf{P}^b$ can be simplified in practice, since we do not necessarily need to evaluate $\mathbf{P}^b$ itself but rather its products with the linearized observation operator, $\mathbf{H}$, as shown in the following equations (Xue et al. 2006):

$$\mathbf{P}^b\mathbf{H}^T = \frac{1}{N-1}\sum_i^N \left(\mathbf{x}_i^b - \bar{\mathbf{x}}^b\right)\left[H\left(\mathbf{x}_i^b\right) - \overline{H(\mathbf{x}^b)}\right]^T, \tag{2.3}$$

$$\mathbf{H}\mathbf{P}^b\mathbf{H}^T = \frac{1}{N-1}\sum_i^N \left[H\left(\mathbf{x}_i^b\right) - \overline{H(\mathbf{x}^b)}\right]\left[H\left(\mathbf{x}_i^b\right) - \overline{H(\mathbf{x}^b)}\right]^T. \tag{2.4}$$

Here, $H\left(\mathbf{x}_i^b\right)$ is the model state background in observation space, also called the observed first guess or observed prior, for the ith ensemble member. $\overline{H(\mathbf{x}^b)}$ is the ensemble mean observed prior. In the assimilation step, we update both $\mathbf{x}_i^b$ and $\mathbf{P}^b$ using the following equations:

$$\mathbf{x}_i^a = \mathbf{x}_i^b + \mathbf{K}\left(\mathbf{y}^o - H(\mathbf{x}_i^b)\right) \tag{2.5}$$

$$\mathbf{K} = \mathbf{P}^b\mathbf{H}^T(\mathbf{H}\mathbf{P}^b\mathbf{H}^T + \mathbf{R})^{-1} \tag{2.6}$$

$$\mathbf{P}^a = (\mathbf{I} - \mathbf{K}\mathbf{H})\mathbf{P}^b \tag{2.7}$$

where $\mathbf{y}^o$ is the observations, $\mathbf{K}$ is the Kalman gain, $\mathbf{R}$ is the observation error covariance, $\mathbf{I}$ is the identity matrix, and $\mathbf{P}^a$ is the analysis error covariance. The resulting analysis state and the analysis error variance are used as the background state for the next forecast time (Eq. 2.1).

There are several specialized versions of EnKF. In general, each ensemble member is updated using equations 2.5, 2.6, and 2.7. However, their implementation can differ depending on the specific algorithm used. ARPS EnKF specifically utilizes the ensemble square root filter (EnSRF; Xue et al. 2000; Whitaker and Hamill 2002; Tong and Xue 2005; Xue et al. 2006). In this DA system, Eq. 2.5 becomes:

$$\overline{\mathbf{x}^a} = \overline{\mathbf{x}^b} + \mathbf{K}\left(\mathbf{y}^o - H\left(\overline{\mathbf{x}^b}\right)\right) \tag{2.8}$$

and

$$\mathbf{x}'^a_i = \beta(\mathbf{I} - \alpha\mathbf{K}\mathbf{H})\mathbf{x}'^b_i \tag{2.9}$$

where $\alpha = \left[1 + \sqrt{R(\mathbf{H}\mathbf{P}^b\mathbf{H}^T + R)^{-1}}\right]^{-1}$ and β is a covariance inflation factor. As is shown in equations 2.8 and 2.9, in the ARPS EnKF system the ensemble perturbations ($\mathbf{x}'^b_i$) and the ensemble mean ($\overline{\mathbf{x}^b}$) are updated individually.

Computation of the innovation in the ARPS EnKF system is made possible by observation operators (H in equation. 2.8). For a fixed ground-based radar, the observation operator calculates simulated radial velocity in observation space from model variables using equation (Xue et al. 2006):

$$V_r(u, v, w) = u \sin\phi \cos\mu + v \cos\phi \cos\mu + w \sin\mu \ , \tag{2.10}$$

where ϕ is the elevation angle and μ is the azimuth angle. u, v, and w are the model x, y, and z components of the wind respectively. For stationary radar, the location of the radar in cartesian coordinates is known and does not change with time. Therefore, the azimuth and elevation angles can be easily computed, using the following equations:

$$\phi = \arctan\left(\frac{y_g - y_r}{x_g - x_r}\right) + \frac{\pi}{2}, \tag{2.11}$$

$$\mu = \arctan\left(\frac{z_g}{\sqrt{(x_g - x_r)^2 + (y_g - y_r)^2}}\right) + \frac{\pi}{2}, \tag{2.12}$$

where x_g, y_g, and z_g are the coordinates of the model data grid point and x_r, y_r, and z_r are the coordinates of the stationary radar's location. For TDR data assimilated in this study, the P3 aircraft is mobile and therefore x_r, y_r, and z_r are not constant. This makes the calculation of elevation and azimuth angles slightly more complicated. When the TDR data were originally collected, the location of the P3 was logged at the time of observation for each observed data point. Thus, each data point in the observation has its own unique x_r, y_r, and z_r. ϕ and μ are calculated and appended to the TDR formatted data, as described in section 2.3. The ARPS EnKF system code was then modified to accommodate variable ϕ and μ for each data point.

The parameters and settings used in the ARPS EnKF system are outlined in Table 2.1. A nested grid setup is chosen for this experiment to better resolve small scale observed features in the analysis (see Figure 2.2). The outermost domain has a horizontal resolution of 2500 m and the nested domain has a horizontal resolution of 500 m. Grid domain sizes were chosen such that the storm(s) of interest fell inside the domains throughout the entire DA/ forecast period. Domain sizes were also chosen such that the grid points in the x and y directions had a common factor, with the grid points in the x direction being divisible by 18 and the grid points in the y direction being divisible by 17. This allowed for easy domain decomposition in parallel computation.

To generate the background for the first DA cycle, a 40-member ensemble was initialized at 1800 UTC on 13 April 2018 and spun up until 2200 UTC. The ensemble was generated by adding perturbations derived from the 1800 UTC Global Ensemble Forecast System (GEFS) to the 1800 UTC North American Model. The boundary conditions for the 2500 m domain were similarly derived. Localization radii for radar data are generally chosen to be 3 to 4 times the horizontal spacing of the formatted data. This is done so that the resulting analysis is not overly smooth. At its closest approach, the P3 aircraft was located approximately 30 km away from the Monroe supercell. Therefore, the horizontal localization radius for the CRL-derived q_v profiles is 30 km, which ensures that CRL data influence the storm's environment and not the properties of the supercell itself. The observation error standard deviations (OSED; σ_o) specified in the DA are meant to include instrument error, representativeness error, and other sources of error. For that reason, we assume a relatively large 3 m s^{-1} σ_o for WSR-88D and TDR data. A relatively small σ_o of 1 g kg^{-1} is used for the CRL data. As a result, the analysis near CRL observations is expected to closely fit observations. Multiplicative inflation, with a covariance inflation factor (β) of 1.1, is applied only to areas directly influenced by radar DA, to help maintain ensemble spread. Additionally, adaptive relaxation-to-prior spread inflation (Whitaker and Hamill 2012; Supinie et al. 2016) is applied everywhere, using an inflation factor (α) of 0.95, to help further maintain ensemble spread.

Table 2.1: EnKF DA settings for 2500 m (d01) and 500 m (d02) grids.

Parameter	Outermost domain (d01)	Nested domain (d02)
Grid size	$360 \times 340 \times 50$	$810 \times 765 \times 50$
Horizontal grid spacing	2.5 km	500 m
First cycle initial conditions	NAM	Outer domain at 2310 UTC
Boundary conditions	NAM	Outer domain analyses
Ensemble size	40	
Surface observation localization radii	Horizontal: 110 km Vertical: 3 km	
WSR-88D localization radii	Horizontal: 7.5 km Vertical: 3 km	Horizontal: 3 km Vertical: 3 km
WSR-88D σ_o	3 dbz, 3 ms^{-1}	
TDR and KULM localization radii	N/A	Horizontal: 2 km Vertical: 500 m
TDR σ_o	3 ms^{-1}	
CRL q_v retrieved soundings localization radii	Horizontal: 30 km Vertical: 200 m	
CRL q_v σ_o	1 g kg^{-1}	
Sounding localization radii	Horizontal: 150 km Vertical: 200 m	
Multiplicative covariance β	1.1 (only in areas where radar is assimilated)	
RTPS inflation α	0.95	

The forecast model utilized in this study is the WRF model: a non-hydrostatic model using an Arakawa C-grid, Runga-Kutta 3rd order time integration scheme, and 3rd order vertical and 5th order horizontal advection schemes. Version 4.3 of the WRF was used for this study, since initial experiments were conducted in 2022, before newer versions of the model became available. Table 2.2 details the WRF parameters and settings chosen for the forecast portions of the experiments. Here, the WRF uses a triple nested two-way grid setup. As in the DA portion of the experiments, domain sizes were chosen such that the storm(s) of interest fell inside the domains throughout the entire forecast period. The initial and boundary conditions for the 2500 m and 500 m grid domains are given by the ensemble mean analyses produced during DA experiments. The horizontal resolution for the innermost nested domain was chosen to be 100 m, which is sufficiently high to resolve tornadic vortices (see Figure 2.2). For simplicity, the timestep decreases proportionally with decrease in grid size between domains, ensuring the timestep is always less than $6dx$, as recommended.

Table 2.2: WRF model settings for the 2500 m (d01), 500 m (d02) and 100 m (d03) domains.

Parameters	Outermost domain (d01)	First nested domain (d02)	Innermost nested domain (d03)
Grid size	$360 \times 340 \times 50$	$810 \times 765 \times 50$	$1800 \times 1870 \times 50$
Horizontal grid spacing	2.5 km	500 m	100m
Time step	5 s	1 s	0.5 s
Initial Conditions	Ensemble mean analysis	Ensemble mean analysis	First nested domain ensemble mean analysis
Boundary Conditions	NAM	Outer domain ensemble mean analysis	First nested domain ensemble mean analysis
Feedback	Two-way feedback		
Land surface	Noah land surface model		
Microphysics	Thompson et. al scheme		
Radiation	RRTMG scheme		
Vertical PBL mixing	Yonsei University Scheme	Off	
Subgrid-scale Turbulence	Horizontal Smagorinsky 1st order closure	1.5-order TKE closure (3D)	

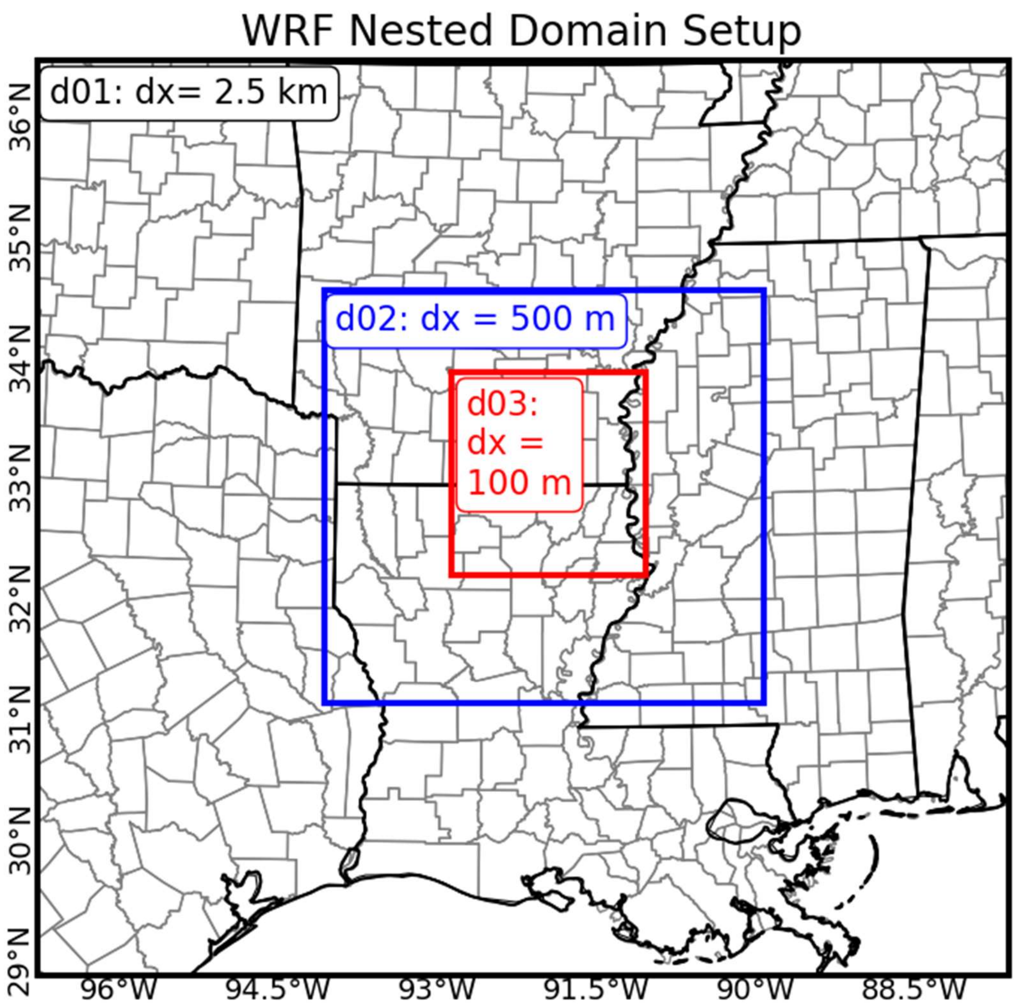

Figure 2.2: The location of the outermost (2500 m) (d01), first nested (500 m) (d02), and innermost nested (100 m) (d03) domains used in the WRF model and ARPS EnKF DA system.

2.3 Data Overview, QC, and Formatting

Of the conventional observations available, 5-minute regular observations recorded by ASOS stations within each gridded domain were used. 72 stations are located within the 2500 m grid domain (Figure 2.3) and 17 stations are located within the 500 m grid domain (Figure 2.4). There are on average approximately 31 surface observations available for any given DA cycle within the 2500 m grid domain. There is an average of approximately 7 surface observations available for any given DA cycle within the 500 m domain.

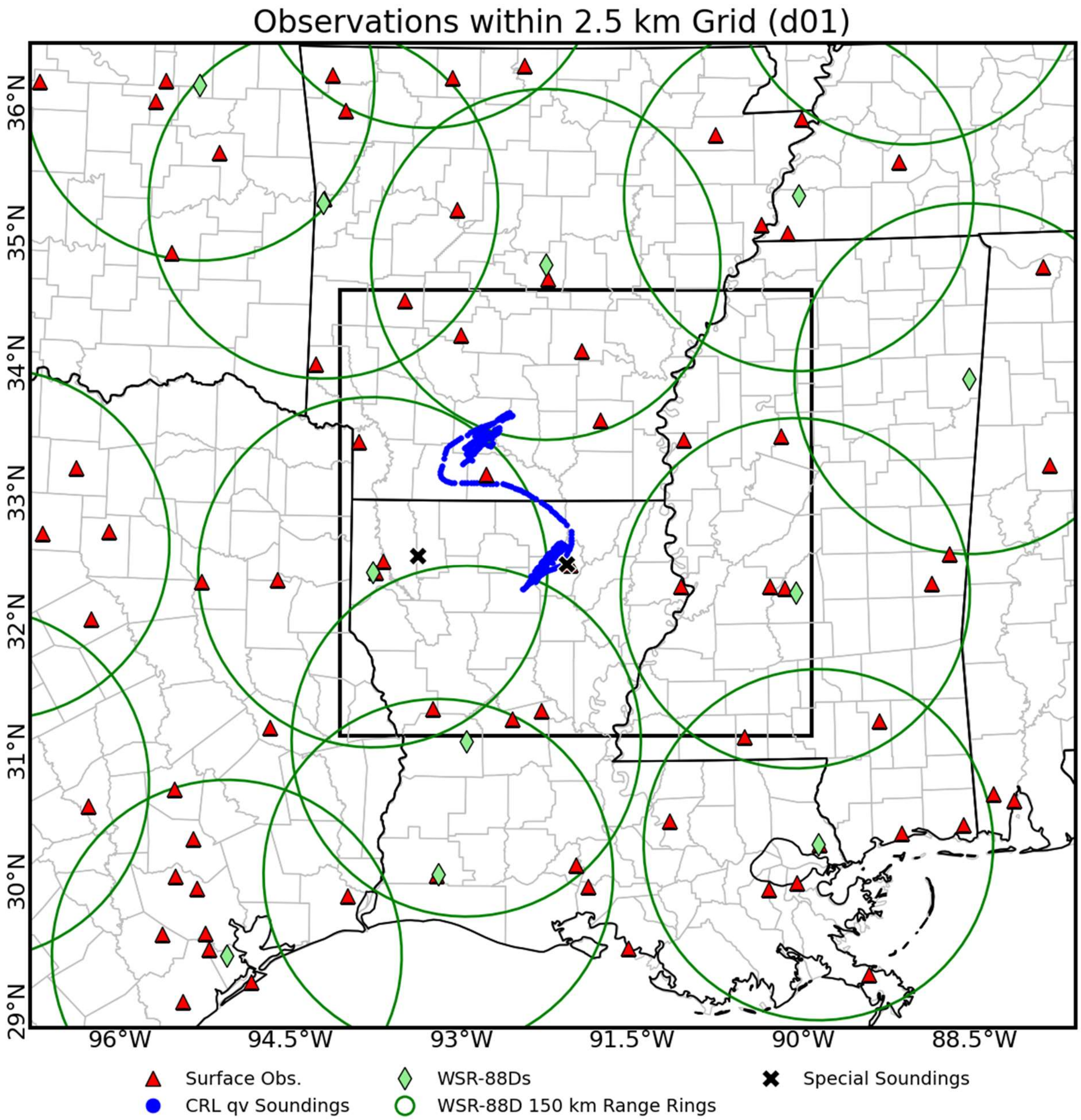

Figure 2.3: Observations located within the 2500 m grid domain. Red triangles indicate surface observation locations. Green diamonds and green circles indicate the locations of WSR-88D radars and their 150 km range rings respectively. Blue dots show the locations of CRL q_v soundings. Black Xs indicate the locations of special soundings launched at Minden, LA (left) and Monroe, LA (right).

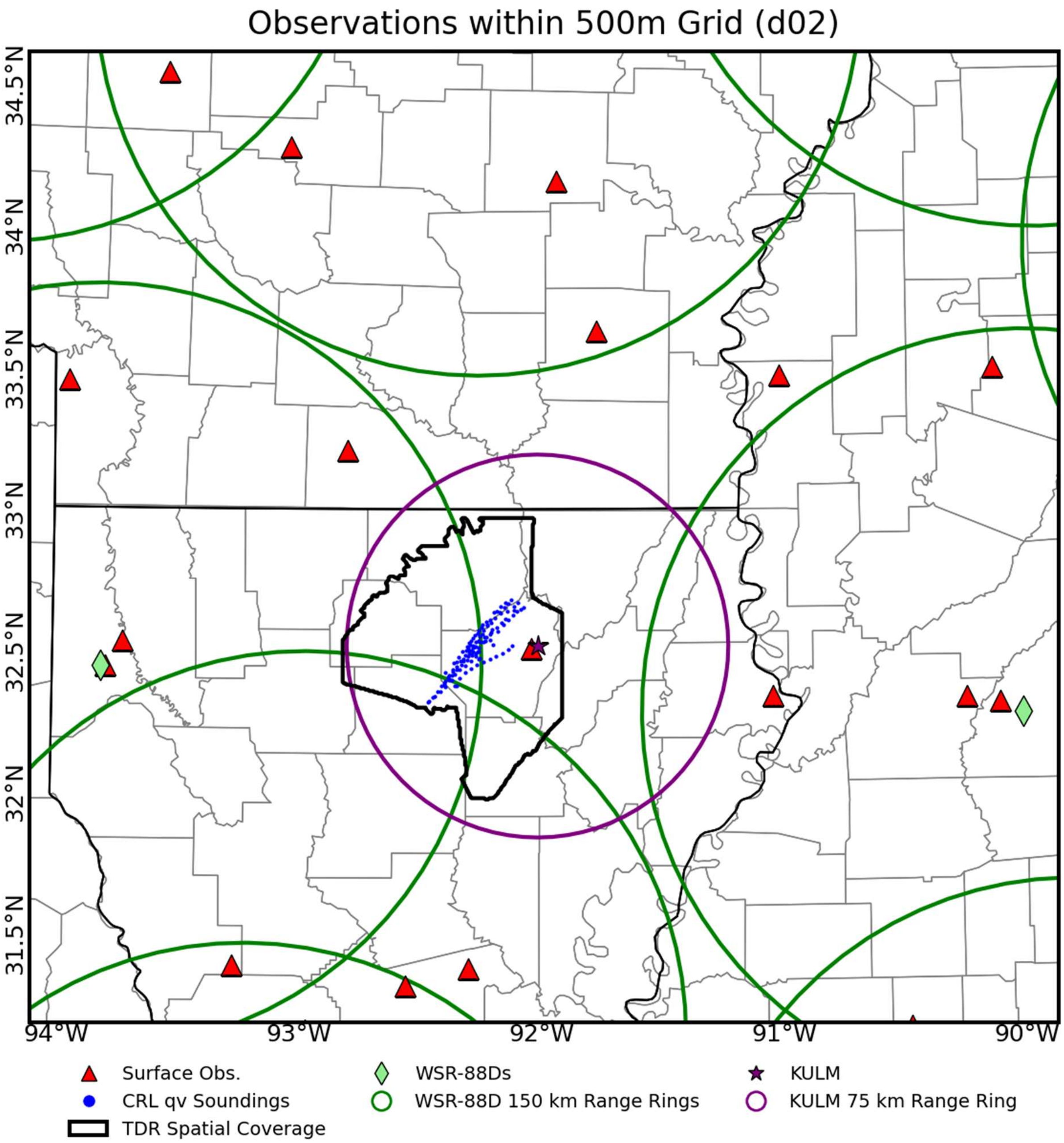

Figure 2.4: Observations located within the 500 m grid domain. Red triangles indicate surface observation locations. Green diamonds and green circles indicate the locations of WSR-88D radars and their 150 km range rings respectively. Blue dots show the locations of CRL q_v soundings. The purple star and purple circle indicate the location of the KULM radar and its 75 km range ring respectively. The black contour indicates the composite spatial coverage of assimilated TDR data across all cycles.

Data from 15 WSR-88Ds are used in DA on the 2500 m grid (Figure 2.3). Data from 9 of those radars are also used in DA on the 500 m grid (Figure 2.4). The data were obtained in binary format from the National Centers for Environmental Information (NCEI) radar data archives. Data were converted to “column-tilt” format by performing bilinear interpolation to horizontal model grid points. As shown in Figure 2.5, the interpolated radar data is still located on a radial, or tilt, and has associated interpolated elevation (ϕ) and azimuth (μ) angles. However, the formatted data is regularly spaced along the radial and therefore falls into a “column” on model grid points. This process was completed for both the 2500 m and 500 m grid resolutions. By formatting the data, the reading of radar data by the ARPS EnKF system is greatly simplified. All available WSR-88D Z data are assimilated, regardless of their value, thereby removing as much spurious convection from the analysis as possible. V_r data are only assimilated in areas where Z is greater than or equal to 10 dBZ (Putnam et al. 2019), thereby removing velocities derived from the movement of non-meteorological objects.

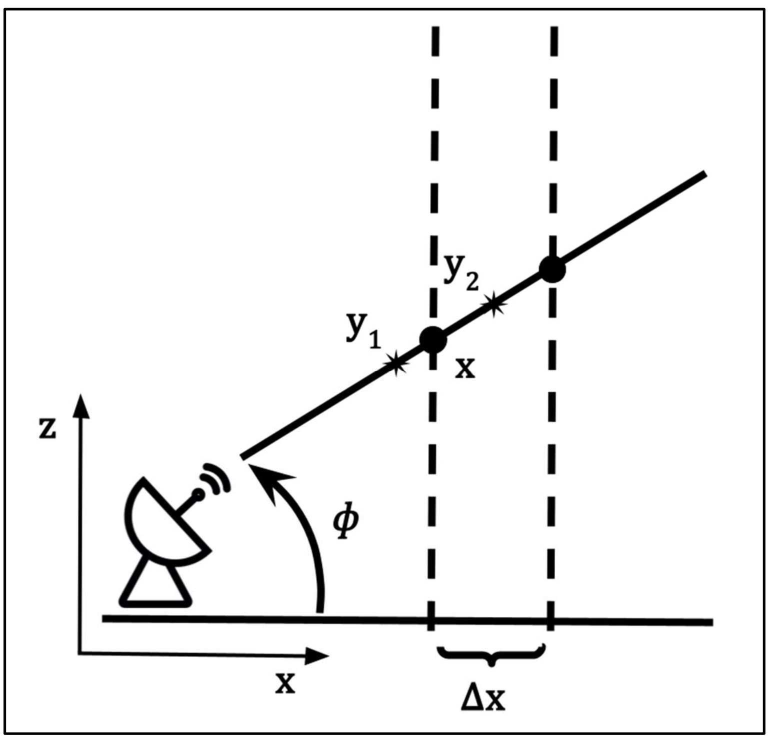

Figure 2.5: A schematic demonstrating the method by which "column-tilt" formatted data is created. y_1 and y_2 are original locations of radar data points. x is the interpolated radar data located on regular horizontal model grid points.

The CRL used in VSE18 is a downward-pointing lidar on board a P3 aircraft which collects vertical profiles of water vapor, aerosol, and temperature at fine resolutions within the BL (Figure 2.6; Liu et al. 2014; Wang et al. 2016; Wu et al. 2016; Lin and Wang 2023). The average altitude of the P3 flight track is approximately 1 km above ground level (AGL), and thus CRL data are only available below 1 km. The original profile data have a vertical resolution of 1.2 m and a horizontal resolution of approximately 360 m along the flight tracks. The CRL data's horizontal resolution is calculated by multiplying the average P3 flight speed of 120 m s^{-1} by the CRL sampling interval of approximately 3 seconds. Measurement errors in CRL profiles can be attributed primarily to calibration and random errors (Wu et al. 2016). To prepare for DA, data profiles are averaged along the P3 flight path to profiles with a horizontal spacing of approximately 2.5 km. Since the resolution of the original CRL data is much higher than the vertical resolution of the WRF model grids, the profiles were vertically thinned to a final vertical resolution of 60 m. While information is lost in the thinning process, the details in the original profiles cannot truly be resolved by the model grid, and thinning helps reduce potential observation overfitting issues. In a previous, related dataset collected by the VSE18 CRL, Hosek et al. (2023) discovered areas of unphysically large supersaturation near the surface in relative humidity derived from CRL temperature data. They determined that the high values of relative humidity were the result of low-bias errors within the temperature profile data, and therefore concluded that the CRL-retrieved temperature data are less reliable. Consequently, CRL-derived temperature profiles are not assimilated in this study. After formatting, an average of approximately 12 CRL-derived q_v profiles are available for assimilation on both the 2500 m and 500 m grids for each DA cycle. The location of all assimilated CRL q_v profiles on the 2500 m and 500 m grids is shown in Figure 2.3 and Figure 2.4 respectively.

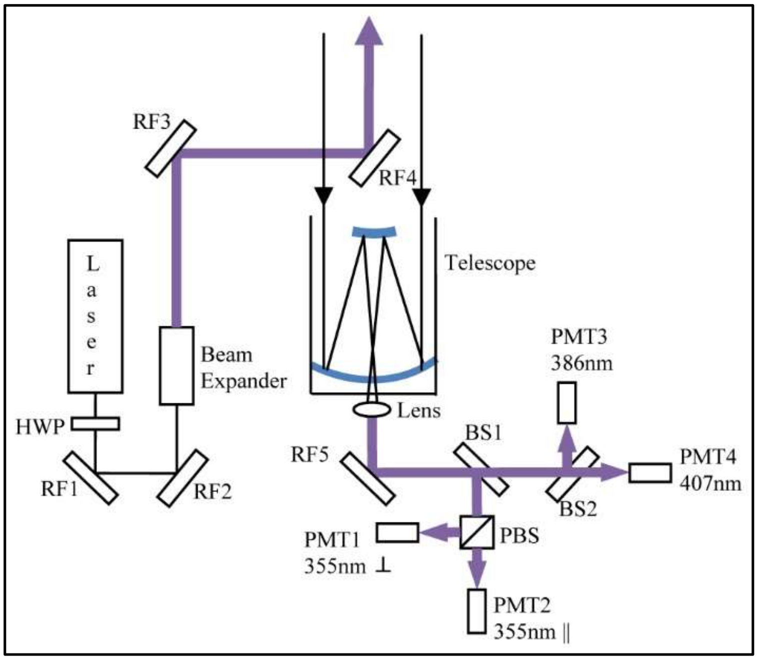

Figure 2.6: Schematic of the CRL instrument. Taken from Fig. 2 of Liu et al. (2014).

Dual TDRs operated simultaneously aboard the NOAA P3 aircraft during VSE18 (Jorgensen et al. 2017; Ziegler et al. 2018; Ziegler 2019; Ziegler et al. 2025a). The dual TDRs are each single-polarization 3.2 cm (X-band) radars, consisting of a forward-pointing TDR-fore (TFOR) radar and a backward-pointing TDR-aft (TAFT) radar. Both radars perform simultaneous vertically oriented scans, with the TFOR and TAFT radars oriented 20° from a plane normal to the P3 fuselage in the forward and aft directions respectively (Figure 2.7; Bluestein et al. 1997). In contrast, earlier P3 observations from the VORTEX project (Bluestein et al. 1997; Ziegler et al. 2001) obtained degraded spatial resolution measurements in which a single radar conducted a Fore-Aft Scanning Technique (FAST) by alternately transmitting-receiving on the foreward- and aft-pointing antennas on the side of the P3 where the storm was located. Due to the aircraft ground speed, the shape of the resulting scans is slightly helical instead of purely conical. Each TDR has a 2° half-power beamwidth, an extended Nyquist velocity of 49.9 m s^{-1}, and a ~ 3-5 min volume scan time corresponding to the length of the successively reversing straight, level legs flown along the inflow storm flank. The combined spatial coverage of all available TFOR and TAFT is shown in Figure 2.4. The neighboring TFOR and TAFT volume scans overlap owing to aircraft motion, providing a minimum of dual-TDR data coverage in the region of overlapping sweeps and single-TDR coverage outside the overlap region (Figure 2.8a). At the radar antenna rotation rate of 20 revolutions per min (a full 360 deg revolution every 3 s) and a nominal ground speed of 115 m s^{-1}, the along-track effective radar gate spacing is ~ 0.35 km.

The TDR data has several unique features that make them desirable for use in DA. When the Monroe supercell became tornadic, it was located more than 125 km away from the nearest WSR-88D radars. As a result, the WSR-88D data does not contain any information on the low levels of the Monroe supercell storm. The P3 flight path places the TDRs ~10-15 km or less away from the storm, much closer than any WSR-88D. Furthermore, the beam of the TDR can point slightly downward, as it completes its volume scan. These features allow the TDR to sample the low-level structure of the supercell much more accurately than WSR-88Ds. Note that although the vertical coverage of the Monroe supercell by the TDR is complete above the lowest ~ 0.3 km AGL, and although the TDR data coverage of the storm core is complete in the along-track direction, the forward stratiform (anvil) region is only partially sampled.

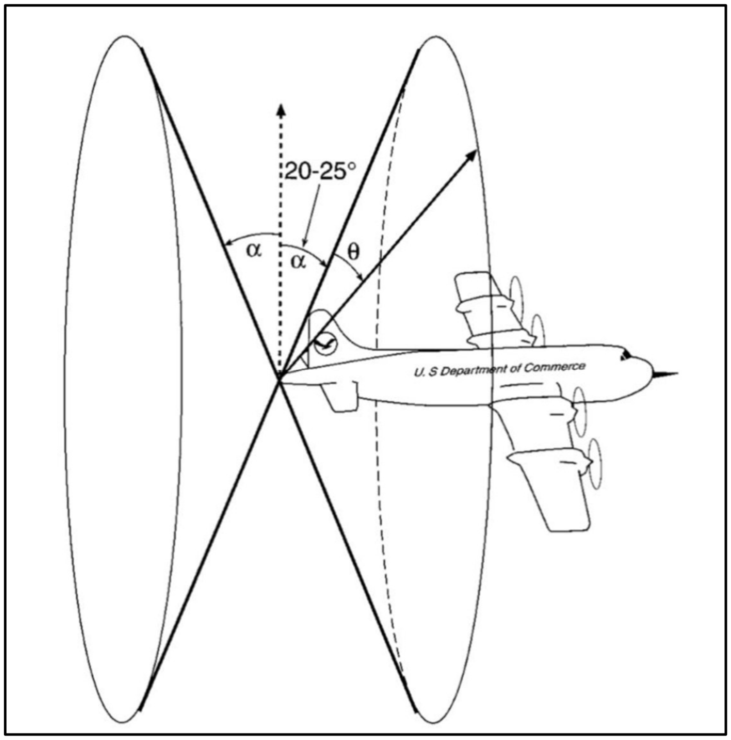

Figure 2.7: Scanning procedure for the P3 mounted TDR radar. θ is an angle representing the rotation of the radar beam around the flight track. α is the angle made by the sweep and the plane orthogonal to the flight track. Figure from Bluestein et al. (1997).

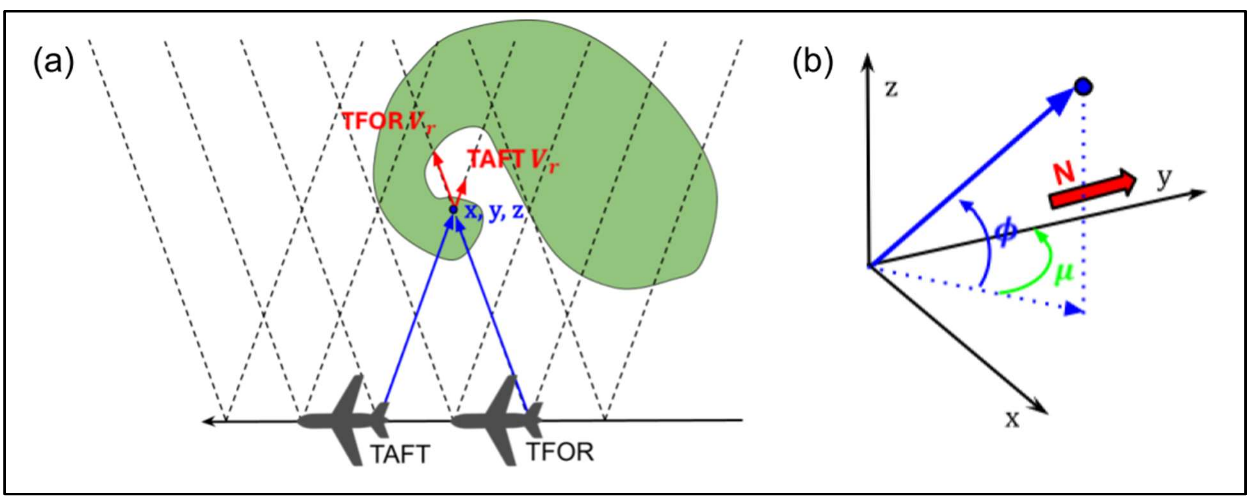

Figure 2.8: (a) The network of intersecting TAFT and TFOR radar beams (black dashed lines), demonstrating the resultant dual-TDR coverage (where lines intersect) and single-TDR coverage near the ends of each flight leg. (b) The elevation and azimuth angles of a given data point in the TDR data.

The University of Louisiana-Monroe operated a WSR-88D-equivalent dual-polarization 10.2 cm (S-band) Doppler radar (KULM) with a 0.93° half-power beamwidth, a Nyquist velocity of 25.4 m s^{-1}, and a volume scan time of about ~ 2 min during this severe weather event (Murphy 2018; Ziegler et al. 2018; Murphy et al. 2019; Ziegler et al. 2025a) During the period 2312 UTC on 13 April to 0020 UTC on 14 April 2018 in which the close-range dual-TDR and KULM observations of the Monroe supercell were obtained, the nearest WSR-88D was located more than 125 km away from the storm while KULM was located within ~45 km of the storm at 2312 UTC and within ~ 30-35 km of the storm throughout its tornadic phase in the period ~ 2332-0005 UTC. KULM collected data at 0.7°, 1.8°, 3.1°, 4°, and 5.1° elevation angles (i.e., at and below approximately 3 km AGL around the range of the storm) with the project objective of increasing time resolution of low- and midlevel storm rotation and divergence profiles (Todd Murphy, personal communication, 2018). KULM being at about twice the range from the storm but with about half the half-power beamwidth relative to the TDRs, KULM and TDR data comparably resolve the Monroe supercell at low levels, whereas KULM only partially cover the storm vertically. Storm core observations are thus up to triple-Doppler below 3 km AGL and up to dual-TDR above 3 km AGL.

The editing and analysis procedures for TDR and KULM data (Ziegler et al. 2025a) as applied to this study are similar to those performed by Hosek et. al. (2023) and Ziegler et al. (2025b). Bulk editing of the TDR data was done using a modified Python ARM Radar Toolkit (Py-ART; Helmus and Collis 2016) script that combines dual-PRF processor error correction (Alford et al. 2022) with numerous additional editing functions for removal of ground returns, noisy precipitation signal, and clear air noise from both airborne and ground-based radars (D. Stechman and Conrad Ziegler, personal communication, 2023). Prior to bulk editing, aircraft motion was removed from V_r data using the National Center for Atmospheric Research (NCAR) SOLO3 software. After the bulk editing was complete, data were manually investigated and additional de-aliasing, noise filtering, and ground clutter removal were performed where necessary using the SOLO3 software. The editing and analysis of KULM data are essentially equivalent to the methods used for TDR data, with bulk editing conducted using the modified Py-ART script and additional dealiasing and noise filtering performed within SOLO3 software package. An additional statistical masking technique was preapplied to the raw KULM data to remove ground targets.

A two-pass Barnes objective analysis (Majcen et al. 2008) was applied by Conrad Ziegler to interpolate all dual-TDR and KULM data to a 3-D fixed, ground-relative regular Cartesian grid domain (personal communication, 2023). The analysis domain had (x, y, z) dimensions of 85 km x 110 km x 15 km, a 250 m grid spacing in all directions, and the z-origin located at ground level. Considering KULM observations at 50 km range to have the coarsest (range-dependent) effective gate spacings, the smoothing parameter κ_0 = 1.3541, while the convergence parameter γ = 0.2. Due to terrain beam blockage issues to the north of KULM, combined with north-northeasterly storm motion, the dual-TDR and KULM data were not objectively analyzed after 0020 UTC on 14 April 2018 owing to poor KULM low-level sampling. In preparation to assimilate these radar analyses, their data were retained on the original grid points in the vertical but regridded to the 500 m horizontal model grid points via bilinear interpolation.

Two special soundings were recorded via radiosonde launches at Minden, LA and Monroe, LA during the DA window on the 2500 m grid (Figure 2.3). The Monroe sounding was launched at 2226 UTC and Minden sounding was launched at 2231 UTC. The file structure and metadata of the soundings was altered, allowing them to be read by the APRS EnKF system.

However, the variables and resolutions of the original soundings were preserved. For the Minden sounding, points in the profile are separated by an average of 23.6 m, with a minimum distance of 15.6 m and a maximum distance of 37.6 m. For the Monroe sounding, points in the profile are separated by an average of 30.4 m, with a minimum distance of 22.2 m and a maximum distance of 37.1 m. The profiles contain pressure, temperature, dewpoint, wind speed, and wind direction data, all of which are assimilated in the associated experiments.

2.4 Experiment Design

Table 2.3 outlines the five DA experiments conducted in this study: (1) a control experiment in which no special VSE18 data are assimilated (CNTRL), (2) an experiment assimilating additional CRL q_v data (AIRL), (3) an experiment assimilating additional TDR and KULM V_r data (AIRV), (4) an experiment assimilating additional TDR V_r, KULM V_r, and CRL q_v data (AIRVL), and (5) an experiment assimilating additional TDR V_r, KULM V_r, CRL q_v, and special sounding data (AIRVL+S). All experiments also assimilate conventional observations and WSR-88D Z and V_r observations, as in CNTRL. The DA period is comprised of 25 DA cycles performed at 5-minute intervals from 2200 UTC on 13 April 2018 to 0000 UTC on 14 April 2018 (Figure 2.9). The 2500 m grid is run for all cycles. Since TDR data is unavailable before 2310 UTC and several features of interest (including the three tornados that were produced by the Monroe Supercell) occur after 2310 UTC, the 500 m grid is spun up during the forecast step of cycle 14 (2305 UTC) using interpolated 2500 m grid ensemble analyses from cycle 14 as initial conditions. DA on the 500 m grid begins with cycle 15 (2310 UTC) and is performed for all subsequent cycles. Surface observations are assimilated on both the 2500 m and 500 m grids, providing information on low level temperature, moisture, and pressure fields. WSR-88D Z and V_r data are likewise assimilated on both the 2500 m and 500 m grids, providing information on precipitation and wind related parameters respectively. For the AIRL, AIRVL, and AIRVL+S experiments, the CRL q_v data are assimilated on both the 2500 m and 500 m grids when able, providing moisture information in the boundary layer. For the AIRV, AIRVL, and AIRVL+S experiments, the TDR and KULM data are only assimilated on the 500 m grid, providing information on the mesocyclone and tornadic circulations within the supercell.

Table 2.3: List of DA experiments and the data types assimilated in each experiment.

Name	Conventional and WSR-88D	CRL q_v	TDR V_r	KULM V_r	Special Soundings
CNTRL	Yes	No	No	No	No
AIRL	Yes	Yes	No	No	No
AIRV	Yes	No	Yes	Yes	No
AIRVL	Yes	Yes	Yes	Yes	No
AIRVL+S	Yes	Yes	Yes	Yes	Yes

Deterministic forecasts are run using ensemble mean analyses as initial conditions for each cycle starting with cycle 17 (2320 UTC). For those experiments that assimilate TDR and KULM V_r data, this allows information from at least 3 DA cycles of TDR and KULM DA to be included in the forecast's initial conditions. Since the Monroe supercell storm tended to lose supercellular characteristics in trial forecasts runs before 0030 UTC, each official forecast ends on 14 April 2018 at 0030 UTC regardless of when it is initialized, thereby conserving computational resources.

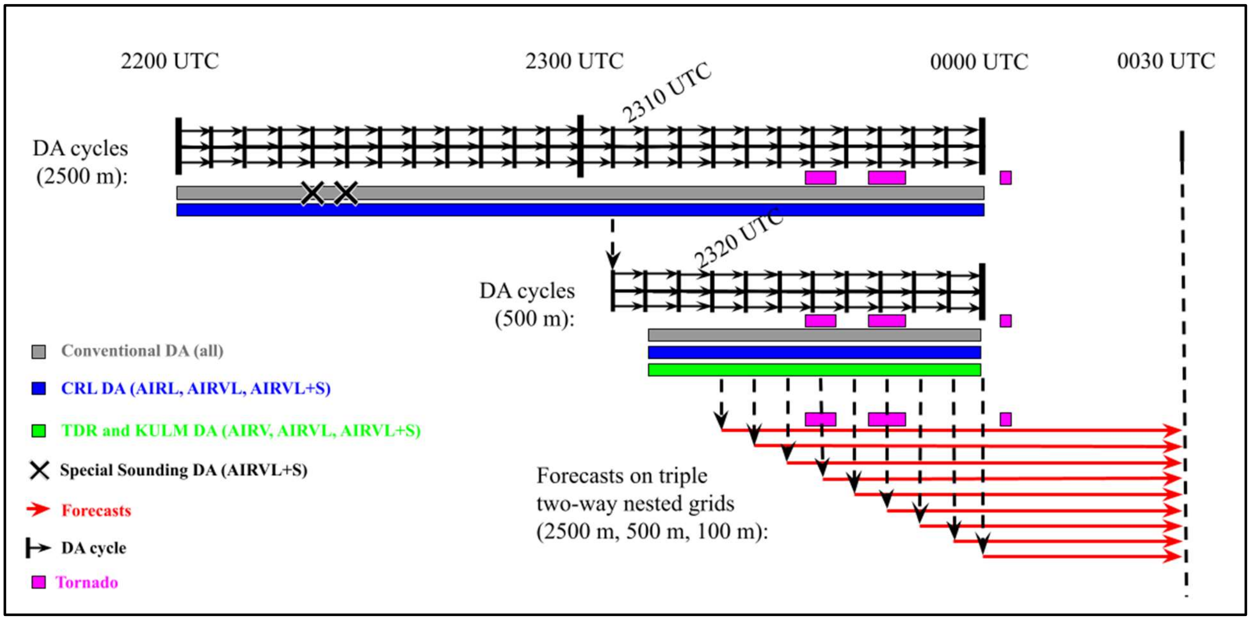

Figure 2.9: Experiment timeline. Vertical tick marks and black arrows indicate the DA and forecast steps for EnKF DA cycles respectively. Colored bars denote the types of DA performed on corresponding grids, including surface observations and WSR-88D DA (gray), CRL DA (blue), and TDR and KULM DA (green). Xs mark when special sounding DA occurs. Vertical dashed arrows designate the spin up of a nested grid. Red arrows represent deterministic forecasts. The temporal extent of tornado tracks shown by purple colored bars.

Chapter 3: Results

3.1 Impact of DA on Storm Analyses

The direct impact of DA on the analyzed fields on the 2500 m and 500 m grids is evaluated quantitatively using calculated statistical quantities in observation space, i.e., innovation statistics, similar to those outlined in Dowell and Wicker (2009), though they differ slightly. The calculation of the root-mean-square innovation (RMSI) is done using the equation

$$RMSI = \sqrt{\frac{1}{M}\sum_{m=1}^{M}(d)^2} \qquad (3.1)$$

where the innovation d is given by the equation

$$d = y^o - H\left(\overline{x^b}\right) \quad or \quad d = y^o - H\left(\overline{x^a}\right) \qquad (3.2)$$

for the ensemble mean background $\overline{x^b}$and ensemble mean analysis $\overline{x^a}$, respectively. M in (3.1) denotes the number of observation points assimilated. Unlike in Dowell and Wicker (2009), the volume mean innovation is not removed in the calculation of RMSI . RMSI provides an overall measure of the difference between the observation and the background or analysis. RMSI helps determine how well the DA algorithms can incorporate the information provided by observations. If DA is successful, the distance from observations should be greater in the background than in the analysis. Therefore, RMSI of the analysis should be lower than RMSI of the background at any given time. If the decrease in RMSI after DA is smaller than expected, it indicates the inability of the DA algorithm to adequately fit the background to the observations.

The average ensemble spread is calculated by taking the square root of the average ensemble variance (Fortin et al. 2014) using equation

$$spread = \sqrt{\frac{1}{M}\sum_{m=1}^{M}\left[\frac{1}{N-1}\sum_{n=1}^{N}\left[H(x_{n,m}) - H(\overline{x_{n,m}})\right]^2\right]} \qquad (3.3)$$

where N is the number of ensemble members. Here, the observation error variance is excluded from the spread calculation. Together with RMSI, the ensemble spread can help determine if the ensemble is properly dispersed. Recall, the background error covariance in EnKF is estimated using the ensemble spread (Eq. 2.2). RMSI is an estimate of the background error plus the observation error. Using these relationships, a consistency check, or a consistency ratio (CR; Dowell et al. 2004), can be calculated by dividing the sum of the observation error variance and the ensemble variance by the mean-square innovation:

$$CR = \frac{\sigma_o^2 + spread^2}{RMSI^2} = \frac{\left(\sigma_o^2 + \frac{1}{M}\sum_{m=1}^{M}\left[\frac{1}{N-1}\sum_{n=1}^{N}\left[H(x_{n,m}) - H(\overline{x_{n,m}})\right]^2\right]\right)}{\frac{1}{M}\sum_{m=1}^{M}(d)^2}. \qquad (3.4)$$

If the ensemble spread is too small, i.e. the ensemble is under-dispersed, the CR will be less than 1. If the ensemble spread is too large, i.e. the ensemble is over-dispersed, the CR will be greater than 1. An under-dispersed ensemble can prevent the DA from properly fitting the background to observations. An over-dispersed ensemble can cause observation overfitting.

Bias is calculated from the average of the negative innovation:

$$bias = \frac{1}{N}\sum_{n=1}^{N}(-d)\,. \tag{3.5}$$

Here, bias refers to the average difference between model state and observations. It can be used to determine how DA fits the background state to observations. If bias is negative, DA will act to increase associated values in the analysis. If bias is positive. DA will act to decrease associated values in analysis.

Since this study examines a convective scale case, the points used in innovation statistics are filtered to focus mainly on areas of convection. In related studies, this is done by only considering points where observed Z is greater than or equal to 15 dBZ (Snook et al. 2011). In this study, since V_r DA occurs at locations where observed Z is greater than or equal to 10 dBZ, and all Z observations are assimilated regardless of their value, a threshold of 10 dBZ is chosen instead of 15 dBZ for WSR-88D Z, WSR-88D V_r, KULM V_r, and TDR V_r data innovation statistics.

3.1.1 Comparison of Analyses on the 2500 m Grid

The results shown in Figure 3.1 and Figure 3.2 demonstrate successful assimilation of WSR-88D Z data on the 2500 m grid domain. Since TDR data is not assimilated until cycle 15 (2310 UTC) on the 500 m grid, the CNTRL and AIRV innovation statistics for cycles 1-14 are very similar. The same is true for AIRL and AIRVL innovation statistics. Since the first special sounding is assimilated at 2225 UTC (cycle 6) for the AIRVL+S experiment, innovation statistics for cycles 1-5 of the AIRVL and AIRVL+S experiments are identical. Across all experiments, a decrease in RMSI after the DA step occurs in each EnKF DA cycle, indicating successful fitting of the analysis to the observation by the DA. WSR-88D Z biases for the backgrounds of each cycle are generally positive, especially for earlier cycles, indicating higher reflectivity in the backgrounds relative to the observation. This is further confirmed when comparing Figure 3.2 to Figure 2.1. Spurious convection is clearly present in the model backgrounds (Figure 3.2a and Figure 3.2d verses Figure 3.2b and Figure 3.2e respectively), especially for the first cycle (2200 UTC; Figure 3.2a), and is removed across several regions in the resultant analysis (see spatial extent of negative analysis increments in Figure 3.2c and Figure 3.2f). The variation in RMSI, ensemble spread, and bias trends downward with an increase in DA cycle. This suggests the ensemble is under-dispersed. The consistency ratio confirms this inference; the ensemble begins relatively well dispersed, with a CR value of approximately 0.8, but becomes under-dispersed with time, as shown by a decrease in CR with increase in DA cycle, plateauing around a value of 0.4. This under-dispersion could be the result of a small assumed observation standard error deviations (OSED; σ_o). Some studies have used larger OSED, resulting in a better dispersed ensembles. However, the Z OSED used in this study (3 dBZ; Table 2.1) has been used in several other related studies and should be a reasonable representation of the errors inherent in the WSR-88D Z data. As mentioned in section 2.2, both multiplicative and RTPS inflation are implemented in areas affected by radar DA. Relatively large values for β and α respectively are used in inflation, and, therefore, additional covariance inflation is not reasonable. Fortunately, previous EnKF DA studies have indicated that an under-dispersed ensemble does not necessarily result in degraded analyses (Supinie et al. 2016).

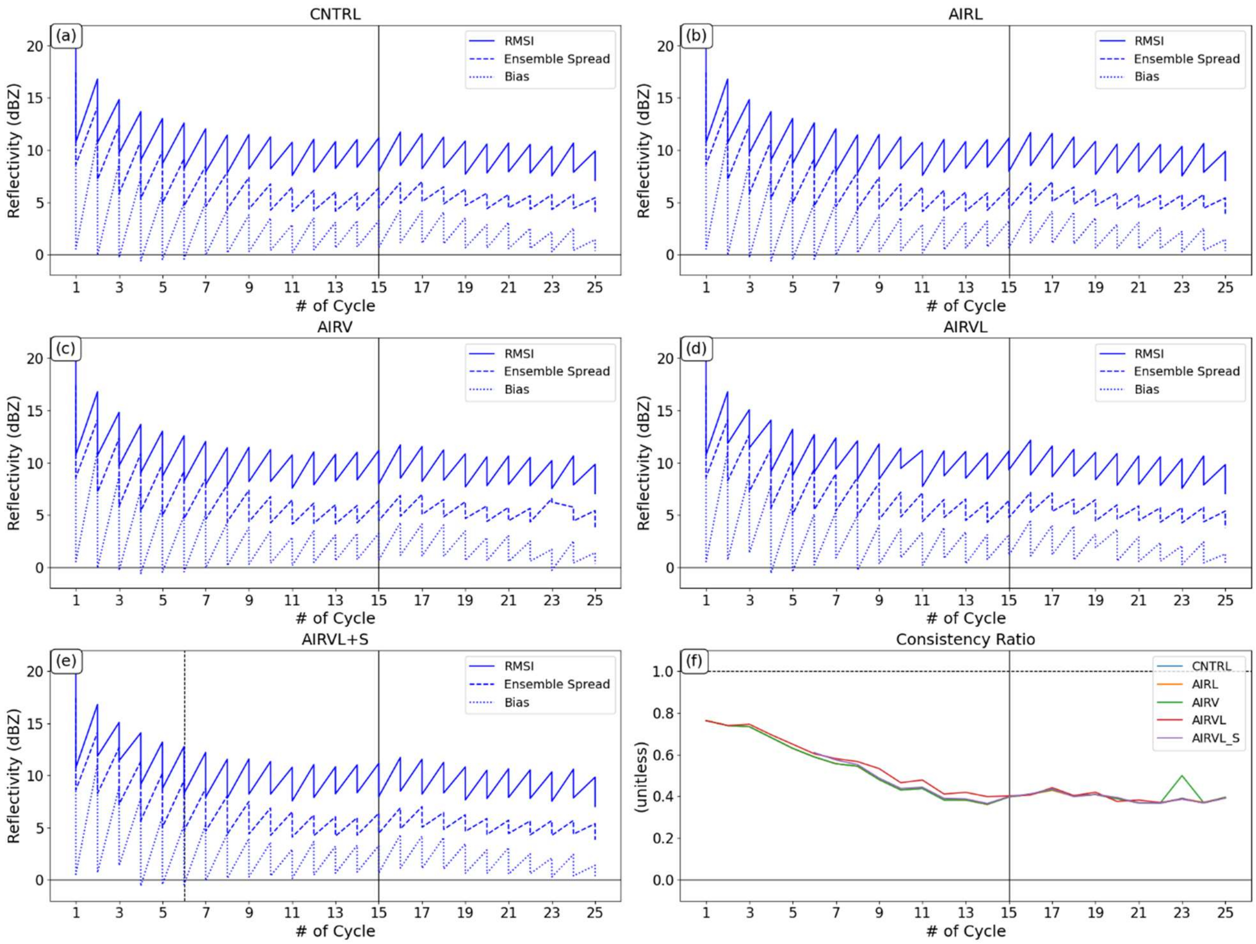

Figure 3.1: Sawtooth diagram displaying RMSI (solid blue), average ensemble spread (dashed blue), and bias (dotted blue) for WSR-88D *Z* data on the 2500 m grid for the (a) CNTRL, (b) AIRL, (c) AIRV, (d) AIRVL, and (e) AIRVL+S experiments. The dashed black line marks the first DA cycle for which a special sounding is assimilated. The solid black line indicates the first cycle for which TDR data is assimilated on the 500 m grid. (f) The consistency ratio for CNTRL (blue), AIRL (orange), AIRV (green), AIRVL (red), and AIRVL+S (purple) experiments. A horizontal dashed black line is provided at CR=1 to help in diagnosing over- or under-dispersion.

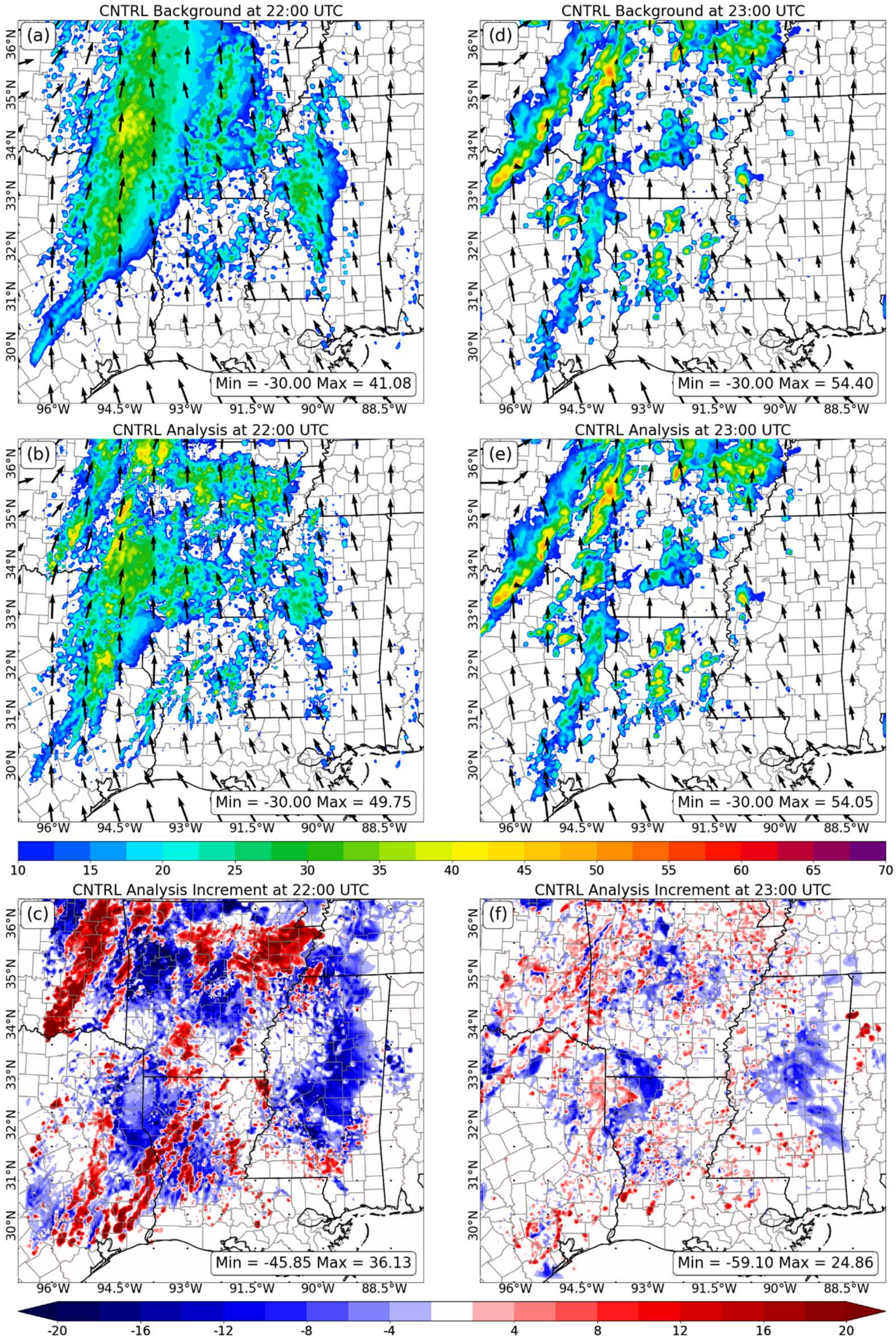

Figure 3.2: Composite reflectivity for the CNTRL experiment. (a) and (b) are the backgrounds for the 2200 UTC and 2300 UTC DA cycles respectively, (b) and (e) are the final analyses for the 2200 UTC and 2300 UTC cycles respectively, and (c) and (f) are the corresponding analysis increments.

Similar to Figure 3.1, Figure 3.3 demonstrates successful assimilation of WSR-88D V_r data on the 2500 m grid domain. As in WSR-88D Z DA, the decrease in RMSI after the DA step in each EnKF DA cycle demonstrates the nudging of the analysis toward the observation. The bias is always positive and relatively small, with values between ~0.08 and ~0.3 m s^{-1}. Variations in RMSI, ensemble spread, and bias do not have a noticeable trend. The average ensemble spread always falls below the assumed 3 m s^{-1} V_r OSED, except for the background ensemble spread for the first cycle. CR values stay between 1.2 and 1.5 throughout the DA period, indicating relatively well-dispersed V_r in the ensemble.

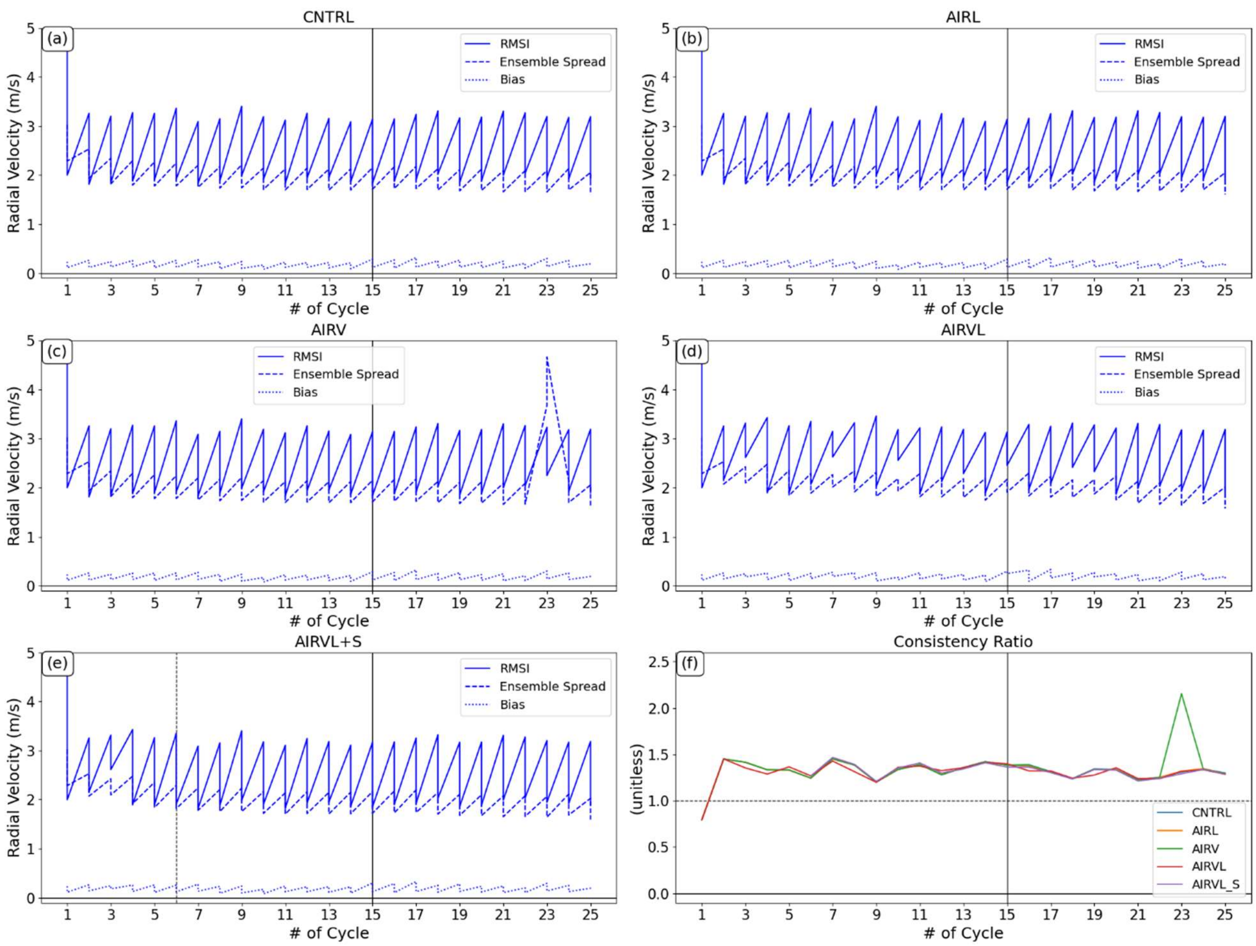

Figure 3.3: As in Figure 3.1, but for WSR-88D V_r data.

A sawtooth diagram for the CRL q_v DA on the 2500 m grid is shown in Figure 3.4. The variation in RMSI between backgrounds and analyses is not as consistent as in the previous two sawtooth diagrams (Figure 3.1 and Figure 3.3). This is likely due to the spatial differences between legs of the P3 flight path in different cycles. The variation in RMSI becomes more consistent, and the graph resembles a more traditional sawtooth diagram, once the magnitude of the bias exceeds 0.5 g kg^{-1} (cycle 8, 2235 UTC). This implies that the innovations at earlier cycles could be too small to strongly influence the analyses. Curiously, while the ensemble spread does decrease after DA for all cycles, the change is not as large as would be expected. This is also evident in the consistency ratio, whose values fluctuate greatly between DA cycles and are generally much greater than 1, indicating over-dispersion. As mentioned in section 2.2, the assumed OSED used for CRL q_v is relatively small in comparison to the errors that should be inherent in the CRL q_v data. It is speculated that the reason for the relatively small impact of DA on the ensemble spread is due to the RTPS inflation, whose α is somewhat large (0.95). A comparison of backgrounds and analyses, by way of the analysis increment (figure not included), supports the results of the RMSI, confirming that the influence of the CRL q_v DA is non-zero and does pull model q_v toward the observation. In section 3.1.2, the influence of CRL q_v DA will be further examined, with an emphasis on its influence on BL conditions in the inflow region of the storm on the 500 m grid.

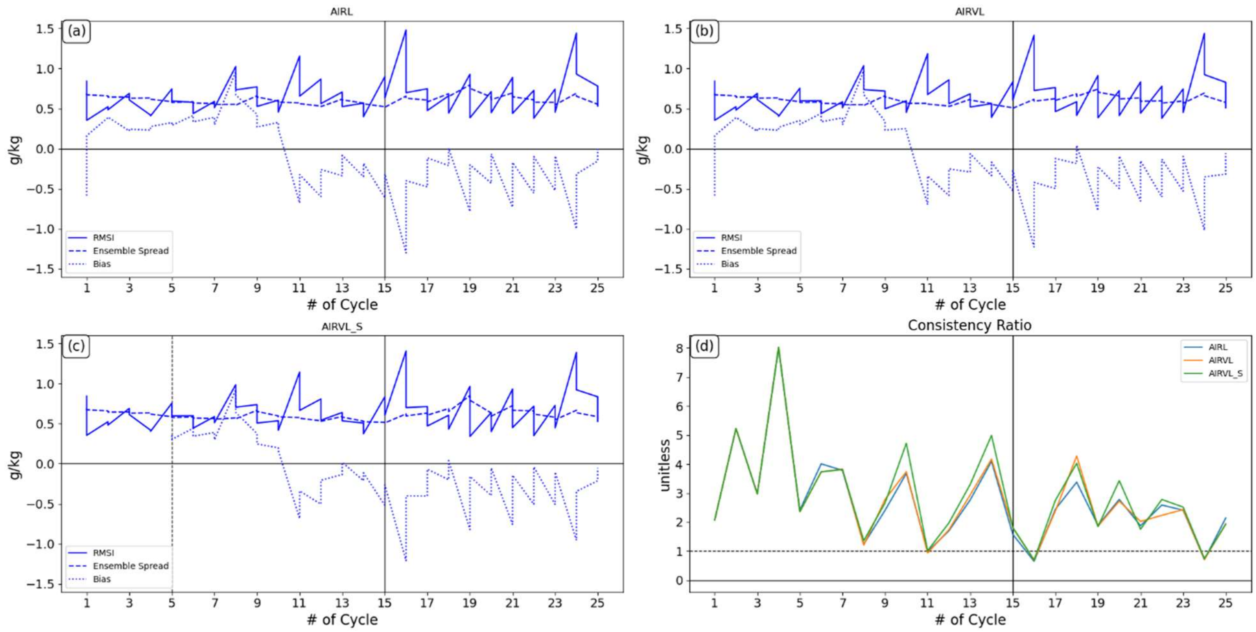

Figure 3.4: RMSI (solid blue), average ensemble spread (dashed blue), and bias (dotted blue) for formatted CRL q_v profile data on the 2500 m grid for the (a) AIRL, (b) AIRVL, and (c) AIRVL+S experiments. The dashed black line marks the first DA cycle for which a special sounding was assimilated. The solid black lines indicate the first cycle for which TDR data is assimilated on the 500 m grid. (d) The consistency ratio for AIRL (blue), AIRVL (orange), and AIRVL+S (green) experiments. A horizontal dashed black line is provided at CR=1, to help in diagnosing over- or under-dispersion.

After completing preliminary versions of the CNTRL, AIRL, AIRV, and AIRVL experiments, including their associated deterministic forecasts, a quick decrease in the skill of predicted reflectivity was found in the AIRV and AIRVL experiments (see section 3.2.1). In an investigation of the Monroe supercell's inflow environment, a "warm-nose" was identified at the 700 mb pressure level in AIRV and AIRVL ensemble mean analyses. This warm nose resulted in lower lapse rates and decreased buoyancy at and below the 700 mb level. The underperformance of AIRV and AIRVL forecasts was initially hypothesized to be linked to poor environment conditions in their analyses and, by extension, the presence of the 700 mb warm nose. As detailed in section 2.3, two VSE18 special soundings fall within the DA window. The soundings were launched from Minden, LA and Monroe, LA at 2225 UTC and 2230 UTC respectively. The

700 mb warm nose is absent from the real environment revealed by these soundings (Monroe sounding shown by way of example in Figure 3.5). However, temperature and moisture profiles retrieved from AIRVL analyses at these times and locations do show the presence of the 700 mb warm nose (Figure 3.6). Given the presence of the warm nose in AIRV and AIRVL analyses, a decision was made to run an additional experiment, AIRVL+S, which attempted to remove the 700 mb warm nose from the Monroe supercell's environment by assimilating the Minden and Monroe special soundings. The results, displayed in Figure 3.7, show successful removal of the 700 mb warm nose from the analyses by the special sounding DA. In addition to its removal at special sounding locations, the warm nose is also removed in an area around the special sounding locations equal to about half of the special sounding DA localization radius (75 km, see Figure 3.8). Storm relative helicity (SRH) is also increased across a similar area (Figure 3.9). DA of both the Minden and Monroe special soundings slightly decreases the surface temperature at sounding locations in the analysis, which causes a slight decrease in the convective available potential energy (CAPE). The impact of special sounding DA on the analyses of later cycles is discussed in subsequent sections.

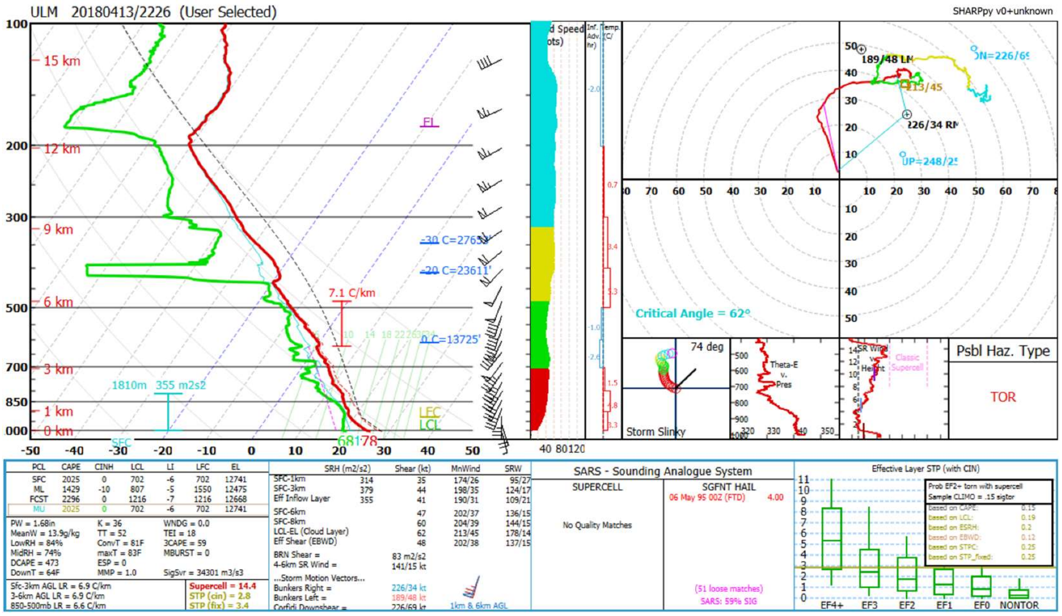

Figure 3.5: Skew-T diagram for the observed special sounding launched from Monroe, LA at 2226 UTC on 13 April 2018. Created using SHARpy.

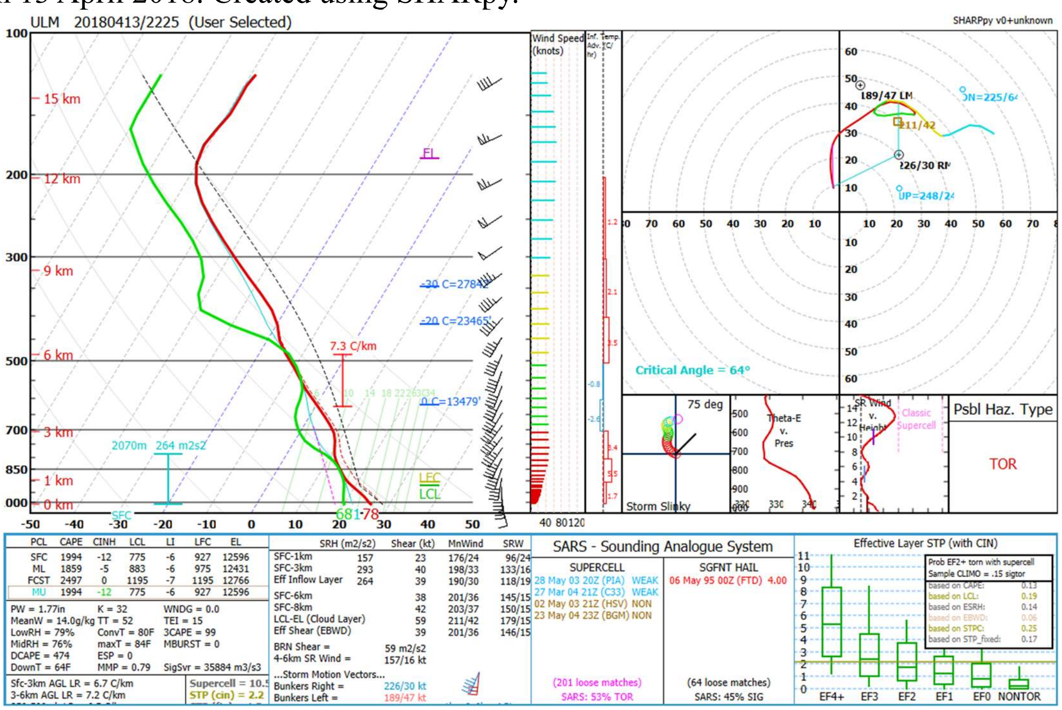

Figure 3.6: Skew-T diagram of temperature and moisture profiles from the cycle 6 (2225 UTC) AIRVL+S DA ensemble mean background interpolated to the 2226 UTC Monroe, LA special sounding launch location. Created using SHARpy.

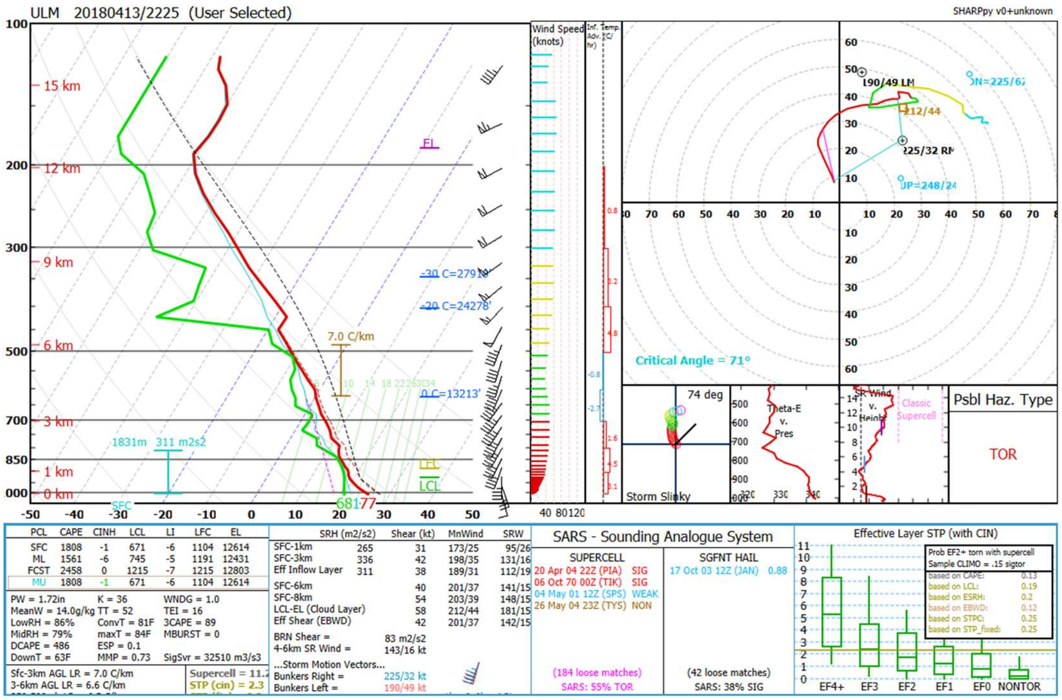

Figure 3.7: As in Figure 3.6, but for the cycle 6 (2225 UTC) AIRVL+S DA ensemble mean analysis.

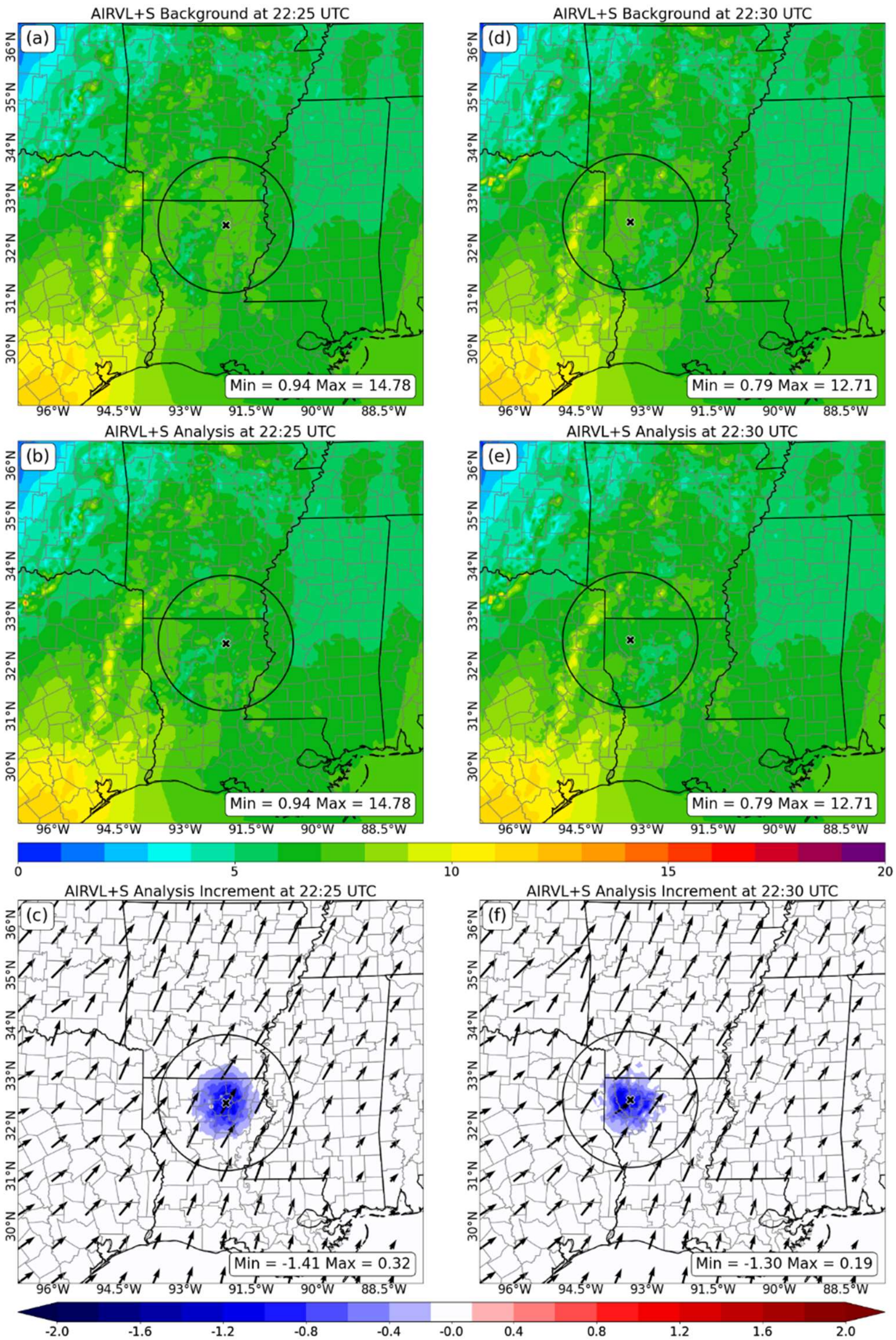

Figure 3.8: The 700 mb temperature (in °C) for the AIRVL+S experiment. (a) and (b) are the backgrounds for the 2225 UTC and 2230 UTC DA cycles respectively, (b) and (e) are the analyses for the 2225 UTC and 2230 UTC cycles respectively, and (c) and (f) are the corresponding analysis increments overlayed with 700 mb wind vectors. The black Xs indicate special sounding observation locations. The black circles indicate the extent of the localization radius used in special sounding DA.

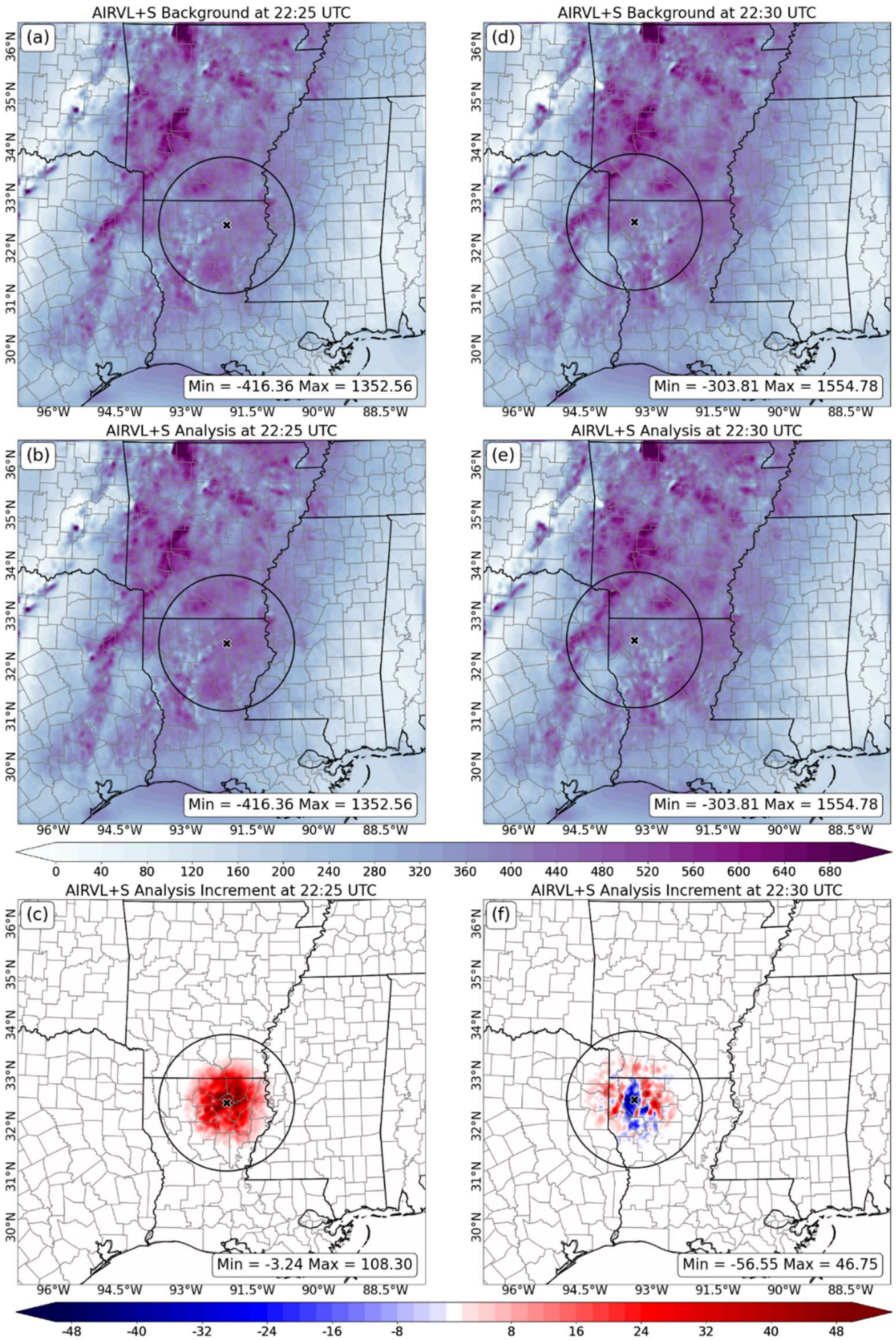

Figure 3.9: The 700 mb storm relative helicity (in m2 s-2) for the AIRVL+S experiment. (a) and (b) are the backgrounds for the 2225 UTC and 2230 UTC DA cycles respectively, (b) and (e) are the analyses for the 2225 UTC and 2230 UTC cycles respectively, and (c) and (f) are the corresponding analysis increments.

3.1.2 Comparison of Analyses on 500 m Grid

As was done for the 2500 m grid, innovation statistics were also computed on the 500 m grid for radar DA and CRL q_v DA (not shown). Generally, their values are similar to and consistent with those calculated on the 2500 m grid. This is expected, since feedback between the 2500 m outermost grid and the 500 m nested grid is two-way during the forecast step. This essentially leads to the replacement of a portion of the 2500 m outermost grid by the 500 m nested grid via interpolation within the 500 m grid's domain at the end of the forecast step. CR values for WSR-88D Z data on the 500 m grid range from ~0.65 to ~0.4, suggesting under-dispersion. CR values for WSR-88D V_r data on the 500 m grid are larger than 2500 m grid CR values, regularly surpassing 2. The increase in V_r CR values occurs for all experiments, implying that TDR/ KULM DA is not the cause. Within the 500 m grid domain, there are fewer radars and therefore fewer points considered in observation space statistical calculations, which likely causes this increase in CR. Innovation statistics were also calculated for CRL q_v DA on the 500 m grid and are virtually identical to those values calculated for the 2500 m grid.

Successful assimilation of TDR and KULM data on the 500 m nested grid is revealed via observation-space statistics in Figure 3.10. RMSI, spread, and bias decrease after the DA step of each DA cycle, indicating successful fitting of the analysis to the observation. The bias for KULM is generally negative, while the bias for TFOR and TAFT are generally positive. This suggests that V_r values derived from model backgrounds and analyses are smaller than observed KULM V_r values but are larger than observed TDR V_r values. CR values for the TFOR and TAFT V_r are near or below 1, indicating a well-dispersed ensemble relative to TDR V_r (Figure 3.11). The decrease in TDR CR between cycles 18 (2325 UTC) and 23 (2350 UTC) appears to be the result of increased RMSI. This increase in TDR RMSI is likely due to the spatial errors in the location of the low-level tornadic like vortex (TLV) that arise during the forecast step of each cycle. CR values for KULM V_r are above 1.5, sometimes surpassing 2, indicating an over-dispersed ensemble relative to KULM V_r (Figure 3.11).

A review of the ensemble mean analyses produced by TDR DA reals large values of downdraft in the upper levels of the Monroe supercell, at or above 8 km AGL (Figure 3.12 and Figure 3.13). The magnitude of the downdraft for some cycles exceeds 30 m s^{-1}, which is abnormally large. TAFT (Figure 3.12a) and TFOR (Figure 3.12d) observations show areas of strongly negative V_r values at high altitudes collocated with these abnormal downdraft values. As shown in Figure 3.12h and Figure 3.13b, areas of large, positive innovations, calculated using TAFT and TFOR observations, are collocated with high magnitude downdrafts in the analysis. This proves that TDR DA is the cause of these abnormal downdraft values in the analyses. However, as shown in Figure 3.12j, these values seldom persist through to the end of the forecast step and are generally absent from the background of the next DA cycle. Since these values are likely unphysical, the model could be resolving inconsistencies in model dynamics using the creation and propagation of gravity waves. The unphysically large downdraft values in the ensemble mean analyses could potentially affect their associated deterministic forecasts. However, their true effect on the forecasts was not verified in this study.

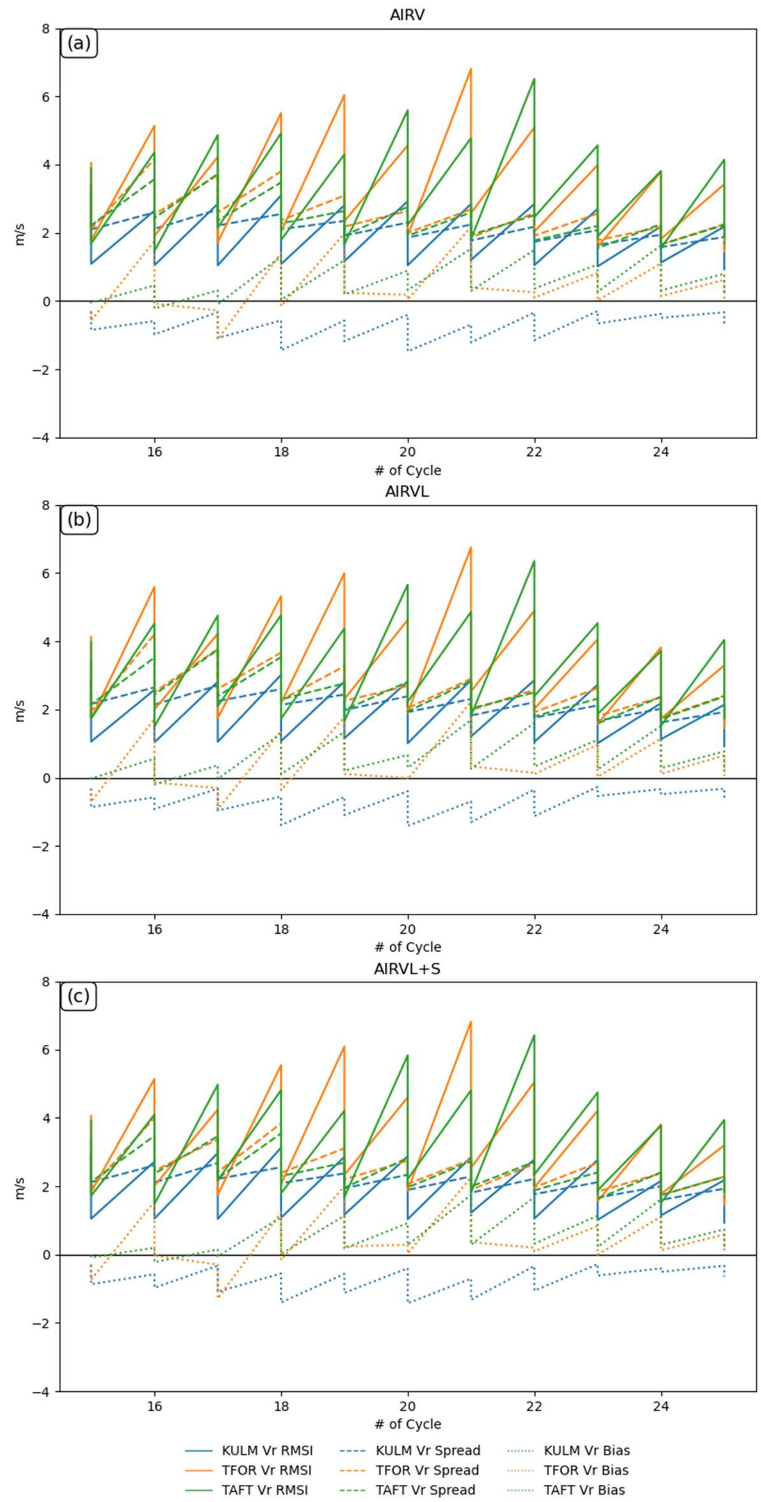

Figure 3.10: RMSI (solid lines), average ensemble spread (dashed lines), and bias (dotted lines) for KULM (blue), TFOR (orange) and TAFT (green) V_r data on the first nested, 500 m grid for the (a) AIRV, (b) AIRVL, and (c) AIRVL+S experiments.

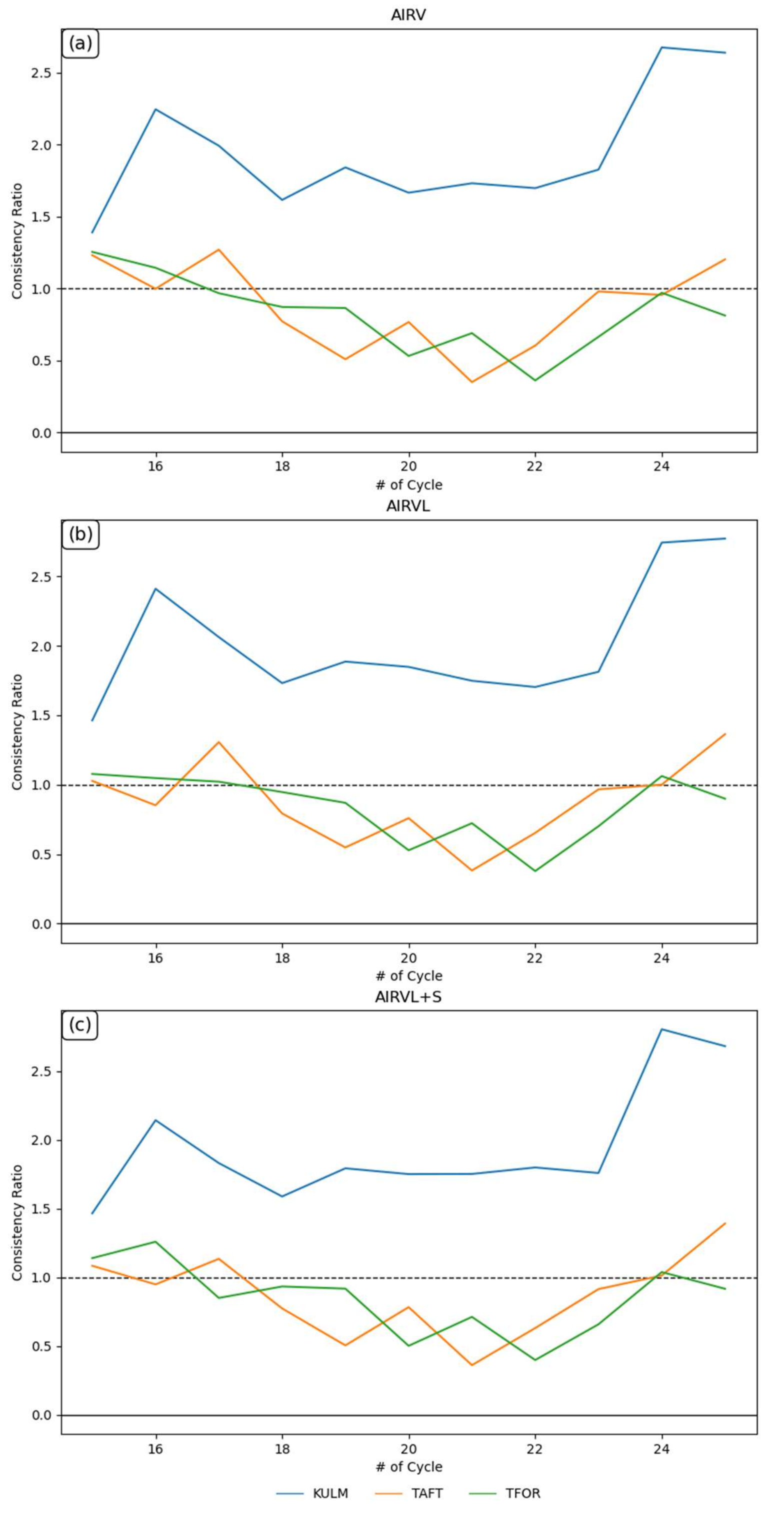

Figure 3.11: As in Figure 3.10, but for a consistency ratio (solid lines). A horizontal dashed black line is provided for CR=1, to help in diagnosing over- or under-dispersion.

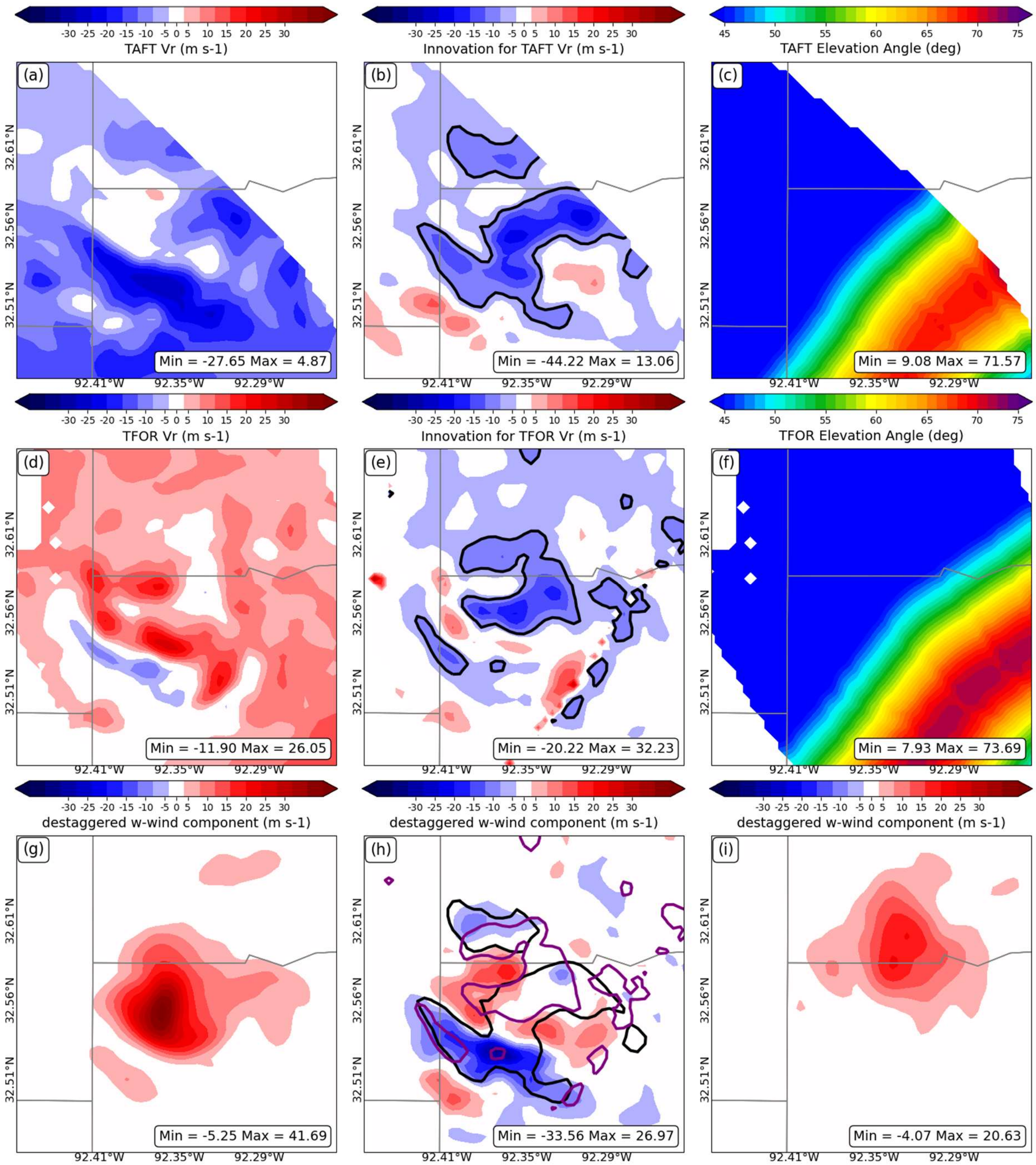

Figure 3.12: (a) TAFT V_r observation at 10 km AGL for 2325 UTC 13 April 2018, (b) TAFT V_r ensemble mean innovation for the AIRV experiment at 10 km AGL for cycle 18 (2325 UTC), (d) the elevation angle for TAFT at 10 km AGL for 2325 UTC. (d)-(f) Same as (a)-(b) but for TFOR. (g) Ensemble mean background 10 km vertical velocity on mass grid points for the cycle 18 (2325 UTC), (g) ensemble mean analysis 10 km vertical velocity on mass grid points for cycle 18 (2325 UTC) with solid contours marking locations where TAFT (black) and TFOR (purple) innovations are less than or equal to -8 m/s. (i) Ensemble mean background 10 km vertical velocity on mass grid points for cycle 19 (2330 UTC).

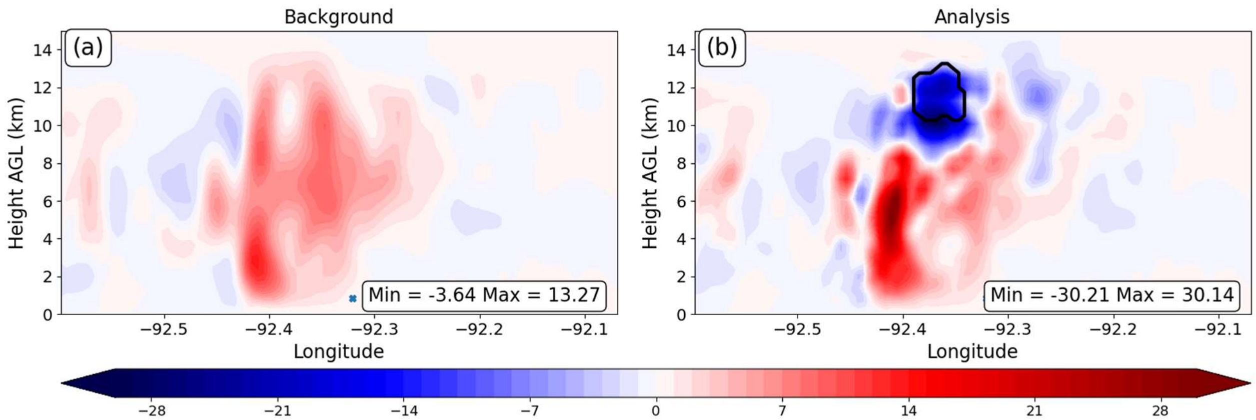

Figure 3.13: Ensemble mean (a) background and (b) analysis vertical velocity on mass grid points for cycle 18 (2325 UTC) of the AIRV experiment. The black contour in (b) indicates where both the TFOR and TAFT innovations are less than -10 m/s.

Figure 3.14, Figure 3.15, Figure 3.16, and Figure 3.17 depict the low-level structure of the Monroe supercell in the ensemble mean analyses of cycles 18 (2325 UTC), 20 (2335 UTC), 22 (2345 UTC), and 23 (2350 UTC) respectively. Figure 3.18, Figure 3.19, Figure 3.20, and Figure 3.21 compare the three-dimensional vertical vorticity and vertical velocity structures present in the ensemble mean analyses of the CNTRL and AIRVL experiments for the same times respectively. Results from cycles 20 and 22 are shown here because they display reanalysis conditions at times when a tornado was observed on the ground (the Calhoun the Downsville tornadoes respectively). Cycles 18 and 23 are also shown to further demonstrate the spectrum of results provided by the experiments. Additionally, the time-height plot of maximum vertical vorticity for all experiments is shown in Figure 3.22.

The low-level (<1 km) TLV is present and clearly visible in the experiments assimilating TDR and KULM V_r data (AIRV, AIRVL, and AIRVL+S) but is completely absent from the other experiments. In the CNTRL and AIRL experiments, vertical vorticity values of at least 15×10^{-3} s^{-1} sometimes reach into the mid-levels, as low as 2 km for cycle 22 (2345 UTC) (Figure 3.22). However, in the AIRV, AIRVL, and AIRVL+S analyses, higher vorticity values extend through the mid-levels to less than 50 m above the surface, with near surface values exceeding 70×10^{-3} s^{-1} in some cases (Figures 3.14 through 3.22). A column of relatively high vertical vorticity values extends upward from the surface in AIRV, AIRVL, and AIRVL+S experiments, with values greater than 30×10^{-3} s^{-1} reaching heights greater than or equal to 4 km AGL, and values greater than 15×10^{-3} s^{-1} reaching the top of the supercell. As shown in Figure 3.22, large vorticity values in these experiments first appear near the surface and then build upward very rapidly, peaking in magnitude at 2335 UTC, coinciding with the formation of the Calhoun tornado. This agrees with tornado simulations conducted in other studies (Rotunno and Bluestein 2024).

The magnitude of both updrafts and downdrafts is greatest in the AIRV, AIRVL, and AIRVL+S experiments. Updraft values exceeding 10 m s^{-1}, and sometimes surpassing 15 m s^{-1}, are present 1 km AGL in these experiments. In the CNTRL and AIRL experiments, strong updrafts are present but are not found as close to the surface.

In addition to improved wind fields, the simulated 10 cm reflectivity structure at 1 km AGL in the AIRV, AIRVL, and AIRVL+S experiments is more representative of a classic tornado producing supercell, featuring a more distinct hook echo, than in the other experiments.

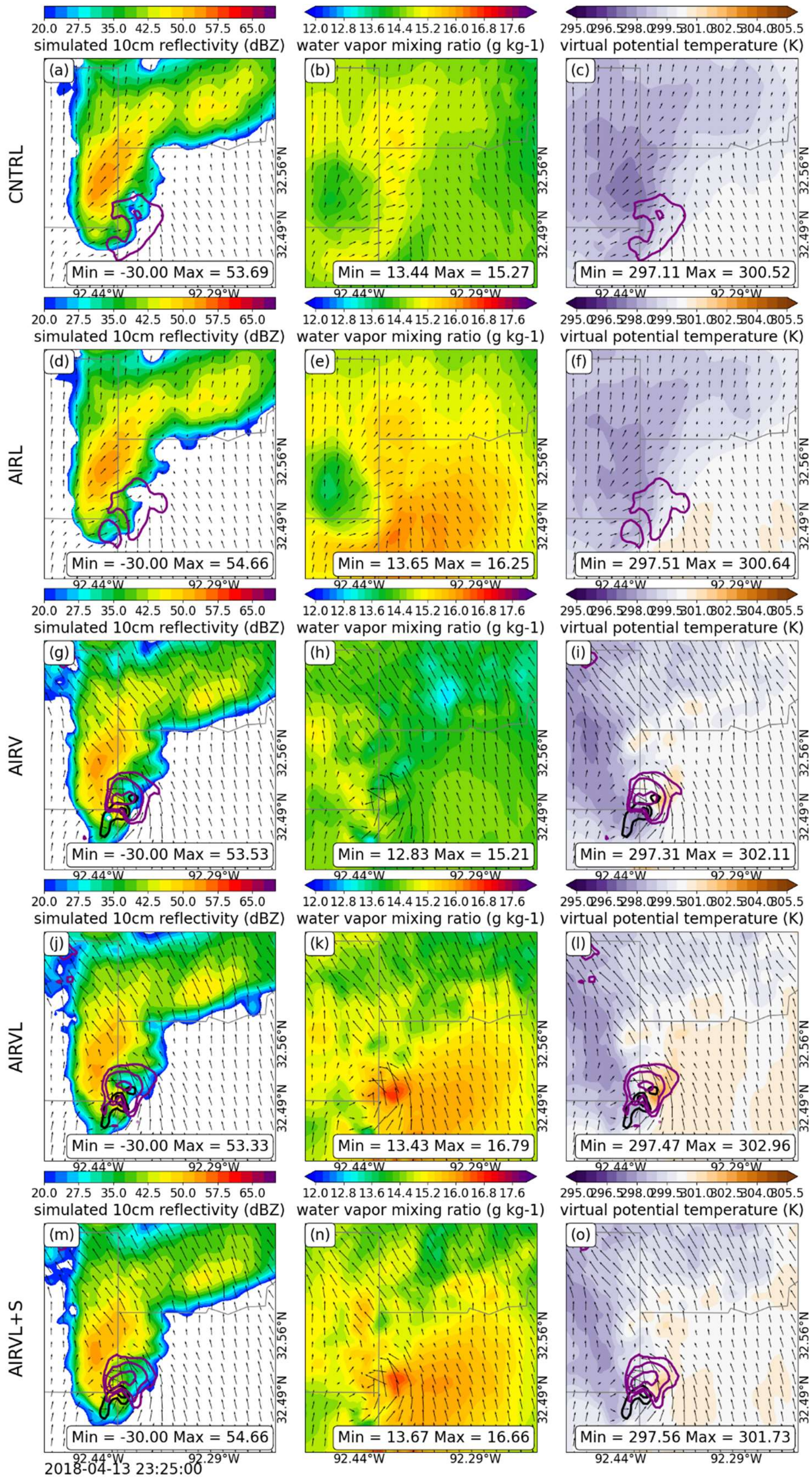

simulated 10cm reflectivity (dBZ)
water vapor mixing ratio (g kg-1)
virtual potential temperature (K)
20.0 27.5 35.0 42.5 50.0 57.5 65.0
12.0 12.8 13.6 14.4 15.2 16.0 16.8 17.6
295.0 296.5 298.0 299.5 301.0 302.5 304.0 305.5
CNTRL
AIRL
AIRV
AIRVL
AIRVL+S
(a) Min = -30.00 Max = 53.69
(b) Min = 13.44 Max = 15.27
(c) Min = 297.11 Max = 300.52
(d) Min = -30.00 Max = 54.66
(e) Min = 13.65 Max = 16.25
(f) Min = 297.51 Max = 300.64
(g) Min = -30.00 Max = 53.53
(h) Min = 12.83 Max = 15.21
(i) Min = 297.31 Max = 302.11
(j) Min = -30.00 Max = 53.33
(k) Min = 13.43 Max = 16.79
(l) Min = 297.47 Max = 302.96
(m) Min = -30.00 Max = 54.66
(n) Min = 13.67 Max = 16.66
(o) Min = 297.56 Max = 301.73
92.44°W
92.29°W
32.56°N
32.49°N
2018-04-13 23:25:00

Figure 3.14: Cycle 18 (2325 UTC) ensemble mean analyses for the (a)-(e) CNTRL, (d)-(f) AIRL, (g)-(i) AIRV, (j)-(l) AIRVL, and (m)-(o) AIRVL+S experiments. The first column (a, d, g, j, m) displays 1 km AGL simulated 10 cm reflectivity, the second row (b, e, h, k, n) displays 50 m AGL q_v, and the third row (c, f, i, l,o) displays virtual potential temperature at 50 m AGL. Solid black contours denote vertical vorticity at 50 m AGL of 15, 30, and 60 10^{-3} s^{-1}. Solid purple contours denote updraft strength at 1 km AGL of 5, 10, and 15 m s^{-1}.

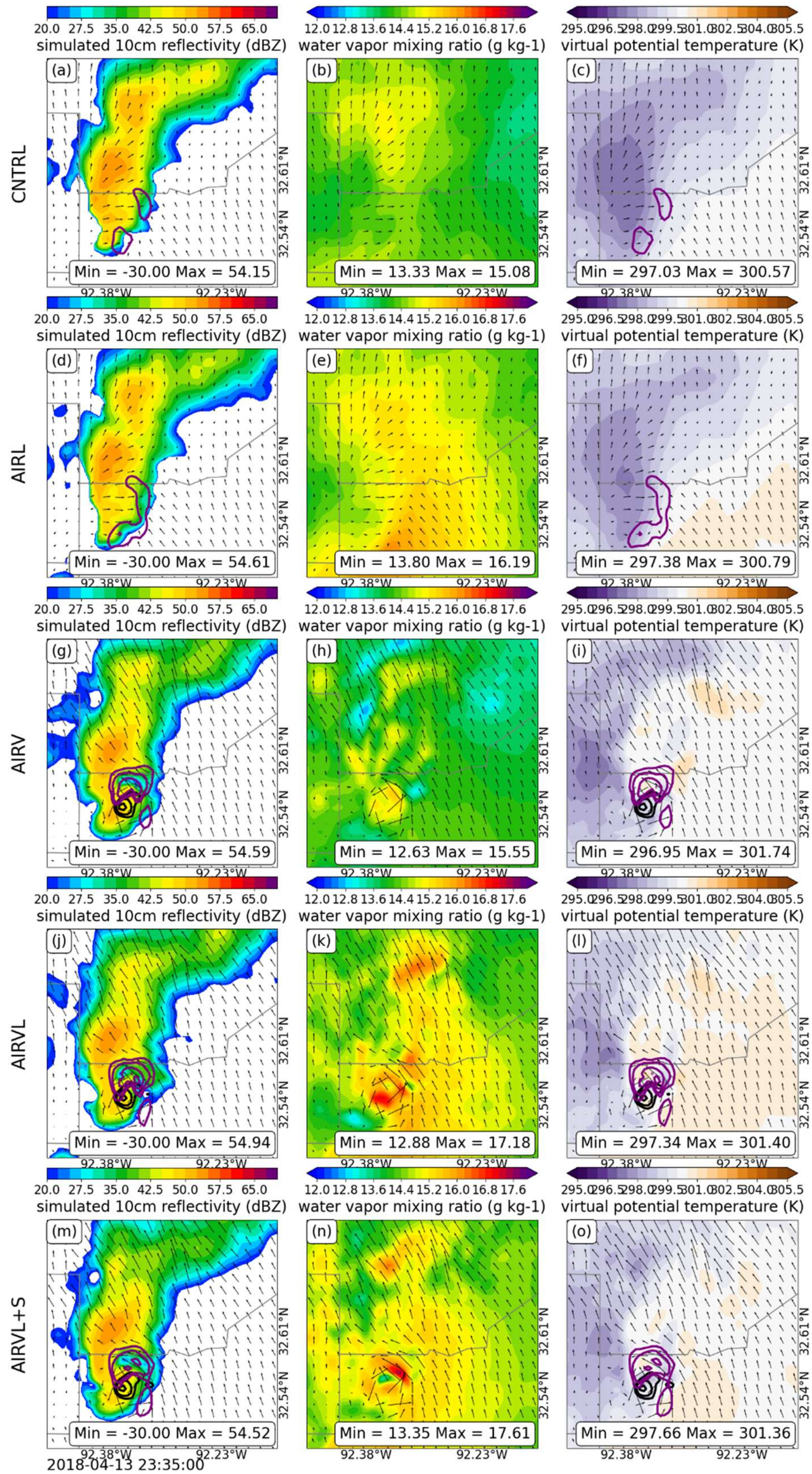

Figure 3.15: As in Figure 3.15, but for ensemble mean analyses from cycle 20 (2335 UTC).

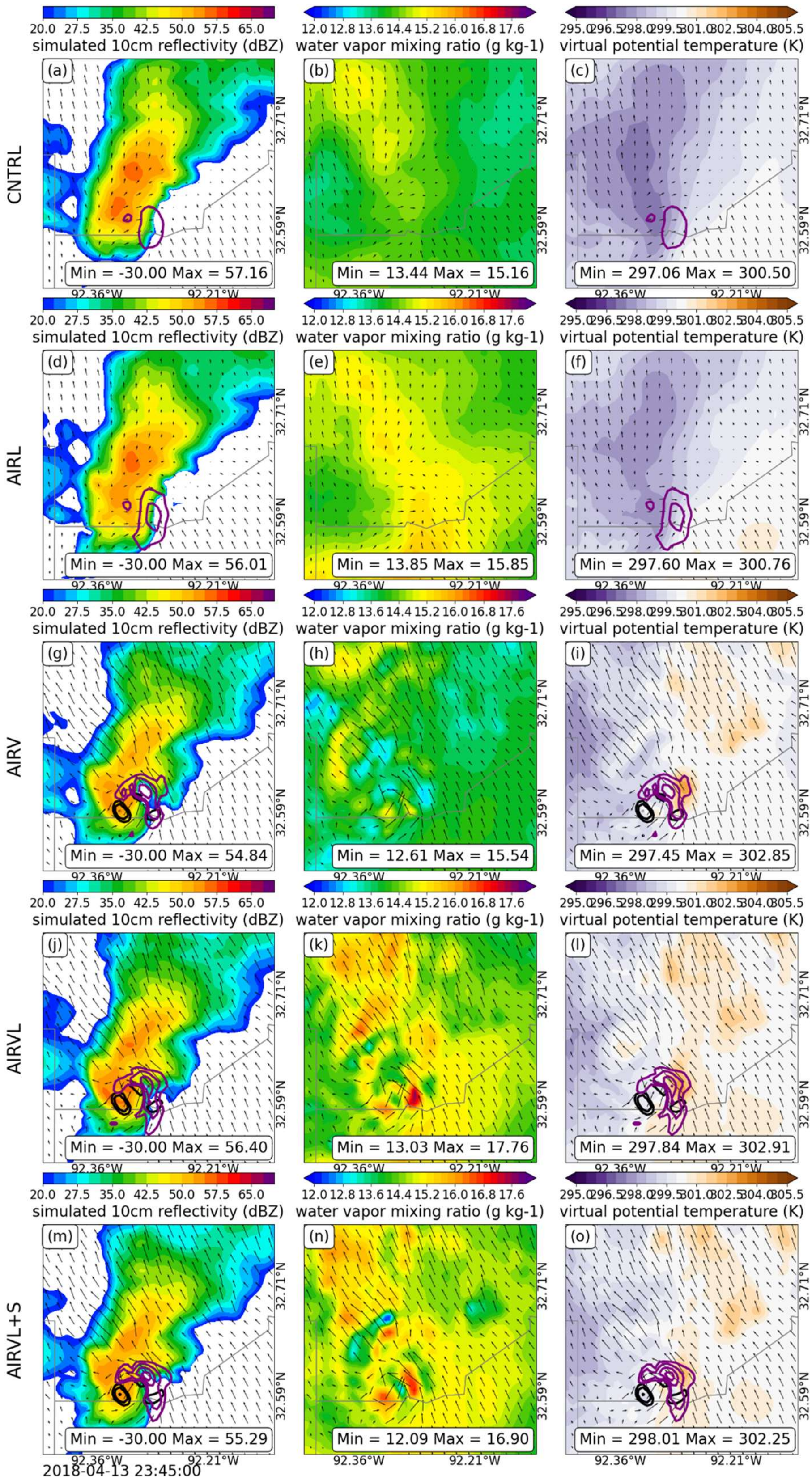

Figure 3.16: As in Figure 3.15, but for ensemble mean analyses from cycle 22 (2345 UTC).

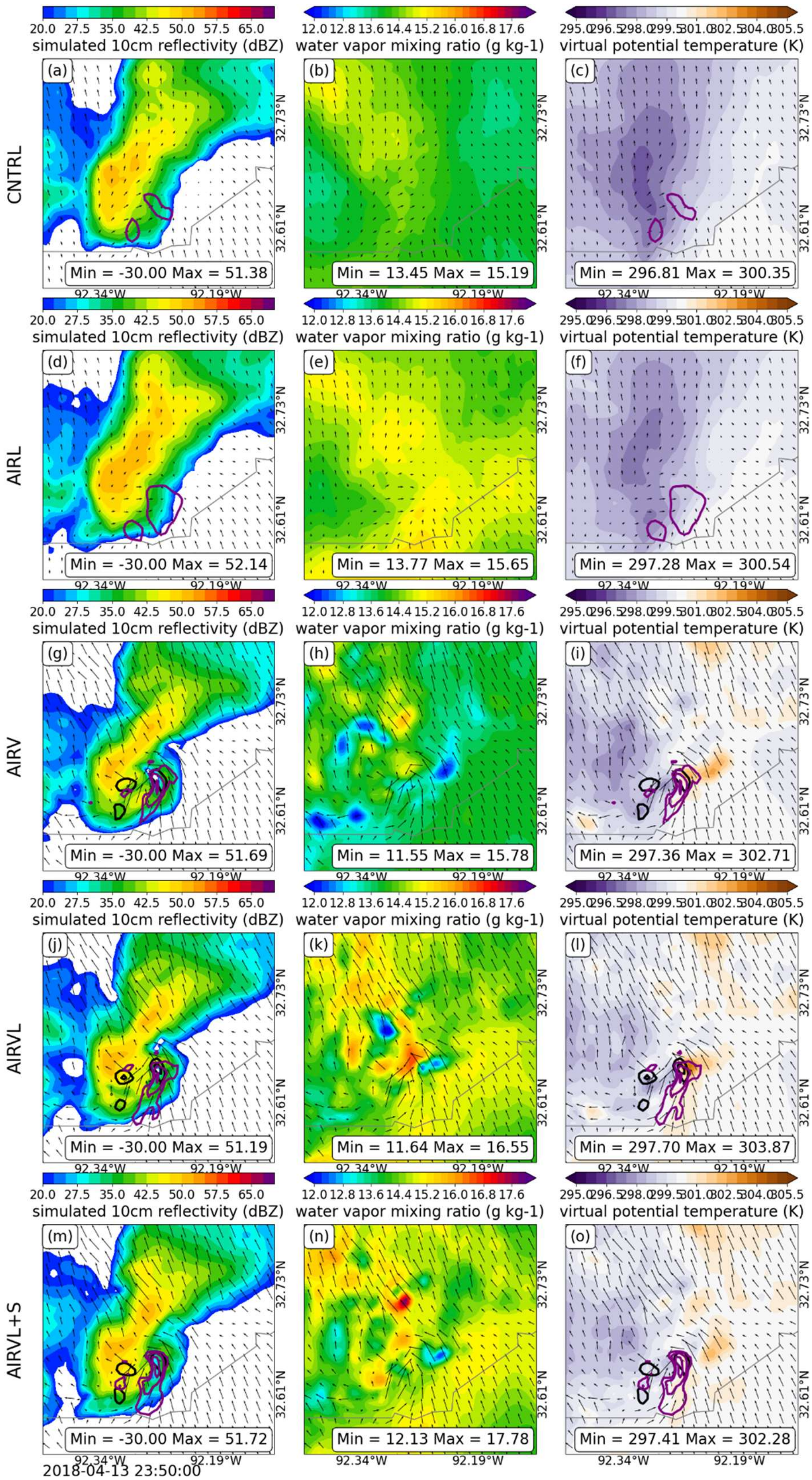

Figure 3.17: As in Figure 3.15, but for ensemble mean analyses from cycle 23 (2350 UTC).

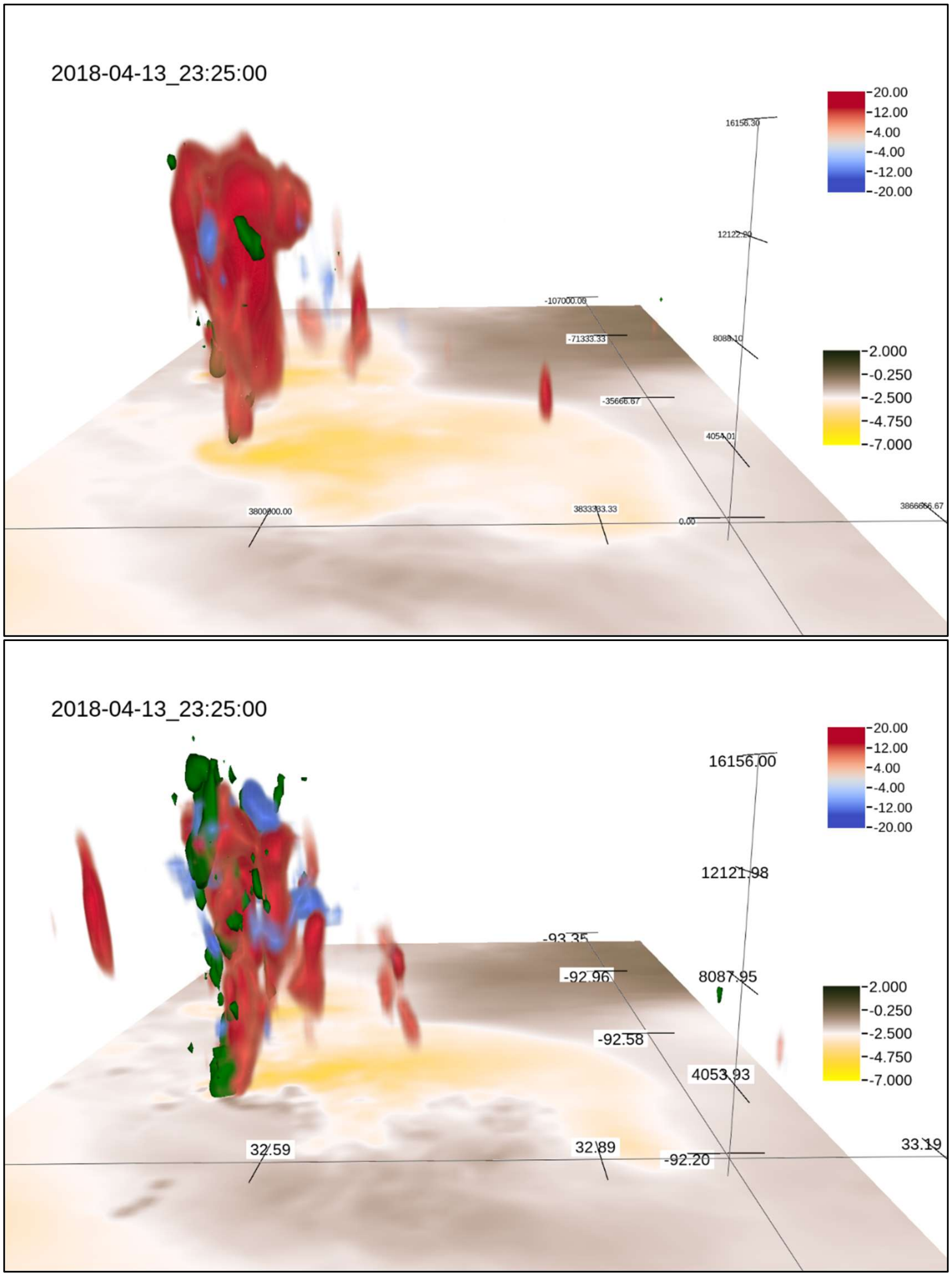

Figure 3.18: A three-dimensional rendering of the ensemble mean analyses for cycle 18 (2325 UTC) of the CNTRL (top) and AIRVL (bottom) experiments. Updraft and downdraft magnitude are represented by red and blue shading respectively. The potential temperature perturbation at the first model level above the ground is given by the yellow and black shaded surface. The green surface is an iso-surface of constant 15×10^{-3} s^{-1} vertical vorticity. Created using VAPOR (Li et al. 2019).

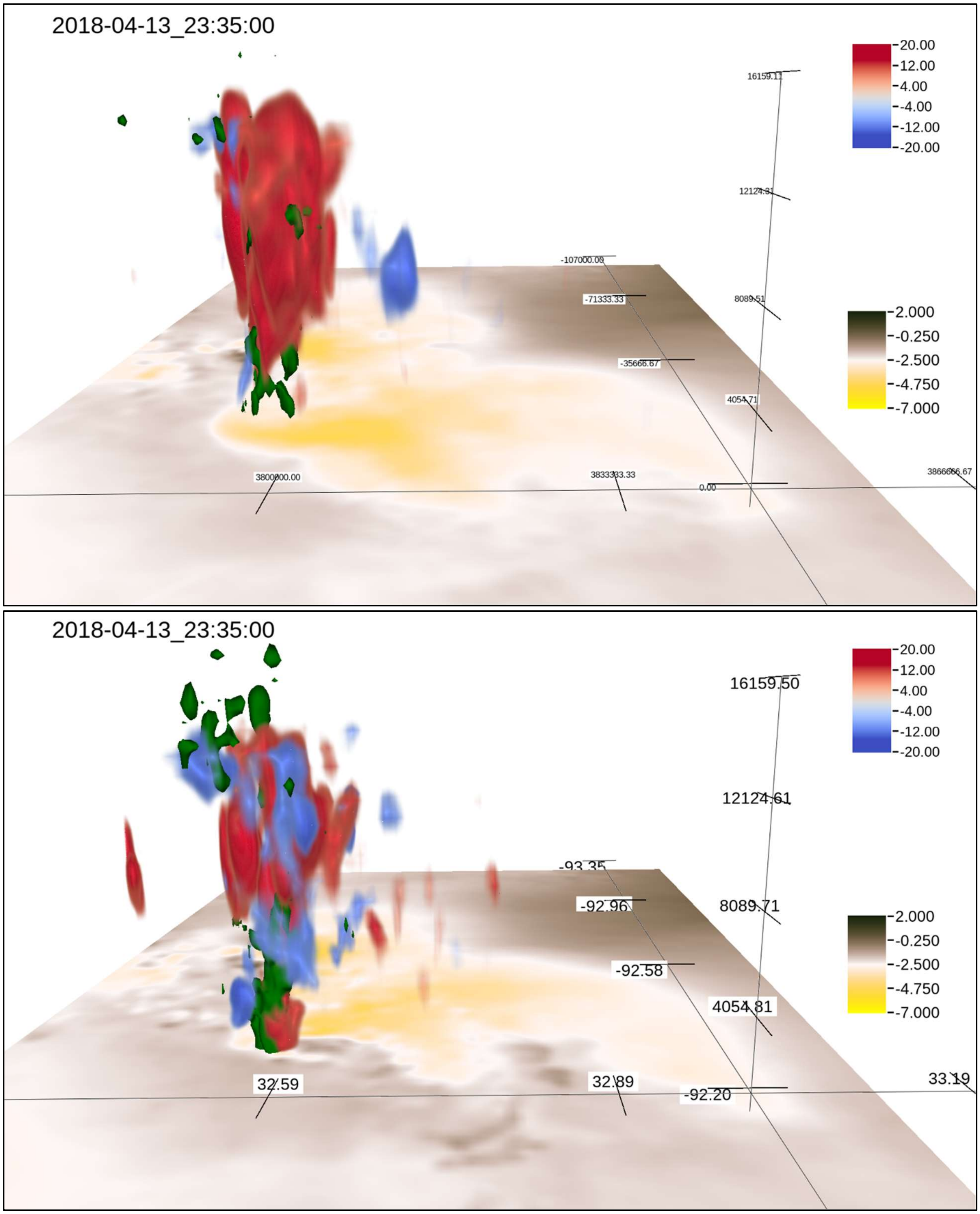

Figure 3.19: As in Figure 3.18, but for cycle 20 (2335 UTC).

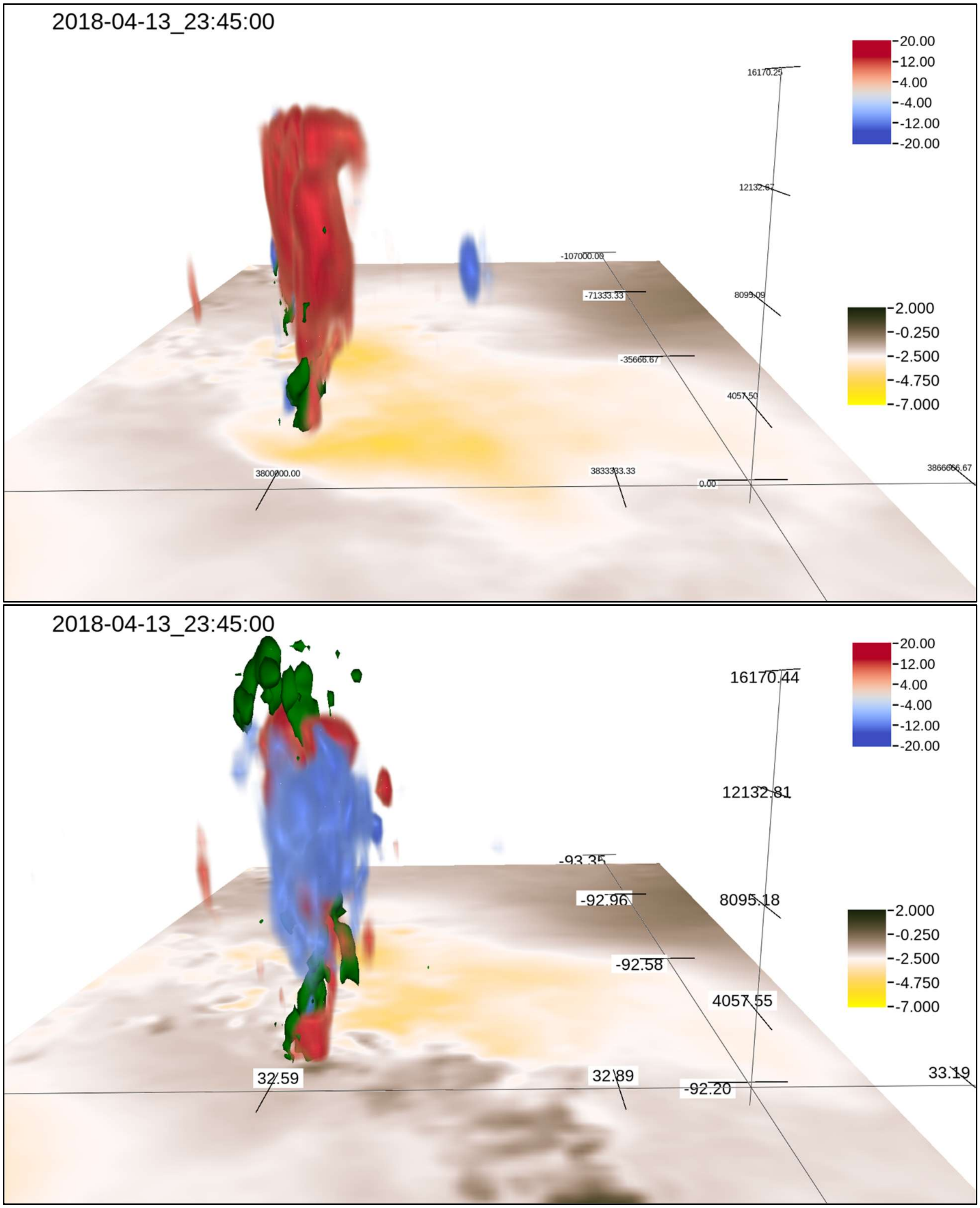

Figure 3.20: As in Figure 3.18, but for cycle 22 (2345 UTC).

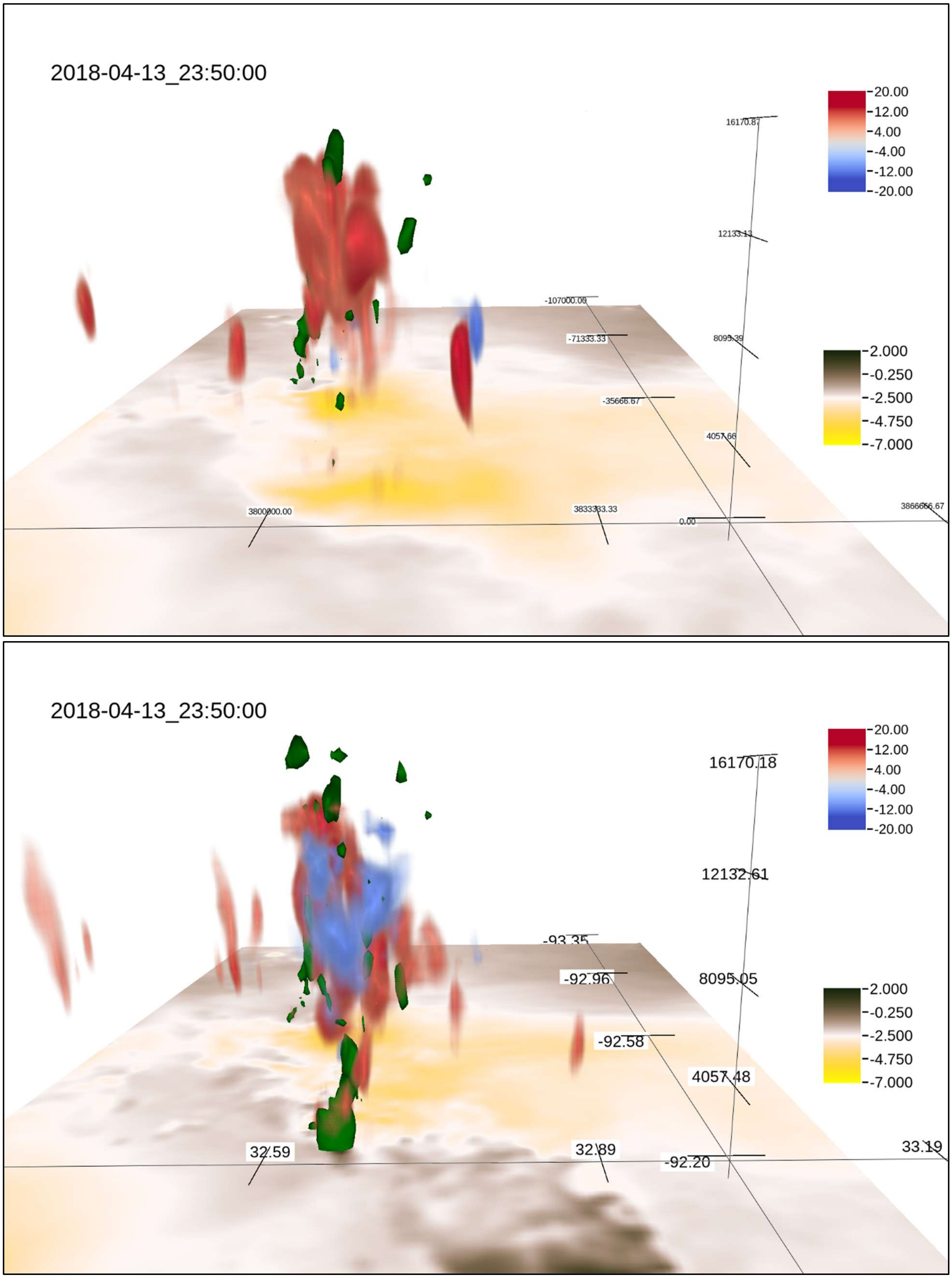

Figure 3.21: As in Figure 3.19, but for cycle 23 (2350 UTC).

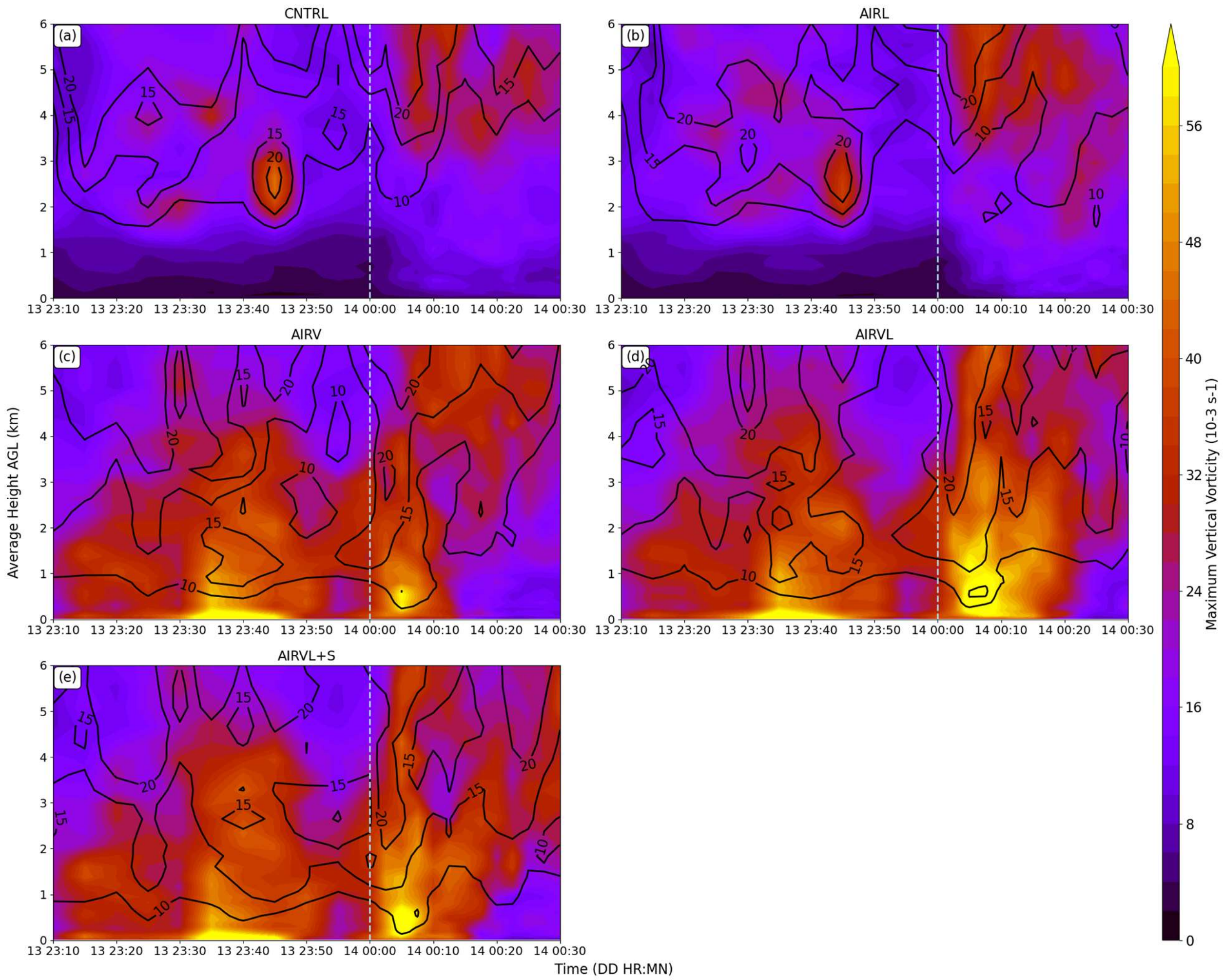

Figure 3.22: Time-height plot of horizontal maximum vertical vorticity (10^{-3} s^{-1}) (filled contours) for the ensemble mean analyses (before 0000 UTC, dash light blue line) and subsequent deterministic forecasts (after 0000 UTC, dash light blue line). Horizontal maximum updraft also shown for 10 ms^{-1}, 15 ms^{-1}, and 20 ms^{-1} thresholds (solid black contours). Results shown for (a) CNTRL, (b) AIRL, (c) AIRV, (d) AIRVL, and (e) AIRVL+S experiments. Maximums derived on 500 m grid using values within a 30 km by 30 km box centered on the Monroe supercell storm center.

As expected, the experiments assimilating CRL q_v data generally exhibit larger low-level ($<$ 500 m) q_v values in the inflow region of the supercell. In experiments that also assimilate TDR and KULM data, the region of enhanced q_v extends beyond the inflow region and wraps around the TLV. Although CRL temperature data are not directly assimilated, CRL q_v DA experiments generally have higher temperature values in the inflow region.

The differences between the AIRVL and AIRVL+S analyses of the Monroe supercell on the 500 m grid are less pronounced than might be expected, given the improvements made to environmental conditions by special sounding DA in earlier cycles. As shown in Figure 3.23, the 700 mb warm nose, which was removed near Monroe, LA and Minden, LA in the 2225 UTC and 2230 UTC AIRVL+S analyses respectively, reappears in the supercell environment at 2320 UTC. In the 2225 UTC and 2230 UTC AIRVL+S analyses, shown Figure 3.8c and Figure 3.8f, 700 mb flow is southwesterly, aligning with the southwesterly track of the Monroe supercell. Since the supercell is located near the southern boundary of the modified environment in the 2230 UTC DA analysis, it is suspected that the modified environment is advected northeastward, away from the Monroe supercell, before it can significantly influence the supercell's evolution. Consequently, the environment feeding the supercell in the AIRVL+S experiment does not differ significantly from the environment in the AIRVL experiment. Differences between the AIRVL and AIRVL+S analyses, in terms of low-level updraft intensity and low-level vertical vorticity, while perceptible, are also subtle and not always consistent. For example, the analyzed TLV is stronger in the AIRVL+S experiment than that in the AIRVL experiment for cycle 22 (2345 UTC, Figure 3.16) but is weaker for cycle 23 (2350 UTC, Figure 3.17). Similarly, the analyzed updraft intensity is weaker in the AIRVL+S experiment than in the AIRVL experiment for cycle 20 (2335 UTC, Figure 3.15) but is greater for cycle 23 (Figure 3.17).

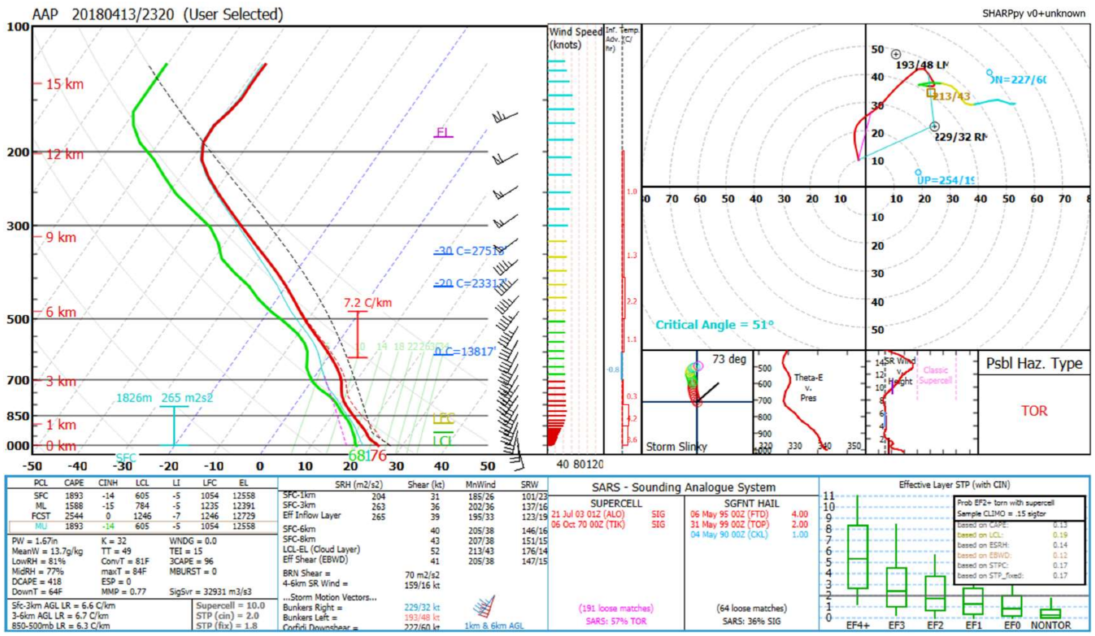

Figure 3.23: Skew-T diagram of temperature and moisture profiles from the cycle 17 (2320 UTC) AIRVL+S DA ensemble mean analysis approximately 30 km southeast of the Monroe supercell center.

Ultimately, the analyses produced by the AIRVL and AIRVL+S experiments are superior to those of other experiments, since they include stronger TLV signatures, more intense low- and mid-level updrafts, and improved BL conditions in the inflow region of the supercell. Improvements in TLVs, updraft magnitude, and supercell storm structure make AIRV analyses more appealing than the CNTRL and AIRL analyses. However, AIRL analyses may be more attractive than AIRV analyses if BL improvements in the inflow region are desired.

3.2 Impact of DA on Forecasts

3.2.1 Predicted Reflectivity and Mid-level Updrafts

As outlined in section 2.3, deterministic forecasts are initialized from the ensemble mean analysis of each DA cycle and experiment beginning with DA cycle 17 (2320 UTC). Predicted reflectivity is quantitatively evaluated using equitable threat score (ETS) and fractional skill score (FSS) statistical scores for composite reflectivity. Since feedback between WRF grids is two-way, 500 m grid values within the 100 m grid domain are averaged from the 100 m grid. Therefore, to speed up computation, 500 m values are used instead of 100 m grid values. Composite WSR-88D reflectivity interpolated to the 500 m grid is used as truth.

The ETS, also referred to as the Gilber Skill Score (Schaefer 1990), is given by the equation:

$$ETS = \frac{a - a_r}{a + b + c - a_r} \tag{3.6}$$

where a is the number points that reach the given threshold in both the observation and the forecast (hits), b is the number of the points that reach the threshold in forecast but not the observation (false alarms), c is the number of points that reach the threshold in the observation but not in the forecast (misses), and a_r is the estimated number of hits that occur randomly. a_r is given by the equation:

$$a_r = \frac{(a + b)(a + c)}{n} \tag{3.7}$$

where n is the total number of points. The inclusion of a_r in the calculation of ETS is what makes the score "more equitable" than the Critical Success Index. An ETS value of 0 indicates no skill and an ETS value of 1 indicates a perfect forecast.

Since ETS is a traditional, point-based verification metric, it evaluates forecasts at individual grid points without considering spatial relationships. This can be a major limitation when verifying high-resolutions forecasts, where small spatial displacements are penalized twice, leading to poor ETS scores despite being meteorologically useful. Neighborhood-based verification methods, such as the FSS, aim to address the limitations of ETS by relaxing the strict point-to-point comparison and allowing for some spatial flexibility. The FSS compares the fraction of observed and forecasted events within a given neighborhood (Roberts and Lean 2008). It is given by the equation

$$FSS = 1 - \frac{\sum_N \left(P_{fcst} - P_{obs}\right)^2}{\sum_N P_{fcst}^2 + \sum_N P_{obs}^2} \qquad (3.8)$$

where P_{fcst} and P_{obs} are the fraction of the forecast points and observed points, respectively, within a given neighborhood. FSS values range from 0 to 1, with 0 indicating no skill and 1 indicating a perfect forecast.

For most of the deterministic forecasts, specifically those initialized using analyses from cycles 18 through 23, the AIRL experiment has the higher ETS and FSS scores compared to other experiments. This is especially true at later forecast times, i.e. 15 to 20 minutes after initialization (Figure 3.24 and Figure 3.25). This trend is also visually observed in plotted reflectivity fields. As shown in Figure 3.26 and Figure 3.27, the storm in the AIRL forecast remains organized and retains supercellular characteristics, including hook echo structure, longer than the other experiments. As shown in Figure 3.28 and Figure 3.29, AIRL also maintains strong mid-level updrafts and an associate mesocyclone longer than forecasts from other experiments. Conversely, AIRV ETS and FSS scores are worse than all other experiments, including CNTRL, for most forecasts (cycles 17 through 23). This suggests that TDR and KULM DA degrades reflectivity forecasts. This is likewise confirmed qualitatively via plotted reflectivity fields. In the AIRV experiment, and to a lesser degree the AIRVL and AIRVL+S experiments, the forecasted supercell loses its supercellular characteristics and becomes disorganized quickly 15 to 20 minutes after initialization. As shown in Figure 3.28 and Figure 3.29, the mid-level updrafts also quickly weaken during this time frame.

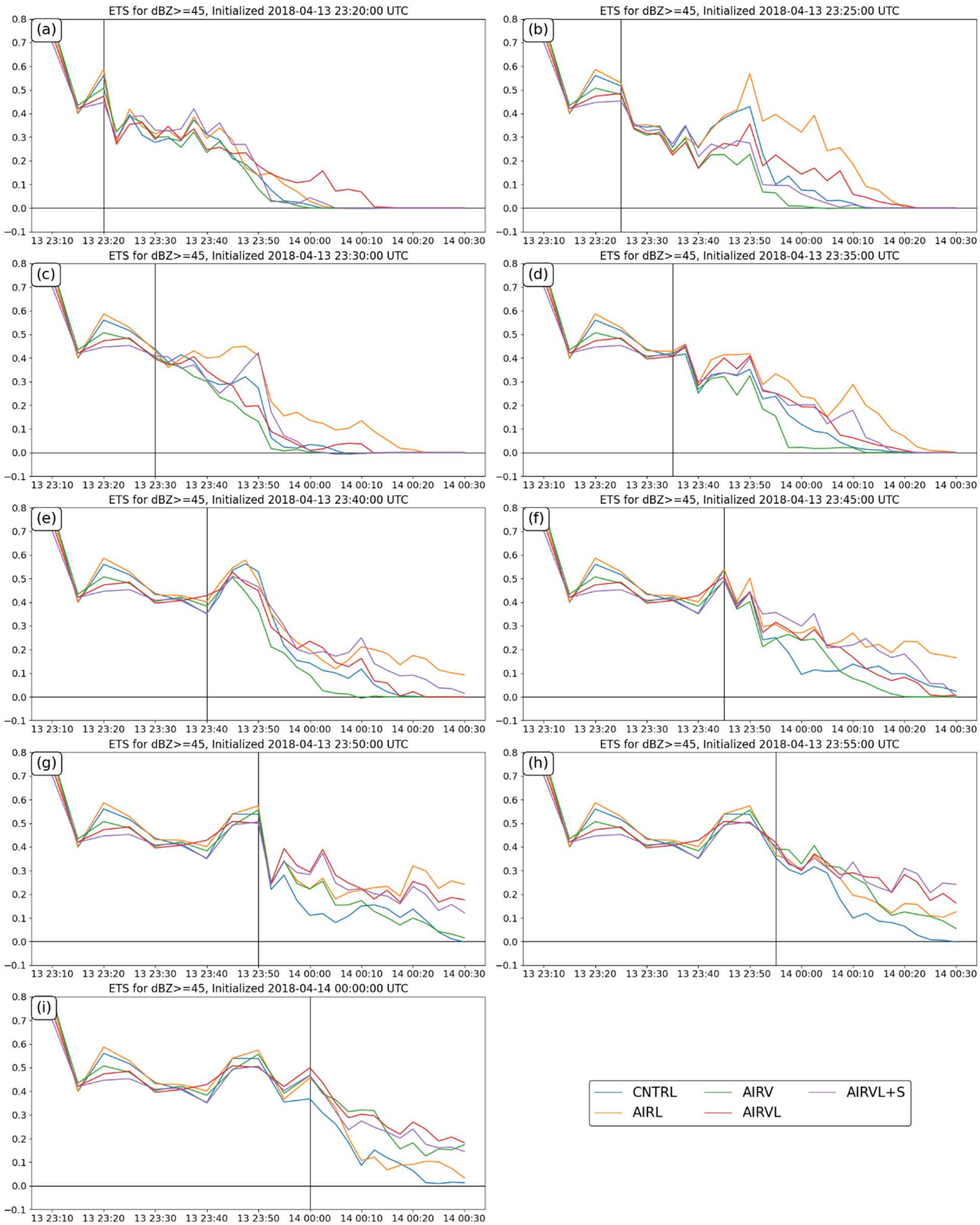

ETS for dBZ>=45, Initialized 2018-04-13 23:20:00 UTC
(a)
ETS for dBZ>=45, Initialized 2018-04-13 23:25:00 UTC
(b)
ETS for dBZ>=45, Initialized 2018-04-13 23:30:00 UTC
(c)
ETS for dBZ>=45, Initialized 2018-04-13 23:35:00 UTC
(d)
ETS for dBZ>=45, Initialized 2018-04-13 23:40:00 UTC
(e)
ETS for dBZ>=45, Initialized 2018-04-13 23:45:00 UTC
(f)
ETS for dBZ>=45, Initialized 2018-04-13 23:50:00 UTC
(g)
ETS for dBZ>=45, Initialized 2018-04-13 23:55:00 UTC
(h)
ETS for dBZ>=45, Initialized 2018-04-14 00:00:00 UTC
(i)
13 23:10
13 23:20
13 23:30
13 23:40
13 23:50
14 00:00
14 00:10
14 00:20
14 00:30
CNTRL
AIRL
AIRV
AIRVL
AIRVL+S

Figure 3.24: Equitable threat scores calculated for composite reflectivity using a threshold of 45 dBZ. Values are calculated for ensemble mean analyses (before solid black line) and deterministic forecasts (after solid black line) using values on the 500 m grid. Deterministic forecasts are initialized at (a) 2320 UTC from the cycle 17 ensemble mean analysis, (b) 2325 UTC form the cycle 18 analysis, (c) 2330 from the cycle 19 analysis, (d) 2335 UTC from the cycle 20 analysis, (e) 2340 UTC from the cycle 21 analysis, (f) 2345 UTC from the cycle 22 analysis, (g) 2350 from the cycle 23 analysis, (h) 2355 from the cycle 24 analysis, and (i) 0000 UTC from the cycle 25 analysis. Observed composite reflectivity constructed from WSR-88D interpolated data is used as truth. Values were calculated using grid points within a 30 km by 30 km domain positioned about the Monroe supercell center. Results shown for CNTRL (blue), AIRL (orange), AIRV (green), AIRVL (red), and AIRVL+S (purple) experiments.

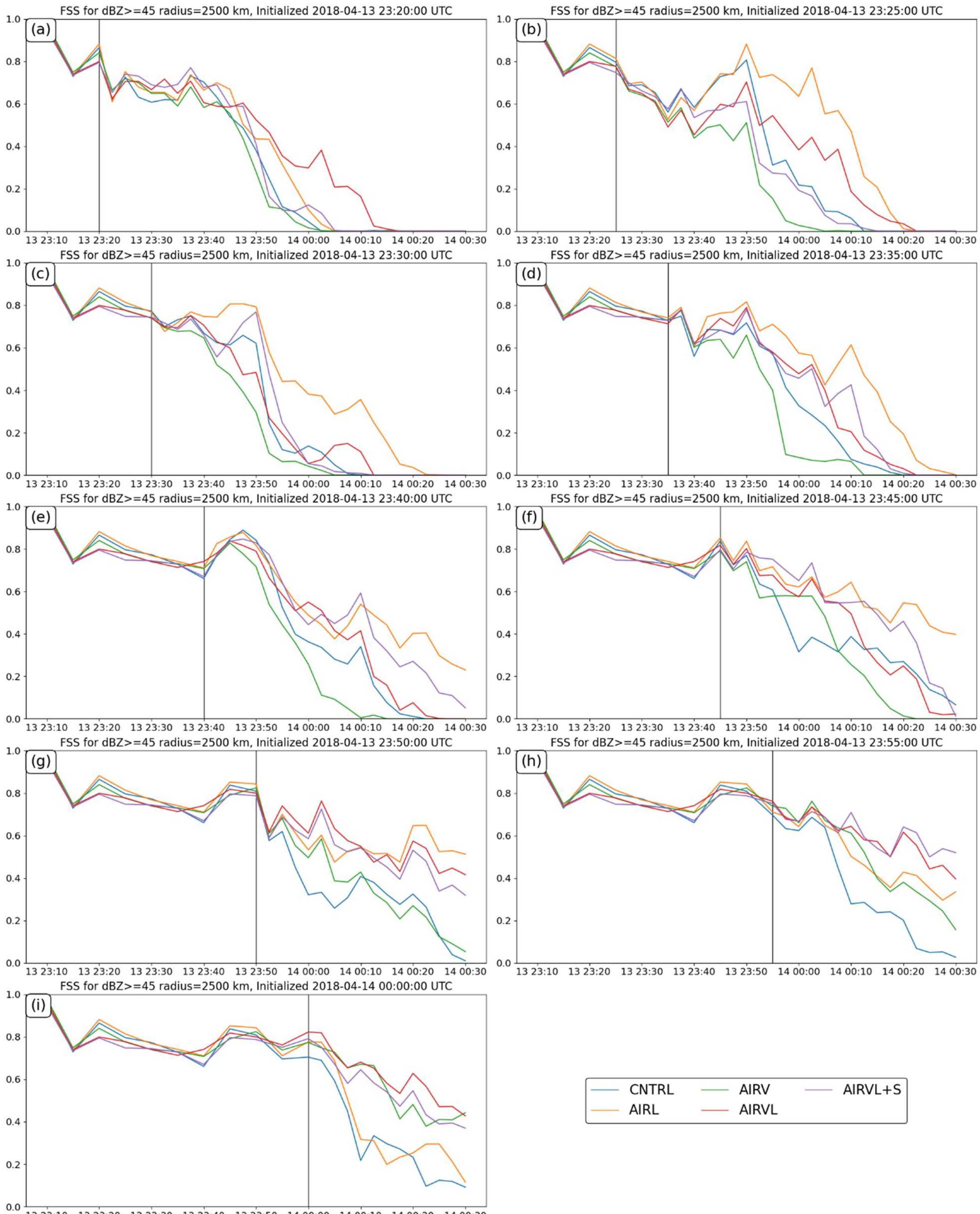

Figure 3.25: As in Figure 3.24, but for fractional skill scores calculated using a influence radius of 2.5 km.

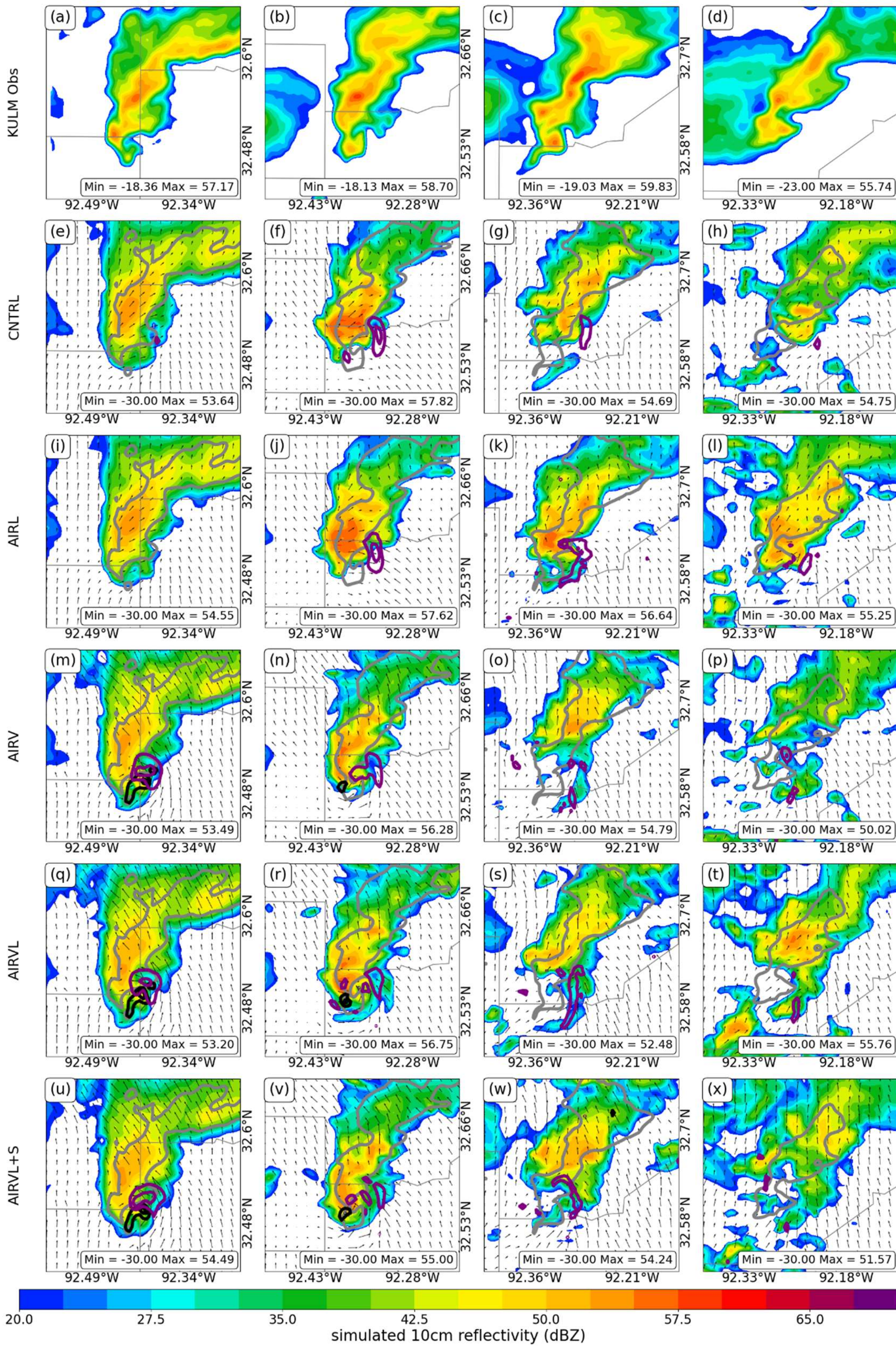

KULM Obs
CNTRL
AIRL
AIRV
AIRVL
AIRVL+S
(a)
Min = -18.36 Max = 57.17
(b)
Min = -18.13 Max = 58.70
(c)
Min = -19.03 Max = 59.83
(d)
Min = -23.00 Max = 55.74
(e)
Min = -30.00 Max = 53.64
(f)
Min = -30.00 Max = 57.82
(g)
Min = -30.00 Max = 54.69
(h)
Min = -30.00 Max = 54.75
(i)
Min = -30.00 Max = 54.55
(j)
Min = -30.00 Max = 57.62
(k)
Min = -30.00 Max = 56.64
(l)
Min = -30.00 Max = 55.25
(m)
Min = -30.00 Max = 53.49
(n)
Min = -30.00 Max = 56.28
(o)
Min = -30.00 Max = 54.79
(p)
Min = -30.00 Max = 50.02
(q)
Min = -30.00 Max = 53.20
(r)
Min = -30.00 Max = 56.75
(s)
Min = -30.00 Max = 52.48
(t)
Min = -30.00 Max = 55.76
(u)
Min = -30.00 Max = 54.49
(v)
Min = -30.00 Max = 55.00
(w)
Min = -30.00 Max = 54.24
(x)
Min = -30.00 Max = 51.57
92.49°W
92.34°W
92.43°W
92.28°W
92.36°W
92.21°W
92.33°W
92.18°W
32.6°N
32.48°N
32.66°N
32.53°N
32.7°N
32.58°N
32.76°N
32.64°N
20.0
27.5
35.0
42.5
50.0
57.5
65.0
simulated 10cm reflectivity (dBZ)

Figure 3.26: ((a)-(d)) Observed KULM reflectivity. Simulated 1 km AGL reflectivity (filled contours), 1 km AGL updraft (solid purple contours at 5, 10, and 15 m s^{-1}), 50 m AGL vertical vorticity (solid black contours at 15, 30, and 60 × 10^{-3} s^{-1}), 50 m horizontal wind vectors, and observed KULM reflectivity (solid gray contour at 40 dBZ) derived from deterministic forecasts initialized using the cycle 18 (2325 UTC) ensemble mean analyses for the ((e)-(h)) CNTRL, ((i)-(l)) AIRL, ((m)-(p)) AIRV, ((q)-(t)) AIRVL, and ((u)-(x)) AIRVL+S experiments. The columns correspond to different forecast times: initial conditions (first column), 10-minute forecast (second column), 20-minute forecast (third column), and 30-minute forecast (fourth column). All plots are centered on the observed supercell.

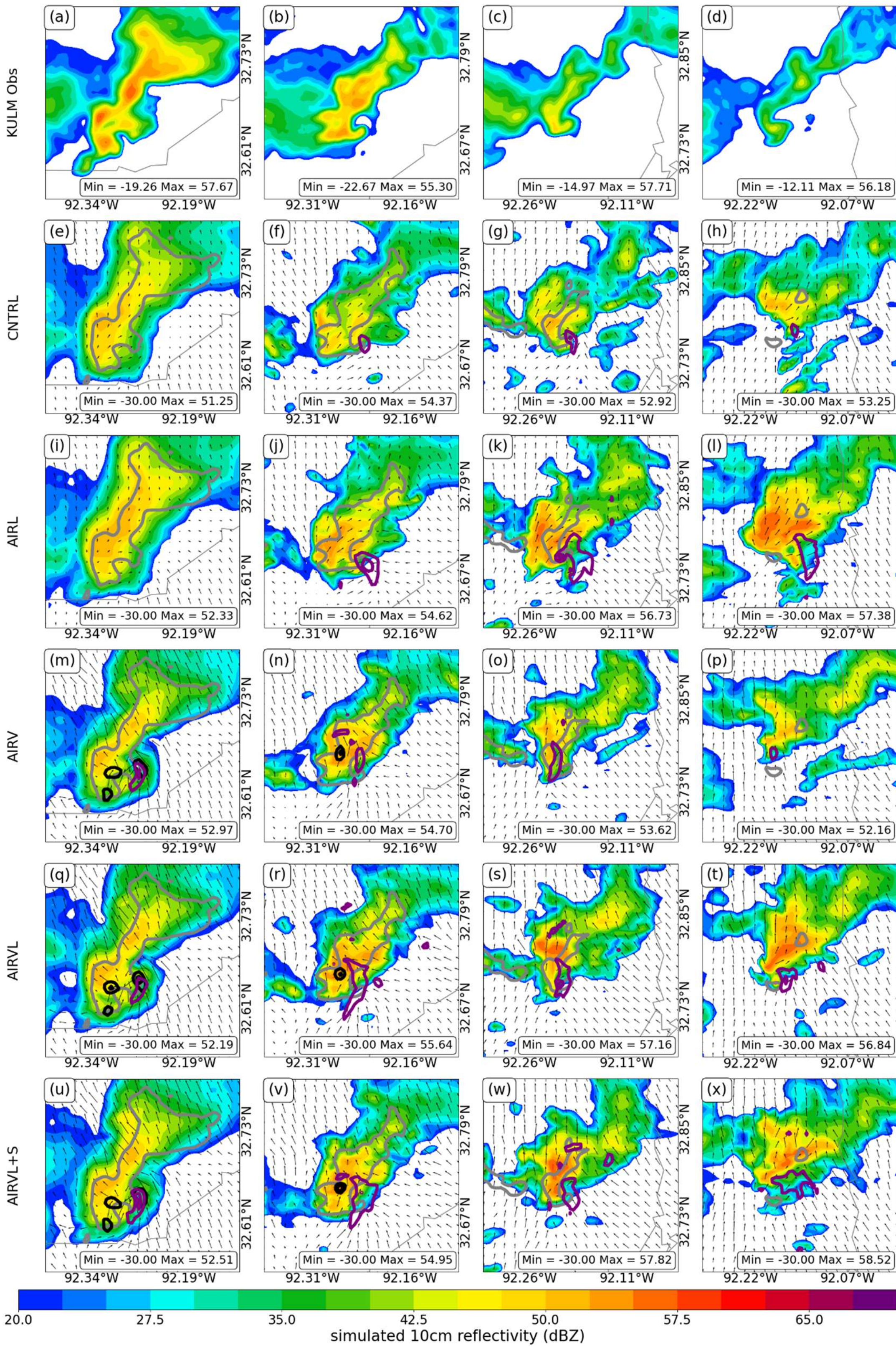

Figure 3.27: As in Figure 3.26, but showing results from deterministic forecasts initialized using the cycle 23 (2350 UTC) ensemble mean analyses.

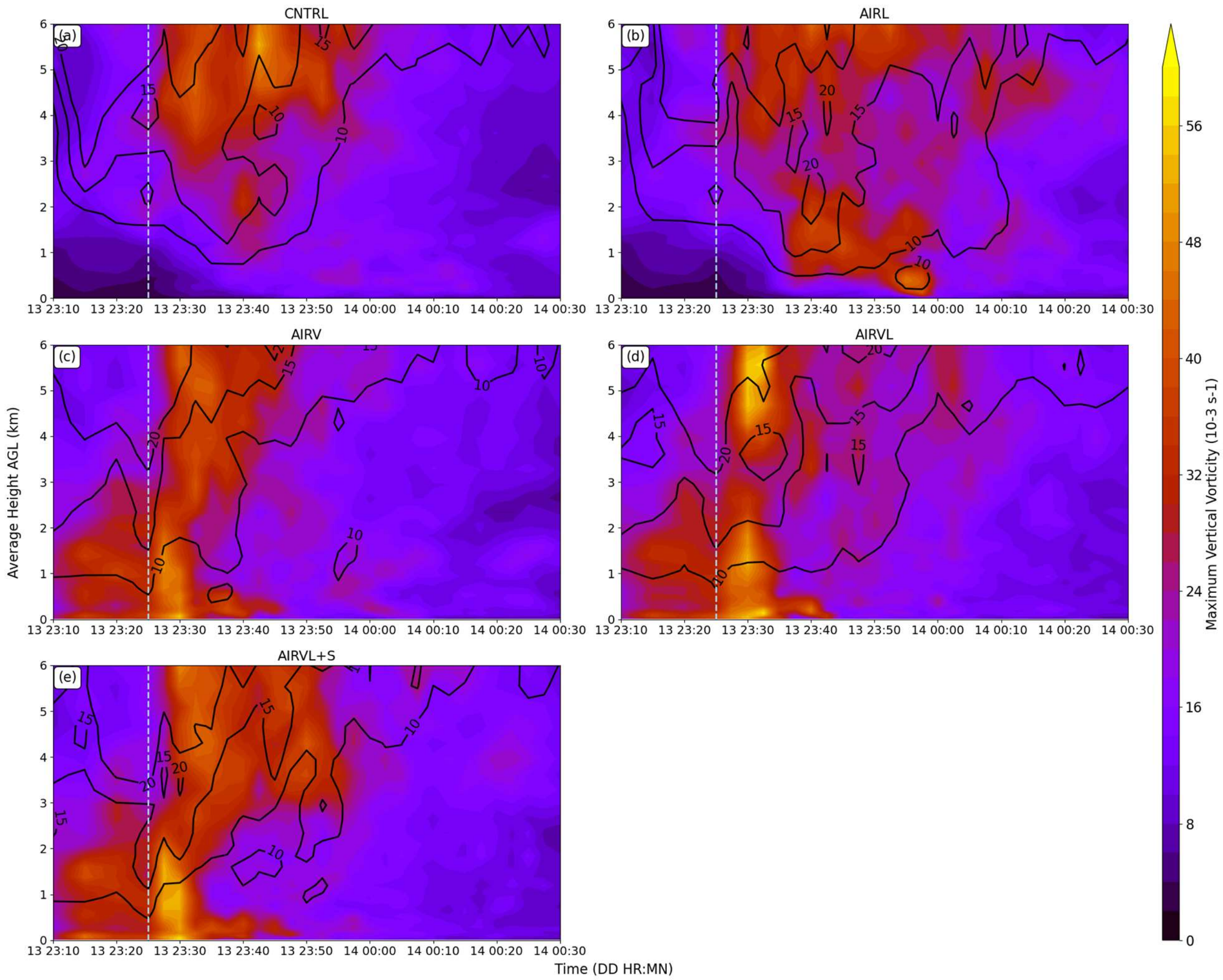

Figure 3.28: As in Figure 3.22, but the maximums for ensemble mean analyses are shown before 2325 UTC (cycle 18, dash light blue line), after which time the maximums for deterministic forecasts are shown.

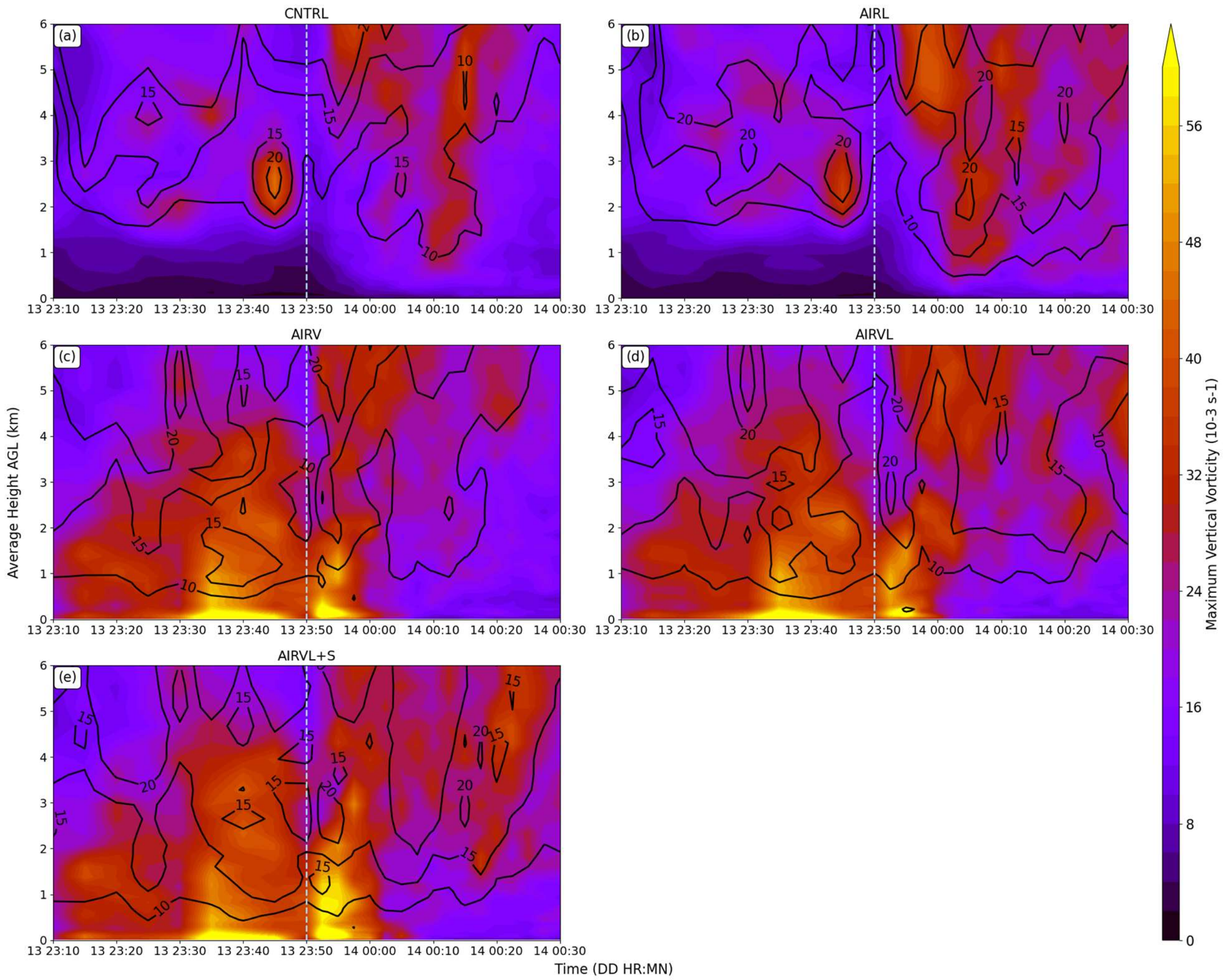

Figure 3.29: As in Figure 3.22, but the maximums for ensemble mean analyses are shown before 2350 UTC (cycle 23, dash light blue line), after which time the maximums for deterministic forecasts are shown.

There are several factors that could contribute to forecast degradation in the TDR and KULM DA. Partial sampling of the storm by TDR and KULM could lead to imbalances and inconsistencies in the analysis that negatively impact forecast performance. The dual-Doppler coverage of the TDR in each volume scan often only partially samples the storm horizontally. KULM only partially samples the storm vertically. Additionally, we suspect that the unphysically large values of downdraft at upper levels in TDR V_r data (described in section 3.1.2) may have had a negative impact on supercell evolution in the associated forecasts.

3.2.2 Forecasted Tornado Track and Intensity

Updraft helicity (UH) is a proven, useful tool in forecasting tornado tracks (Clark et al. 2012; Clark et al. 2013; Sobash et al. 2016). The metric was first introduced by Kain et al. (2008), whose original limits of integration were from 2 to 5 km. Since then, UH integrated at lower levels, such as 0 to 3 km, has been more especially used for tornado track forecasting (Sobash et al. 2016; Supinie et al. 2016; Sobash et al. 2019). Both 2 to 5 km UH and 0 to 3 km UH are calculated in this study. Despite the large values of low-level vorticity present in the AIRV, AIRVL, and AIRVL+S forecasts (Figure 3.22, Figure 3.28, and Figure 3.29), the AIRL forecasts generally have larger UH values and longer UH swaths (Figure 3.30, Figure 3.31, Figure 3.32, and Figure 3.33). This stems from larger values of mid-level, and to a lesser degree low-level, updrafts present in the AIRL forecasts verses of other forecasts, especially at later forecast times. AIRV, AIRVL, and AIRVL+S forecasts generally have higher magnitudes of updraft than CNTRL and AIRL forecasts at initialization, with the maximum occurring within 5 mins of initialization. However, the updraft weakens quickly thereafter. Since the AIRV analyses lack the critical BL information provided by CRL q_V DA, a weaker updraft and associated mesocyclone in the AIRV forecasts verses the AIRL forecasts is unsurprising. As mentioned in section 1, TDR/ KULM DA can vastly improve in-storm and near-storm properties in the analysis but cannot modify or improve the storm's environment. Conversely, CRL q_v data does not directly impact the properties of the supercell when assimilated, but the perceived effects of the DA on supercell structure and dynamics can be significant once the modified air is ingested by the storm. Air parcels in the inflow region of the supercell may take tens of minutes to be ingested by the storm, which is why its properties affect the supercell at later forecast times. However, it is unclear why the mid-level updraft and associated mesocyclone weakens so quickly in the AIRVL and AIRVL+S analyses, as these experiments assimilate both CRL, TDR, and KULM data. Additional investigation is needed to determine the cause of updraft weakening.

Despite the weakening of mid-level updrafts and the mesocyclone, the effects of stretching on low-level vorticity are clearly shown in the forecasts of AIRV, AIRVL, and AIRVL+S experiments. For most forecasts, the low-level vertical vorticity intensifies significantly shortly after initialization, increasing by a factor of ~2. The low-level vorticity is maximumized usually within the first 5 to 10 minutes (Figure 3.22, Figure 3.28, and Figure 3.29). Low-level vorticity swaths (at 50 m AGL), while relatively short, are clear and identifiable in the AIRV, AIRVL, and AIRVL+S forecasts, but are absent in the CNTRL and AIRL forecasts. Thus, while the supercell persists longer and maintains a stronger, longer-lived mid-level mesocyclone in the AIRL forecasts, the magnitude of low-level vorticity in AIRL forecasts is significantly lower than in AIRV, AIRVL, and AIRVL+S forecasts. Therefore, the AIRV, AIRVL, and AIRVL+S predicts the intensity, track, and overall structure of the TLV much better than the CNTRL and AIRL forecasts.

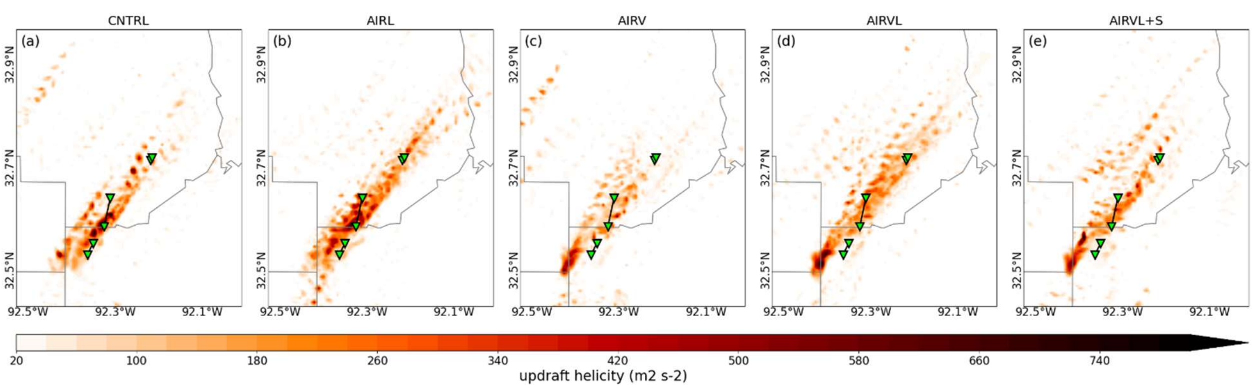

Figure 3.30: Composite 2 to 5 km updraft helicity (m^2 s^2) for forecasts initialized using cycle 18 (2325 UTC) ensemble mean analyses for (a) CNTRL, (b), AIRL, (c) AIRV, (d) AIRVL, and (e) AIRVL+S experiments. Green triangles indicate the start and end locations of real tornadoes tracks produced by Monroe supercell. The black lines connecting green triangles indicate real tornado tracks.

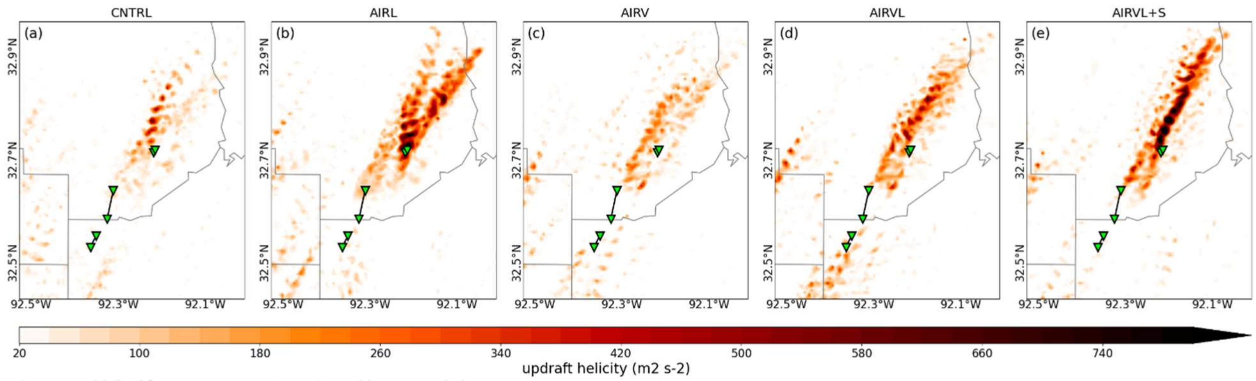

Figure 3.31: As in Figure 3.30, but for cycle 23 (2350 UTC).

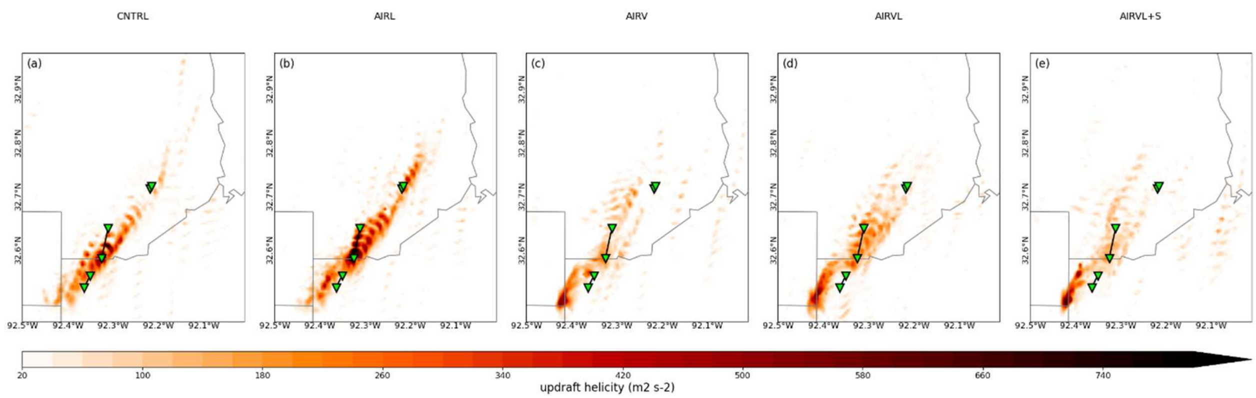

Figure 3.32: As in Figure 3.30, but for composite 0 to 3 km updraft helicity.

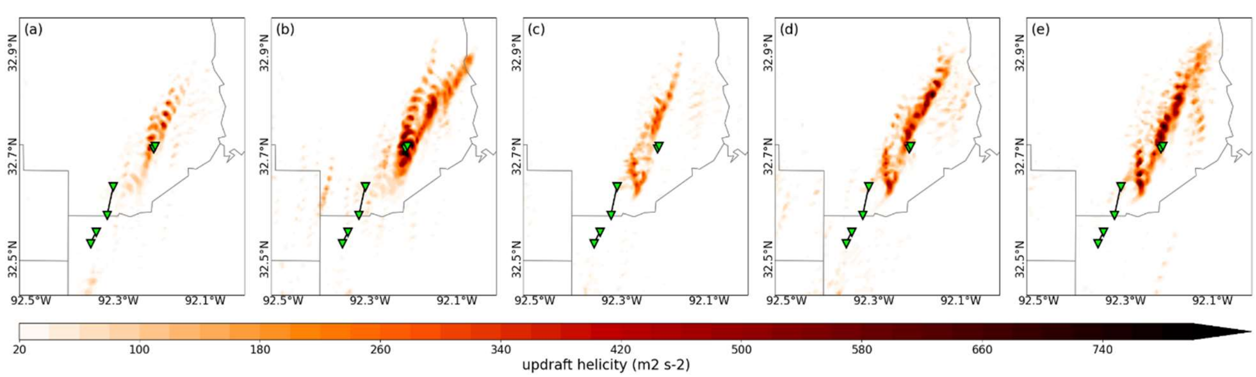

Figure 3.33: As in Figure 3.31, but for composite 0 to 3 km updraft helicity.

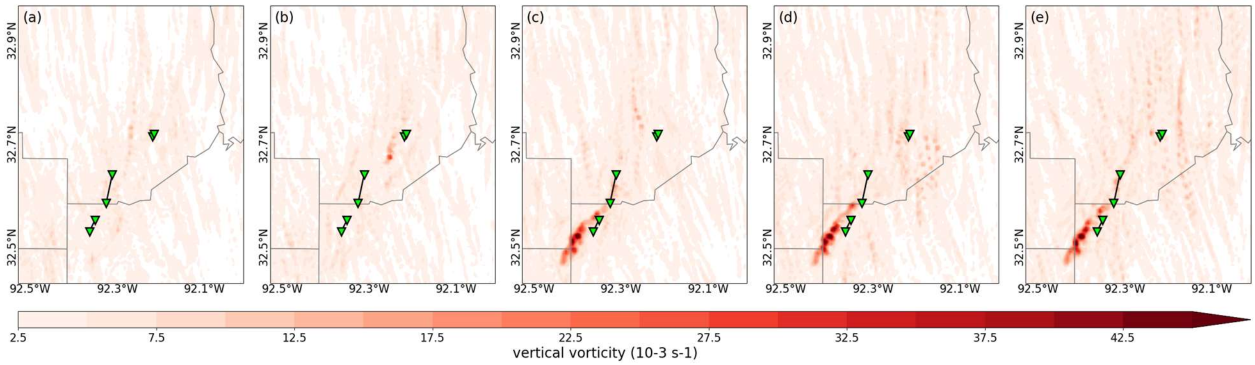

Figure 3.34: As in Figure 3.30, but for 50 m vertical vorticity (10^{-3} s^{-1}).

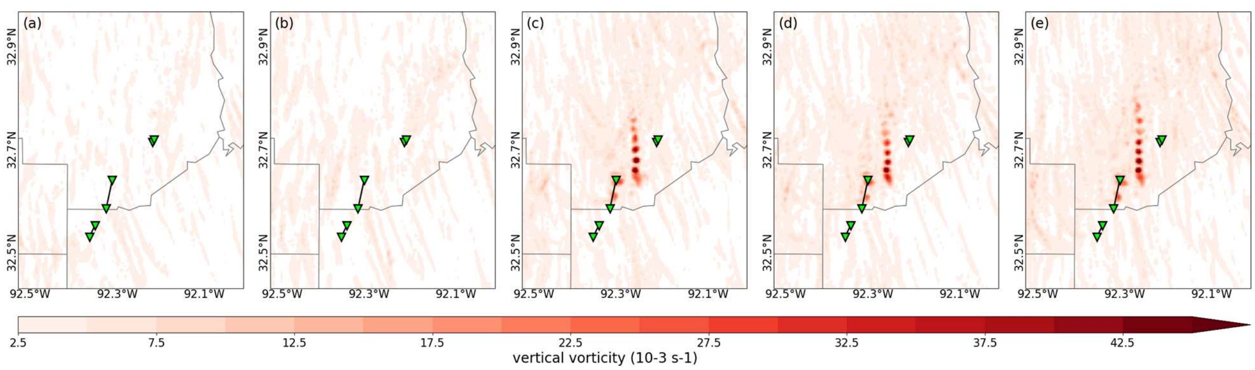

Figure 3.35: As in Figure 3.31, but for 50 m vertical vorticity (10^{-3} s^{-1}).

Chapter 4: Summary, Conclusions and Future Work

In this study, novel DA experiments assimilating VSE18 observations were successfully performed for the multi-tornado producing 13 April 2018 Monroe supercell. In addition to surface observations and WSR-88D Z and V_r observations, CRL-derived q_v profiles (AIRL, AIRVL, AIRVL+S), TDR V_r data (AIRV, AIRVL, AIRVL+S), and special sounding data (AIRVL+S) were also assimilated. The DA period was comprised of 25 DA cycles performed at 5-minute intervals from 2200 UTC on 13 April 2018 to 0000 UTC on 14 April 2018 in a domain centered in northcentral Louisiana. DA was conducted using 2500 m and 500 m two-way nested grids. Successful DA was verified using innovation statistics. The impacts of CRL q_v, TDR V_r, and special sounding DA on the storm structure and storm environment in the analyses were investigated using horizontal cross-sections and 3D renderings. Upon completion of the DA, a series of deterministic forecasts were conducted on two-way nested 2500 m, 500 m, and 100 m resolution grids using the ensemble mean analyses from cycles 17 (2310 UTC) through 25 (0000 UTC) as initial conditions. All forecasts, regardless of initialization time, terminated at 0030 UTC on 14 April 2018. The impacts of CRL q_v, TDR V_r, and special sounding DA on predicted reflectivity were determined quantitatively using ETS and FSS statistical scores. Differences in storm structure were evaluated using horizontal cross-sections, vertical cross sections, and composites. 2 to 5 km UH swaths, 0 to 3 km UH swaths, and composite 50 m vertical vorticity were used to investigate forecasted tornado track and intensity.

Results from the DA portion of this study yield the following conclusions:

- The assimilation of CRL q_v data results in much larger values of q_v in the inflow region of the supercell than other analyses.
- The assimilation of TDR and KULM V_r data results in higher values of low-level vertical vorticity. The TLV is present in TDR and KULM DA analyses but is absent in analyses from other experiments. The TLV strength is maximized around the time the first tornado occurs. The low-level circulation associated with the TLV is strongest just above the surface at times when tornadoes were observed.
- The assimilation of TDR and KULM V_r data increases the strength of low- and mid-level updrafts in the analyses.
- The impact of assimilating special soundings in earlier cycles (6 and 7) on analyses later cycles (15 through 25) is relatively small, and the sign of the impact

is not always consistent. This is likely due to the advection the sounding-modified environment away from the Monroe supercell.

- Ultimately, the analyses produced by assimilating both CRL q_v, TDR V_r, and KULM V_r are superior to those of other experiments, since they include stronger TLV signatures, more intense low- and mid-level updrafts, and improved BL conditions in the inflow region of the supercell.

Results from the forecast portion of this study yield the following conclusions:

- For most cycles, the forecasted Monroe supercell in CRL q_v DA experiments retains supercellular characteristics, including strong mid-level updrafts and associated mesocyclone, longer than the forecasts from other experiments.
- CRL q_v DA experiments better forecast reflectivity than other experiments, as indicated better statistical scores. This is likely caused by improved moisture in the inflow region of the supercell.
- CRL q_v DA experiments have longer and more intense UH tracks than most other experiments.
- TDR and KULM V_r DA experiments, especially AIRVL and AIRVL+S, better predict the intensity, track, and overall structure of the TLV.
- TDR/ KULM V_r DA appears to degrade reflectivity forecasts in earlier cycles (15 through 23), as indicated by poor statistical scores and the qualitatively observed disorganization of the supercell 15 to 20 minutes after initialization.
- Special sounding DA does not consistently improve forecasts. As before, this inconsistency is suspected to be a consequence of the advection of the special sounding modified environment away from the supercell.

Additional work can be completed to further support our conclusions. While forecasts on the tornado-resolving 100 m nested grid were completed, results were not investigated thoroughly on the native 100 m grid in this study due to time constraints. We plan to further investigate the results on the native 100 m grid, including the evolution of the tornadic circulation, via the creation of three-dimensional renderings, as was done for ensemble mean analyses. We would also like to further understand the causes of differences in deterministic forecasts between experiments and thereby determine more definitively the causes of thunderstorm improvement and degradation in the Monroe supercell storm. Computing parcel trajectories from the supercell mesocyclone, backward towards the inflow region of the supercell, may also be useful in determining if and when the CRL q_v DA-modified air is ingested by the supercell. This information may further improve our understanding of the impact of CRL q_v DA on forecasted storm dynamics. The TDR and CRL datasets for additional VSE18 cases are also available, including another tornadic supercell case that also occurred in the Monroe, LA area on 6 April 2018. If possible, EnKF DA for the 6 April 2018 tornadic supercell should also be conducted, to verify if the impacts of TDR and CRL DA found in this study are also found in other DA cases. Given that the EnKF cycles produced ensembles of analyses, ensemble forecasts of up to 40 members can be run if sufficient computational resources are available. Better prediction of the tornado may be obtained on the 100 m grid in some of the members, given the large uncertainties with tornado-resolving predictions. Probabilistic forecasting skills of the ensemble forecasts can also be assessed, following the Snook et al. (2019).

References

Adam, S., A. Behrendt, T. Schwitalla, E. Hammann, and V. Wulfmeyer, 2016: First assimilation of temperature lidar data into an NWP model: impact on the simulation of the temperature field, inversion strength and PBL depth. *Quart. J. Roy. Meteor. Soc.*, **142,** 2882-2896, https://doi.org/10.1002/qj.2875.

Agee, E., and L. Taylor, 2019: Historical Analysis of U.S. Tornado Fatalities (1808–2017) Population, Science, and Technology. *Wea. Climate Soc.*, **11,** 355-368, https://doi.org/10.1175/WCAS-D-18-0078.1.

Alford, A. A., M. I. Biggerstaff, C. L. Ziegler, D. P. Jorgensen, and G. D. Carrie, 2022: A Method for Correcting Staggered Pulse Repetition Time (PRT) and Dual Pulse Repetition Frequency (PRF) Processor Errors in Research Radar Datasets. *J. Atmos. Oceanic Technol.*, **39,** 1763-1780, https://doi.org/10.1175/JTECH-D-21-0176.1.

Ashley, W. S., 2007: Spatial and Temporal Analysis of Tornado Fatalities in the United States: 1880–2005. *Wea. Forecasting*, **22,** 1214-1228, https://doi.org/10.1175/2007WAF2007004.1.

Bjerknes, V., 1904: Das Problem der Wettervorhersage, betrachtet vom Standpunkte derMechanik und der Physik. *Meteorol Z*, **21,** 1-7, https://doi.org/10.1127/0941-2948/2009/416.

Bluestein, H. B., W. P. Unruh, D. C. Dowell, T. A. Hutchinson, T. M. Crawford, A. C. Wood, and H. Stein, 1997: Doppler Radar Analysis of the Northfield, Texas, Tornado of 25 May 1994. *Mon. Wea. Rev.*, **125,** 212-230, https://doi.org/10.1175/1520-0493(1997)125<0212:DRAOTN>2.0.CO;2.

Caumont, O., and Coauthors, 2016: Assimilation of humidity and temperature observations retrieved from ground‐based microwave radiometers into a convective‐scale NWP model. *Quart. J. Roy. Meteor. Soc.*, **142,** 2692-2704, https://doi.org/10.1002/qj.2860.

Chipilski, H. G., X. Wang, and D. B. Parsons, 2020: Impact of Assimilating PECAN Profilers on the Prediction of Bore-Driven Nocturnal Convection: A Multiscale Forecast Evaluation for the 6 July 2015 Case Study. *Mon. Wea. Rev.*, **148,** 1147-1175, https://doi.org/10.1175/MWR-D-19-0171.1.

Chipilski, H. G., X. Wang, D. B. Parsons, A. Johnson, and S. K. Degelia, 2022: The Value of Assimilating Different Ground-Based Profiling Networks on the Forecasts of Bore-Generating Nocturnal Convection. *Mon. Wea. Rev.*, **150,** 1273-1292, https://doi.org/10.1175/MWR-D-21-0193.1.

Clark, A. J., and Coauthors, 2013: Tornado path length forecasts from 2010-2011 using ensemble updraft helicity. *Wea. Forecasting*, **28,** 387-407, https://doi.org/10.1175/WAF-D-12-00038.1.

Clark, A. J., and Coauthors, 2012: An overview of the 2010 Hazardous Weather Testbed Experimental Forecast Program Spring Experiment. *Bull. Amer. Meteor. Soc.*, **93,** 55–74, https://doi.org/10.1175/bams-d-11-00040.1.

Coniglio, M. C., G. S. Romine, D. D. Turner, and R. D. Torn, 2019: Impacts of Targeted AERI and Doppler Lidar Wind Retrievals on Short-Term Forecasts of the Initiation and Early Evolution of Thunderstorms. *Mon. Wea. Rev.*, **147,** 1149-1170, https://doi.org/10.1175/MWR-D-18-0351.1.

Courtier, P., 1997: Dual formulation of four-dimensional variational assimilation. *Quart. J. Roy. Meteor. Soc.*, **123,** 2449-2461, https://doi.org/10.1002/qj.49712354414.

Davis, B., X. Wang, and X. Lu, 2021: A Comparison of HWRF Six-Hourly 4DEnVar and Hourly 3DEnVar Assimilation of Inner Core Tail Dopper Radar Observations for the Prediction of Hurricane Edouard (2014). *Atmosphere*, **12**, https://doi.org/10.3390/atmos12080942.

Degelia, S. K., X. Wang, D. J. Stensrud, and D. D. Turner, 2020: Systematic Evaluation of the Impact of Assimilating a Network of Ground-Based Remote Sensing Profilers for Forecasts of Nocturnal Convection Initiation during PECAN. *Mon. Wea. Rev.*, **148,** 4703-4728, https://doi.org/10.1175/MWR-D-20-0118.1.

Dowell, D., F. Zhang, L. J. Wicker, C. Snyder, and N. A. Crook, 2004: Wind and Temperature Retrievals in the 17 May 1981 Arcadia, Oklahoma Supercell: Ensemble Kalman Filter Experiments. *Mon. Wea. Rev.*, **132,** 1982-2005, https://doi.org/10.1175/1520-0493(2004)132<1982:WATRIT>2.0.CO;2.

Dowell, D. C., and L. J. Wicker, 2009: Additive Noise for Storm-Scale Ensemble Data Assimilation. *J. Atmos. Oceanic Technol.*, **26,** 911-927, https://doi.org/10.1175/2008JTECHA1156.1.

Du, N., M. Xue, K. Zhao, and J. Min, 2012: Impact of assimilating airborne Doppler radar velocity data using the ARPS 3DVAR on the analysis and prediction of hurricane Ike (2008). *J. Geophy. Res.*, **117,** D18113, https://doi.org/10.1029/2012JD017687.

Evensen, G., 1994: Sequential Data Assimilation with a Nonlinear Quasi-Geostrophic Model Using Monte-Carlo Methods to Forecast Error Statistics. *J. Geophys. Res.:Oceans*, **99,** 10143-10162, https://doi.org/10.1029/94JC00572.

Fabry, F., and V. Meunier, 2020: Why Are Radar Data so Difficult to Assimilate Skillfully? *Mon. Wea. Rev.*, **148,** 2819-2836, https://doi.org/10.1175/MWR-D-19-0374.1.

Fortin, V., M. Abaza, F. Anctil, and R. Turcotte, 2014: Why Should Ensemble Spread Match the RMSE of the Ensemble Mean? *J. Hydrometeorology*, **15,** 1708-1713, https://doi.org/10.1175/JHM-D-14-0008.1.

Green, T., X. Wang, and X. Lu, 2022: Impact of Assimilating Ground-Based and Airborne Radar Observations for the Analysis and Prediction of the Eyewall Replacement Cycle of Hurricane Matthew (2016) Using the HWRF Hybrid 3DEnVar System. *Mon. Wea. Rev.*, **150,** 1157-1175, https://doi.org/10.1175/MWR-D-21-0234.1.

Grzeschik, M., and Coauthors, 2008: Four-Dimensional Variational Data Analysis of Water Vapor Raman Lidar Data and Their Impact on Mesoscale Forecasts. *J. Atmos. Oceanic Technol.*, **25,** 1437-1453, https://doi.org/10.1175/2007JTECHA974.1.

Gustafsson, N., and Coauthors, 2018: Survey of data assimilation methods for convective-scale numerical weather prediction at operational centres. *Quart. J. Roy. Meteor. Soc.*, **144,** 1218-1256, https://doi.org/10.1002/qj.3179.

Hamill, T. M., and C. Snyder, 2000: A hybrid ensemble Kalman filter - 3D variational analysis scheme. *Mon. Wea. Rev.*, **128,** 2905-2919, https://doi.org/10.1175/1520-0493(2000)128<2905:AHEKFV>2.0.CO;2.

Hartman, C. M., X. Chen, E. E. Clothiaux, and M.-Y. Chan, 2021: Improving the Analysis and Forecast of Hurricane Dorian (2019) with Simultaneous Assimilation of GOES-16 All-Sky Infrared Brightness Temperatures and Tail Doppler Radar Radial Velocities. *Mon. Wea. Rev.*, **149,** 2193-2212, https://doi.org/10.1175/MWR-D-20-0338.1.

Helmus, J. J., and S. M. Collis, 2016: The Python ARM Radar Toolkit (Py-ART), a Library for Working with Weather Radar Data in the Python Programming Language. *Journal of Open Research Software*, **4,** e25, https://doi.org/10.5334/jors.119.

Hosek, M. J., C. L. Ziegler, M. I. Biggerstaff, T. A. Murphy, and Z. Wang, 2023: Relation between Baroclinity, Horizontal Vorticity, and Mesocyclone Evolution in the 6–7 April 2018 Monroe, Louisiana, Tornadic Supercell during VORTEX-SE. *Mon. Wea. Rev.*, **151,** 2949-2976, https://doi.org/10.1175/MWR-D-22-0313.1.

Hu, J., N. Yussouf, D. D. Turner, T. A. Jones, and X. Wang, 2019: Impact of Ground-Based Remote Sensing Boundary Layer Observations on Short-Term Probabilistic Forecasts of a Tornadic Supercell Event. *Wea. Forecasting*, **34,** 1453-1476, https://doi.org/10.1175/WAF-D-18-0200.1.

Hu, M., M. Xue, and K. Brewster, 2006a: 3DVAR and cloud analysis with WSR-88D level-II data for the prediction of the Fort Worth, Texas, Tornadic thunderstorms. Part I: Cloud analysis and its impact. *Mon. Wea. Rev.*, **134,** 675-698, https://doi.org/10.1175/Mwr3092.1.

Hu, M., M. Xue, J. D. Gao, and K. Brewster, 2006b: 3DVAR and cloud analysis with WSR-88D level-II data for the prediction of the Fort Worth, Texas, Tornadic thunderstorms. Part II: Impact of radial velocity analysis via 3DVAR. *Mon. Wea. Rev.*, **134,** 699-721, https://doi.org/10.1175/Mwr3093.1.

Jidong, G., M. Xue, K. Brewster, F. Carr, and K. K. Droegemeier, 2002: New development of a 3DVAR system for a nonhydrostatic NWP model. *Preprint, 15th Conf. Num. Wea. Pred. and 19th Conf. Wea. Anal. Forecasting*, Amer. Meteor. Soc., 339-341.

Jorgensen, D. P., C. L. Ziegler, E. N. Rasmussen, A. A. Alford, and A. S. Goldstein, 2017: Improvements to the NOAA P-3 airborne Doppler tail-mounted radar: Supercell observations from VORTEX-Southeast. *38th Conference on Radar Meteorology*, American Meteorological Society.

Kain, J. S., and Coauthors, 2008: Severe-weather forecast guidance from the first generation of large domain convection-allowing models: Challenges and opportunities. *24th Conf. Severe Local Storms*, Savannah, GA, Ameri. Meteor. Soc., Paper 9A.2.

Kalnay, E., 2003: *Atmospheric Modeling, Data Assimilation, and Predictability.* Cambridge University Press, 341 pp.

Kong, R., M. Xue, and C. Liu, 2018: Development of a Hybrid En3DVar Data Assimilation System and Comparisons with 3DVar and EnKF for Radar Data Assimilation with Observing System Simulation Experiments. *Mon. Wea. Rev.*, **146,** 175-198, https://doi.org/10.1175/MWR-D-17-0164.1.

Kong, R., M. Xue, C. Liu, and Y. Jung, 2021: Comparisons of Hybrid En3DVar with 3DVar and EnKF for Radar Data Assimilation: Tests with the 10 May 2010 Oklahoma Tornado Outbreak. *Mon. Wea. Rev.*, **149,** 21-40, https://doi.org/10.1175/MWR-D-20-0053.1.

Labriola, J., N. Snook, Y. Jung, and M. Xue, 2020: Evaluating ensemble Kalman filter analyses of severe hail storms on 8 May 2017 in Colorado: Effects of state variable updating and multi-moment microphysics schemes on state variable cross-covariances. *Mon. Wea. Rev.*, **148,** 2365-2389, https://doi.org/10.1175/MWR-D-19-0300.1.

Lewis, J. M., and J. C. Derber, 1985: The use of adjoint equations to solve a variational adjustment problem with advective constraints. *Tellus*, **37A,** 309-322, https://doi.org/10.1111/j.1600-0870.1985.tb00430.x.

Lewis, W. E., T. J. Wagner, J. A. Otkin, and T. A. Jones, 2020: Impact of AERI Temperature and Moisture Retrievals on the Simulation of a Central Plains Severe Convective Weather Event. *Atmosphere*, **11**, https://doi.org/10.3390/atmos11070729.

Li, S., S. Jaroszynski, S. Pearse, L. Orf, and J. Clyne, 2019: VAPOR: A Visualization Package Tailored to Analyze Simulation Data in Earth System Science. *Atmosphere*, **10**, https://doi.org/10.3390/atmos10090488.

Li, X., Z. Pu, J. A. Zhang, and G. D. Emmitt, 2022: Combined Assimilation of Doppler Wind Lidar and Tail Doppler Radar Data over a Hurricane Inner Core for Improved Hurricane Prediction with the NCEP Regional HWRF System. *Remote Sens.*, **14**, https://doi.org/10.3390/rs14102367.

Li, Y., X. Wang, and M. Xue, 2012: Assimilation of Radar Radial Velocity Data with the WRF Hybrid Ensemble–3DVAR System for the Prediction of Hurricane Ike (2008). *Mon. Wea. Rev.*, **140,** 3507-3524, https://doi.org/10.1175/MWR-D-12-00043.1.

Lilly, D. K., 1990: Numerical prediction of thunderstorms—has its time come? *Quart. J. Roy. Meteor. Soc.*, **116,** 779-798, https://doi.org/10.1002/qj.49711649402.

Lin, G., and Z. Wang, 2023: VORTEX-SE_2018: Combined Dual Tail Doppler Radars and Compact Raman Lidar Data, Version 1.0. UCAR/NCAR - Earth Observing Laboratory, accessed 31 Dec 2023., https://doi.org/10.26023/T7ED-KT8Q-8D04.

Lin, G., Z. Wang, C. Ziegler, X.-M. Hu, M. Xue, B. Geerts, and Y. Chu, 2023: A Comparison of Convective Storm Inflow Moisture Variability between the Great Plains and the Southeastern United States Using Multiplatform Field Campaign Observations. *J. Atmos. Oceanic Technol.*, **40,** 539-556, https://doi.org/10.1175/JTECH-D-22-0037.1.

Lin, G., and Coauthors, 2024: Airborne Measurements of Scale-Dependent Latent Heat Flux Impacted by Water Vapor and Vertical Velocity over Heterogeneous Land Surfaces During the CHEESEHEAD19 Campaign. *J. Geophy. Res.*, **129,** e2023JD039586, https://doi.org/10.1029/2023JD039586.

Liu, B., Z. Wang, Y. Cai, P. Wechsler, W. Kuestner, M. Burkhart, and W. Welch, 2014: Compact airborne Raman lidar for profiling aerosol, water vapor and clouds. *Opt. Express*, **22,** 20613-20621, https://doi.org/10.1364/OE.22.020613.

Lorenc, A. C., 1986: Analysis methods for numerical weather prediction. *Quart. J. Roy. Meteor. Soc.*, **112,** 1177-1194, https://doi.org/10.1002/qj.49711247414.

Lu, X., X. Wang, M. Tong, and V. Tallapragada, 2017: GSI-Based, Continuously Cycled, Dual-Resolution Hybrid Ensemble–Variational Data Assimilation System for HWRF: System Description and Experiments with Edouard (2014). *Mon. Wea. Rev.*, **145,** 4877-4898, https://doi.org/10.1175/mwr-d-17-0068.1.

Majcen, M., P. Markowski, Y. Richardson, D. Dowell, and J. Wurman, 2008: Multipass Objective Analyses of Doppler Radar Data. *J. Atmos. Oceanic Technol.*, **25,** 1845-1858, https://doi.org/10.1175/2008JTECHA1089.1.

Murphy, T., 2018: KULM Radar Data, Version 1.0. UCAR/NCAR - Earth Observing Laboratory, accessed 01 Nov 2022, https://doi.org/10.5065/D6PV6J6B.

Murphy, T. A., C. Palmer, C. Entremont, and J. D. Lamb, 2019: Early operational successes of the University of Louisiana Monroe's Polarimetric S-band Doppler radar. *Journal of Operational Meteorology*, **7,** 105-116.

Natenberg, E., J. Gao, M. Xue, and F. H. Carr, 2013: Analysis and Forecast of a Tornadic Thunderstorm Using Multiple Doppler Radar Data, 3DVAR, and ARPS Model. *Adv Meteorol*, **2013**, https://doi.org/10.1155/2013/281695.

Pan, Y., and Coauthors, 2014: A GSI-Based Coupled EnSRF–En3DVar Hybrid Data Assimilation System for the Operational Rapid Refresh Model: Tests at a Reduced Resolution. *Mon. Wea. Rev.*, **142,** 3756-3780, https://doi.org/10.1175/MWR-D-13-00242.1.

Putnam, B., M. Xue, Y. Jung, N. Snook, and G. Zhang, 2019: Ensemble Kalman Filter Assimilation of Polarimetric Radar Observations for the 20 May 2013 Oklahoma Tornadic Supercell Case. *Mon. Wea. Rev.*, **147,** 2511-2533, https://doi.org/10.1175/MWR-D-18-0251.1.

Qin, X., 1996: Generalized Adjoint for Physical Processes with Parameterized Discontinuities. Part I: Basic Issues and Heuristic Examples. *Journal of the Atmospheric Sciences*, **53,** 1123-1142, https://doi.org/10.1175/1520-0469(1996)053<1123:gafppw>2.0.co;2.

Roberts, N. M., and H. W. Lean, 2008: Scale-selective verification of rainfall accumulations from high-resolution forecasts of convective events. *Mon. Wea. Rev*, **136,** 78-97.

Rotunno, R., and H. B. Bluestein, 2024: Recent developments in tornado theory and observations. *Rep. Prog. Phys.*, **87**, https://doi.org/10.1088/1361-6633/ad7f6a.

Schaefer, J. T., 1990: The critical success index as an indicator of warning skill. *Wea. Forecasting*, **5,** 570-575, https://doi.org/10.1175/1520-0434(1990)005<0570:TCSIAA>2.0.CO;2.

Schenkman, A. D., M. Xue, A. Shapiro, K. Brewster, and J. D. Gao, 2011: The Analysis and Prediction of the 8-9 May 2007 Oklahoma Tornadic Mesoscale Convective System by Assimilating WSR-88D and CASA Radar Data Using 3DVAR. *Mon. Wea. Rev.*, **139,** 224-246, https://doi.org/10.1175/2010mwr3336.1.

Shen, F., M. Xue, and J. Min, 2017: A comparison of the limited-area 3DVAR and Hybrid ETKF-En3DVAR data assimilation using radar observations at convective-scale for the prediction of Typhoon Saomai (2006). *Meteor. Apps.*, **24,** 628-641, https://doi.org/10.1002/met.1663.

Simmons, A. J., and A. Hollingsworth, 2002: Some aspects of the improvement in skill of numerical weather prediction. *Quart. J. Roy. Meteor. Soc.*, **128,** 647-678, https://doi.org/10.1256/003590002321042135.

Snook, N., M. Xue, and Y. Jung, 2011: Analysis of a Tornadic Mesoscale Convective Vortex Based on Ensemble Kalman Filter Assimilation of CASA X-Band and WSR-88D Radar Data. *Mon. Wea. Rev.*, **139,** 3446-3468, https://doi.org/10.1175/MWR-D-10-05053.1.

Snook, N., M. Xue, and Y. Jung, 2015: Multiscale EnKF Assimilation of Radar and Conventional Observations and Ensemble Forecasting for a Tornadic Mesoscale Convective System. *Mon. Wea. Rev.*, **143,** 1035-1057, https://doi.org/10.1175/mwr-d-13-00262.1.

——, 2019: Tornado-Resolving Ensemble and Probabilistic Predictions of the 20 May 2013 Newcastle–Moore EF5 Tornado. *Mon. Wea. Rev.*, **147,** 1215-1235, https://doi.org/10.1175/MWR-D-18-0236.1.

Snyder, C., and F. Q. Zhang, 2003: Assimilation of simulated Doppler radar observations with an ensemble Kalman filter. *Mon. Wea. Rev.*, **131,** 1663-1677, https://doi.org/10.1175//2555.1.

Sobash, R. A., C. S. Schwartz, G. S. Romine, and M. L. Weisman, 2019: Next-Day Prediction of Tornadoes Using Convection-Allowing Models with 1-km Horizontal Grid Spacing. *Wea. Forecasting*, **34,** 1117-1135, https://doi.org/10.1175/WAF-D-19-0044.1.

Sobash, R. A., G. S. Romine, C. S. Schwartz, D. J. G. II, and M. L. Weisman, 2016: Explicit forecasts of low-level rotation from convection-allowing models for next-day tornado prediction. *Wea. Forecasting*, **31,** 1591-1614, https://doi.org/10.1175/waf-d-16-0073.1.

Stensrud, D. J., and Coauthors, 2009: Convective-Scale Warn-on-Forecast System a Vision for 2020. *Bull. Amer. Meteor. Soc.*, **90,** 1487-1500, https://doi.org/10.1175/2009bams2795.1.

Stensrud, D. J., and Coauthors, 2013: Progress and challenges with Warn-on-Forecast. *Atmos Res*, **123,** 2-16, https://doi.org/10.1016/j.atmosres.2012.04.004.

Strader, S. M., and W. S. Ashley, 2018: Finescale Assessment of Mobile Home Tornado Vulnerability in the Central and Southeast United States. *Wea. Climate Soc.*, **10,** 797-812, https://doi.org/10.1175/WCAS-D-18-0060.1.

Supinie, T. A., Y. Jung, M. Xue, D. J. Stensrud, M. M. French, and H. B. Bluestein, 2016: Impact of VORTEX2 Observations on Analyses and Forecasts of the 5 June 2009 Goshen County, Wyoming, Supercell. *Mon. Wea. Rev.*, https://doi.org/10.1175/mwr-d-15-0171.1.

Supinie, T. A., Y. Nusrat, C. Jing, J. Youngsun, X. Ming, and W. Shizhang, 2017: Comparison of the analyses and forecasts of a tornadic supercell storm from assimilating phased array radar and WSR-88D observations. *Mon. Wea. Rev.*, **32,** 1379-1401, https://doi.org/10.1175/WAF-D-16-0159.1.

Tanamachi, R. L., L. J. Wicker, D. C. Dowell, H. B. Bluestein, D. T. Dawson, II, and M. Xue, 2013: EnKF Assimilation of High-Resolution, Mobile Doppler Radar Data of the 4 May 2007 Greensburg, Kansas, Supercell into a Numerical Cloud Model. *Mon. Wea. Rev.*, **141,** 625-648, https://doi.org/10.1175/mwr-d-12-00099.1.

Tong, M., and M. Xue, 2005: Ensemble kalman filter assimilation of doppler radar data with a compressible nonhydrostatic model : OSS experiments. *Mon. Wea. Rev.*, **133,** 1789-1807, https://doi.org/10.1175/MWR2898.1.

Vandenberghe, F., and R. Ware, 2002: 4-dimensional variational assimilation of ground-based microwave observations during a winter fog event. *Preceedings International Symposium on Atmospheric Senesing with GPS*, Japan Meteoroogical Agency, 5.

Wang, Z., and Coauthors, 2016: Airborne Raman Lidar and its Applications for Atmospheric Process Studies. *EPJ Web of Conferences*, **119**, https://doi.org/10.1051/epjconf/201611909002.

Weng, Y., and F. Zhang, 2012: Assimilating Airborne Doppler Radar Observations with an Ensemble Kalman Filter for Convection-Permitting Hurricane Initialization and Prediction: Katrina (2005). *Mon. Wea. Rev.*, **140,** 841-859, https://doi.org/10.1175/2011MWR3602.1.

Whitaker, J. S., and T. M. Hamill, 2002: Ensemble Data Assimilation without Perturbed Observations. *Mon. Wea. Rev.*, **130,** 1913-1924, https://doi.org/10.1175/1520-0493(2002)130<1913:EDAWPO>2.0.CO;2.

Whitaker, J. S., and T. M. Hamill, 2012: Evaluating Methods to Account for System Errors in Ensemble Data Assimilation. *Mon. Wea. Rev.*, **140,** 3078-3089, https://doi.org/10.1175/Mwr-D-11-00276.1.

Wu, D., and Coauthors, 2016: Airborne compact rotational Raman lidar for temperature measurement. *Opt. Express*, **24,** A1210-A1223, https://doi.org/10.1364/OE.24.0A1210.

Xiao, Q., X. Zhang, C. Davis, J. Tuttle, G. Holland, and P. J. Fitzpatrick, 2009: Experiments of hurricane initialization with airborne Doppler radar data for the Advanced Research Hurricane WRF (AHW) model. *Mon. Wea. Rev.*, **137,** 2758-2777, https://doi.org/10.1175/2009mwr2828.1.

Xue, M., K. Droegemeier, and V. Wong, 2000: The Advanced Regional Prediction System (ARPS) - A multi-scale nonhydrostatic atmospheric simulation and prediction model. Part I: Model dynamics and verification. *Meteorology and Atmospheric Physics*, **75,** 161-193, https://doi.org/10.1007/s007030070003.

Xue, M., M. Tong, and K. K. Droegemeier, 2006: An OSSE Framework Based on the Ensemble Square Root Kalman Filter for Evaluating the Impact of Data from Radar Networks on Thunderstorm Analysis and Forecasting. *J. Atmos. Oceanic Technol.*, **23,** 46-66, https://doi.org/10.1175/JTECH1835.1.

Yoshida, S., T. Sakai, T. Nagai, Y. Ikuta, Y. Shoji, H. Seko, and K. Shiraishi, 2022: Lidar Observations and Data Assimilation of Low-Level Moist Inflows Causing Severe Local Rainfall Associated with a Mesoscale Convective System. *Mon. Wea. Rev.*, **150,** 1781-1798, https://doi.org/10.1175/MWR-D-21-0213.1.

Zhang, F. Q., C. Snyder, and J. Z. Sun, 2004: Impacts of initial estimate and observation availability on convective-scale data assimilation with an ensemble Kalman filter. *Mon. Wea. Rev.*, **132,** 1238-1253, https://doi.org/10.1175/1520-0493(2004)132<1238:Ioieao>2.0.Co;2.

Zhang, F. Q., M. Zhang, and J. Poterjoy, 2013: E3DVar: Coupling an Ensemble Kalman Filter with Three-Dimensional Variational Data Assimilation in a Limited-Area Weather Prediction Model and Comparison to E4DVar. *Mon. Wea. Rev.*, **141,** 900-917, https://doi.org/10.1175/Mwr-D-12-00075.1.

Ziegler, C., 2019: NOAA P3 Radar Data, Version 1.0. UCAR/NCAR - Earth Observing Laboratory, accessed 01 Nov 2022, https://doi.org/10.26023/WP1T-TTJM-VJ00.

Ziegler, C. L., T. Murphy, Z. Wang, and M. J. Hosek, 2025a: Cold pool forcing of the streamwise vorticity current and low-level tornado-cyclones in the tornadic 13-14 April 2018 Monroe LA supercell during VORTEX-SE. *Mon. Wea. Rev.*, **153,** in preparation.

Ziegler, C. L., E. N. Rasmussen, T. R. Shepherd, A. I. Watson, and J. M. Straka, 2001: The Evolution of Low-Level Rotation in the 29 May 1994 Newcastle-Graham, Texas, Storm

Complex during VORTEX. *Mon. Wea. Rev.*, **129,** 1339-1368, https://doi.org/10.1175/1520-0493(2001)129<1339:TEOLLR>2.0.CO;2.

Ziegler, C. L., P. M. Markowski, Y. P. Richardson, C. C. Weiss, and S. M. Waugh, 2025b: Cold pool forcing of the streamwise vorticity current and low-level mesocyclone in the 9 June 2009 supercell during VORTEX-2. *Mon. Wea. Rev.*, **153,** submitted.

Ziegler, C. L., and Coauthors, 2018: Kinematics, thermodynamics, and microphysics of the tornadic 13-14 April 2018 Calhoun, LA supercell during VORTEX-SE. *29th Severe Local Storms Conference*, Stowe, VT, Amer. Meteor. Soc.